学位論文

Photoemission studies of new electron-doped cuprate high-temperature superconductors

(新規電子ドープ型銅酸化物高温超伝導体の光電子分光による研究)

平成28年12月博士（理学）申請

東京大学大学院理学系研究科

物理学専攻

堀尾眞史

Abstract

Since their discovery, the electronic structure of cuprate high-temperature superconductors has been intensively studied both experimentally and theoretically. Starting from the antiefrromagnetic (AF) Mott insulator, doping holes or electrons suppresses the AF order and induces the superconductivity. Since both hole- and electron-doped cuprates possess CuO_2 planes as a stage for the superconductivity, similarities and differences in their electronic structure should provide a clue for the mechanism of the high-temperature superconductivity. Unfortunately, however, most of studies have been concentrated on the hole-doped cuprates because of their rich materials variety and higher superconducting (SC) transition temperatures. The recent discovery of superconductivity without chemical electron doping (i.e., without Ce substitution for rare-earth atoms) in thin films and powdered samples have attracted much attention to electron-doped cuprates. Removal of excess oxygen through efficient annealing can suppress the antiferromagnetism and induce superconductivity even in the parent compounds. Inspired by the breakthrough on thin films and powdered samples, new annealing method, which is called protect-annealing method, has also been developed for bulk single crystals, leading to the emergence of superconductivity down to heavily underdoped region. In the present thesis, I have studied electronic structure of those "new" electron-doped cuprate superconductors by means of photoemission spectroscopy.

In chapter 3, thin films of the SC parent compound Pr_2CuO_4 have been synthesized and studied by angle-resolved photoemission spectroscopy (ARPES). In order to perform ARPES measurements, which is highly surface sensitive, we first synthesized the SC Pr_2CuO_4 by growing it under highly reducing condition, instead of annealing it after the growth *ex-situ*, to avoid the surface contamination. Then, we carried out ARPES measurements and observed clear Fermi surfaces, whose area suggests electron concentration is much larger than half filling. Chapter 4 was devoted to relatively bulk-sensitive hard X-ray photoemission and soft X-ray absorption spectroscopy on the SC parent compound Nd_2CuO_4 and related materials. We have observed a chemical-potential shift between insulating and SC Nd_2CuO_4, which again suggests that SC parent compound is not at half-filling, but is doped with electrons, probably due to oxygen deficiency.

In chapter 5, we have performed a systematic ARPES study on protect-annealed

underdoped $Pr_{1.3-x}La_{0.7}Ce_xCuO_4$ single crystals with varying Ce concentration and annealing condition to reveal the difference between the effect of Ce doping and annealing on the electronic structure. Efficient annealing was found not only to dope the system with electrons, but also to remove a gap at the Fermi level and decrease the magnitude of AF band splitting. We have concluded that as-grown sample contains disorder which produces the Coulomb gap and increase AF correlation, and the disorder is removed by annealing.

In chapter 6, the nature of the AF band splitting, which is called AF pseudogap in electron-doped cuprates, has been studied by ARPES. We have revealed that the AF pseudogap shows non-trivial momentum dependence, and concluded from comparison with a variational Monte-Carlo calculation that it is due to the effect of strong electron correlation beyond the simple AF band splitting.

In chapter 7, we have studied the SC gap of protect-annealed $Pr_{1.3-x}La_{0.7}Ce_xCuO_4$ single crystals. Although AF correlation was strongly suppressed by protect annealing, the SC gap was found to have *d*-wave symmetry, which may be mediated by AF spin fluctuations.

We have thus studied the electronic structure of the "new" electron-doped cuprate superconductors focusing on the effect of annealing on the carrier concentration, AF correlation, and superconductivity. The present study will not only advance our understanding of the electron-doped cuprate superconductors but also promote reconsideration of the electronic structure and paring mechanism of the hole-doped cuprate superconductors.

Contents

1 Introduction **1**
- 1.1 General aspects of the electron-doped cuprate superconductors . . . 1
- 1.2 Electronic structure and physical properties . . . 2
- 1.3 Role of annealing . . . 6
- 1.4 Antiferromagnetic pseudogap . . . 9
- 1.5 Superconducting gap . . . 13
- 1.6 New electron-doped cuprate superconductors . . . 15
- 1.7 Motivation . . . 20
- 1.8 Outline of the thesis . . . 23

2 Experimental methods and principles **25**
- 2.1 Photoemission spectroscopy . . . 25
  - 2.1.1 General formulation . . . 25
  - 2.1.2 Angle-resolved photoemission spectroscopy . . . 26
  - 2.1.3 Spectral function and self energy . . . 28
  - 2.1.4 Electron escape depth . . . 32
- 2.2 Experimental setup . . . 34
  - 2.2.1 Photosmission measurement system . . . 34
  - 2.2.2 MBE growth system . . . 35

3 Film growth and angle-resolved photoemission spectroscopy of the superconducting parent compound Pr_2CuO_4 **37**
- 3.1 Introduction . . . 37
- 3.2 Growth of as-grown superconducting Pr_2CuO_4 thin films . . . 39
- 3.3 Angle-resolved photoemission spectroscopy of Pr_2CuO_4 thin films . 41
- 3.4 Conclusion . . . 52

4 Core-level electronic structure of the superconducting parent compound Nd_2CuO_4 and Ce-doped compounds $Nd_{2-x}Ce_xCuO_4$ **53**
- 4.1 Introduction . . . 53
- 4.2 Experimental . . . 53

4.3 Results and discussion 55
4.4 Conclusion 65

5 Effect of protect annealing versus Ce doping on the electronic structure of underdoped $Pr_{1.3-x}La_{0.7}Ce_xCuO_4$ 67
5.1 introduction 67
5.2 Experimental 68
5.3 Results and discussion 69
5.4 conclusion 74

6 Nature of the antiferromagnetic gap in the electron-doped cuprates $Pr_{1.3-x}La_{0.7}Ce_xCuO_4$ 75
6.1 Introduction 75
6.2 Experimental 76
6.3 Results and discussion 76
6.4 Conclusion 80

7 Superconducting gap of protect-annealed $Pr_{1.3-x}La_{0.7}Ce_xCuO_4$ single crystals 83
7.1 Introduction 83
7.2 Experimental 84
7.3 Results and discussion 84
7.4 Conclusion 87

8 Summary and conclusion 89

Acknowledgements 91

Chapter 1

Introduction

1.1 General aspects of the electron-doped cuprate superconductors

Three years after the discovery of the hole-doped cuprate superconductors, electron-doped cuprate superconductors were discovered in 1989 [1]. Electron doping is typically achieved by substituting Ce for Ln (lanthanoid) in Ln_2CuO_4. Although both hole-doped and electron-doped high-temperature (high-T_c) superconductors have CuO_2 planes as the stage of superconductivity, they have many differences.

One of the major differences is the crystal structure. While one of the hole-doped cuprates has the so-called T-type structure, in which the Cu atoms are octahedrally co-ordinated by O atoms, electron-doped cuprates have the T'-type structure, in which the Cu atoms are surrounded by the square of four O atoms as shown in Fig. 1.1(a).

Another characteristic difference is found in the phase diagram shown in Fig. 1.1(b). Both of the parent compounds are antiferromagnetic (AF) insulators and superconductivity is achieved by hole or electron doping. However, in the hole-doped cuprates, antiferromagnetism is quickly suppressed by $\sim 3\%$ doping while in the electron-doped cuprates on the other hand, antiferromagnetism is so robust that it persists up to $\sim 15\%$ doping. Furthermore, the doping region where superconductivity is realized is much narrower and the T_c is relatively low (< 30 K) in the electron-doped cuprates. Due to the lower T_c and the difficulty in sample preparation mentioned below, electron-doped cuprates have not been studied extensively neither experimentally nor theoretically compared to the hole-doped cuprates, and they still possess many unresolved problems. The physical properties and current issues in the electron-doped cuprates are described in the following sections.

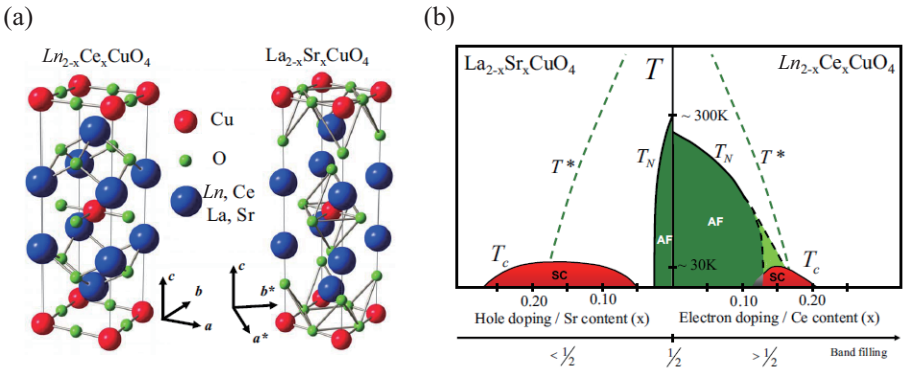

Figure 1.1: Crystal structures and phase diagrams of the electron- and hole-doped cuprates [2]. (a) T'-type and T-type crystal structures, respectively, of the electron-doped (left) and hole-doped cuprates (right). (b) Phase diagram of the cuprate superconductors. The horizontal axis is the doping level of holes (left) or electrons (right).

1.2 Electronic structure and physical properties

Superconductivity induced by electron doping in copper oxides was first found in $Nd_{2-x}Ce_xCuO_4$ with $x = 0.15$ [1]. The electron-doped cuprates are peculiar in the sense that superconductivity is realized only after annealing. As-grown samples are AF and annealing Ce-substituted samples induces superconductivity typically below 20 K. The roles of the annealing are summarized in the next section.

After the discovery of $Nd_{2-x}Ce_xCuO_4$, superconductivity was achieved in various $Ln_{2-x}Ce_xCuO_4$ systems. With varying the lanthanoid Ln, the in-plane lattice constant changes systematically as shown in Fig. 1.2(a) due to the different ionic radii of the lanthanides atoms. The superconducting (SC) properties is also dependent on the lanthanoid. One can find a trend from Fig. 1.2 that T_c becomes higher and superconductivity can be realized with lower Ce concentration with increasing ionic size of the lanthanoid. On the other hand, antiferromagnetism becomes more robust with decreasing ionic size. Thus, antiferromagnetism and superconductivity compete with each other in these systems. Considering these facts, $La_{2-x}Ce_xCuO_4$ is the best superconductor among the electron-doped cuprates. However, La_2CuO_4 tends to take the T-type structure and it is impossible to synthesize crystals of electron-doped $La_{2-x}Ce_xCuO_4$ with the T'-type structure. One way to stabilize T'-$La_{2-x}Ce_xCuO_4$ is fabricating thin films and using the epitaxial strain from the substrate [3]. Another way to stabilize the T' structure is the partial substitution of Pr for La. Single crystals of $Pr_{2-y-x}La_yCe_xCuO_4$ have thus been successfully synthesized [4].

The parent compounds of the cuprate superconductors are regarded as charge-

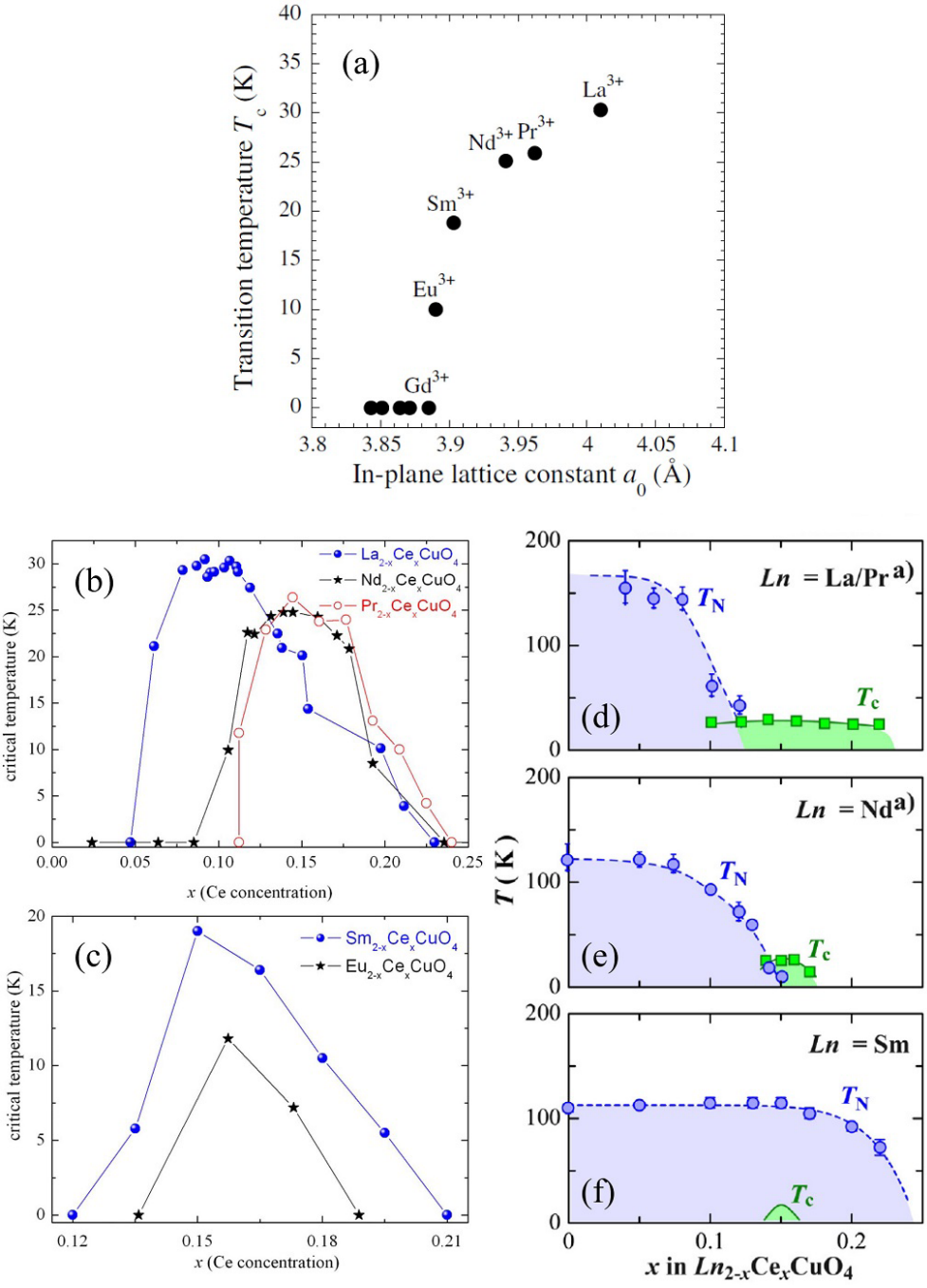

Figure 1.2: Lanthanoid dependence of the SC properties of $Ln_{2-x}Ce_xCuO_4$. (a) In-plane lattice constant and maximum T_c achieved in thin films of $Ln_{2-x}Ce_xCuO_4$ synthesized using molecular beam epitaxy (MBE) [3]. (b), (c) T_c plotted against Ce content x in thin films of $Ln_{2-x}Ce_xCuO_4$ synthesized using MBE [5]. Note that the scale of the horizontal axis is different between (b) and (c). (d)-(f) T_c and the Néel temperature T_N plotted against x in bulk $Ln_{2-x}Ce_xCuO_4$ [6].

transfer insulators in the Zaanen-Sawatzky-Allen diagram [7]. The half-filled Cu $3d_{x^2-y^2}$ orbital, which has the highest energy among the five $3d$ orbitals, splits into the upper and lower Hubbard bands (UHB and LHB) due to the strong on-site Coulomb repulsion U, and the oxygen $2p$ band resides between the UHB and LHB separated from the UHB by the charge-transfer gap $\Delta_{\rm CT}$ as shown in Fig. 1.3(a). When holes are introduced in the oxygen $2p$ band, the holes at the Cu site and that in the molecular orbital of a linear combination of four surrounding oxygen atomic orbitals strongly hybridize, and form a singlet called Zhang-Rice singlet (ZRS) [8] with the Cu^{2+} spin. This singlet state can be defined around each Cu site but is not orthogonal to each other. Then, regarding the singlet state as an empty state surrounding the Cu d hole, one can write a Hamiltonian using only the operators of the oxygen holes of the Cu d symmetry. Consequently, the ZRS band can be regarded as an effective LHB at the Cu site with the effective Coulomb repulsion $U_{eff} = \Delta_{\rm CT}$ as shown in Fig. 1.3(b). The electronic structure of the cuprate superconductors have often been discussed based on this one-band Hamiltonian.

The charge-transfer (CT) gap energy $\Delta_{\rm CT}$ can be observed by optical measurements and it has been found that Nd_2CuO_4 has a CT gap of $\Delta_{\rm CT} \sim 1.5$ eV [9, 10], smaller than $\Delta_{\rm CT} \sim 2.0$ eV of the parent compound La_2CuO_4 of hole-doped cuprates. The smaller $\Delta_{\rm CT}$ originates from the weaker Madelung potential at the Cu site due to the lack of the O atoms at the apical site. While optical measurements mainly probe direct gaps, momentum-resolved measurements such as angle-resolved photoemission spectroscopy (ARPES) enable us to estimate a gap including indirect ones. ARPES measurements have revealed that while the ZRS band takes the maximum at momentum $(\pi/2, \pi/2)$, the UHB takes the minimum at $(\pi, 0)$ or $(0, \pi)$ [11, 12]. Thus, the indirect gap is smaller than the direct one observed by optical measurements. In the case of electron-doped cuprates, the indirect gap may be as small as 0.5 eV as shown in Fig. 1.4 [13].

One of the anomalous features of the hole-doped cuprates is the temperature dependence of the resistivity. While the resistivity of a normal Fermi liquid shows a T^2 temperature dependence, that of the hole-doped cuprates shows a linear dependence in the optimally doped region. ARPES studies have also revealed a linear temperature and energy dependences of the imaginary part of the self energy, $\mathrm{Im}\Sigma$, corresponding to the linear temperature dependence of the resistivity [14,15]. These peculiar behaviors have been well reproduced by the phenomenology of a marginal Fermi liquid [16,17]. On the other hand, the temperature dependence of the resistivity of electron-doped cuprates is basically expressed as $(T/T_{\rm F})^2 \ln(T_{\rm F}/T)$, where $T_{\rm F}$ denotes the Fermi temperature: the Fermi-liquid-like T^2 behavior with a logarithmic correction due to the two dimensional nature of the system [18, 19]. Thus, the electron-doped cuprates have been regarded as rather "normal" than hole-doped cuprates.

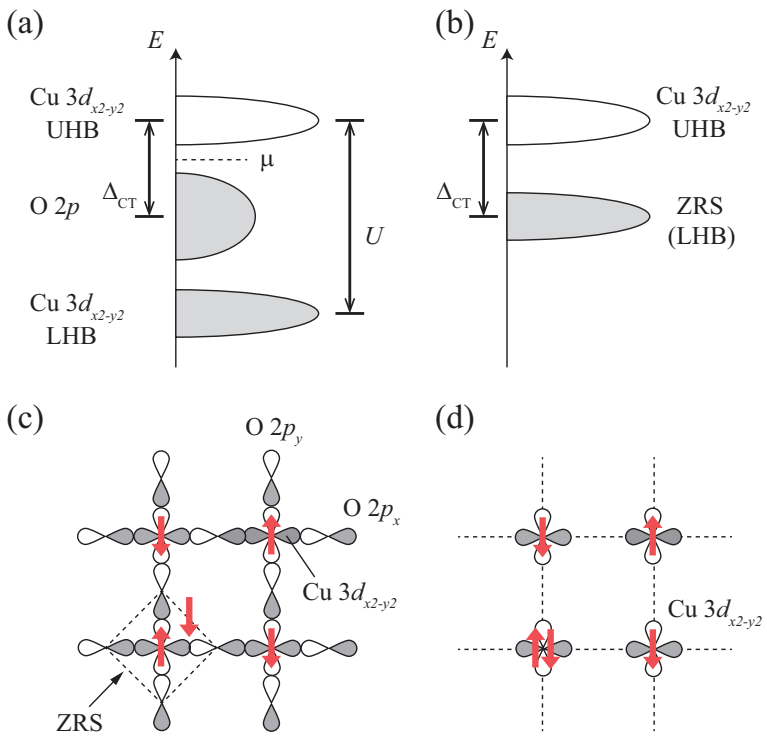

Figure 1.3: Schematic picture of the electronic structure of cuprate superconductors. (a) Energy diagram when the oxygen $2p$ band is explicitly considered, and (b) when one band approximation is applied. Illustrations of the Zhang-Rice singlet (ZRS) formation when the oxygen $2p$ band is explicitly considered (c), and when one-band approximation is applied (d).

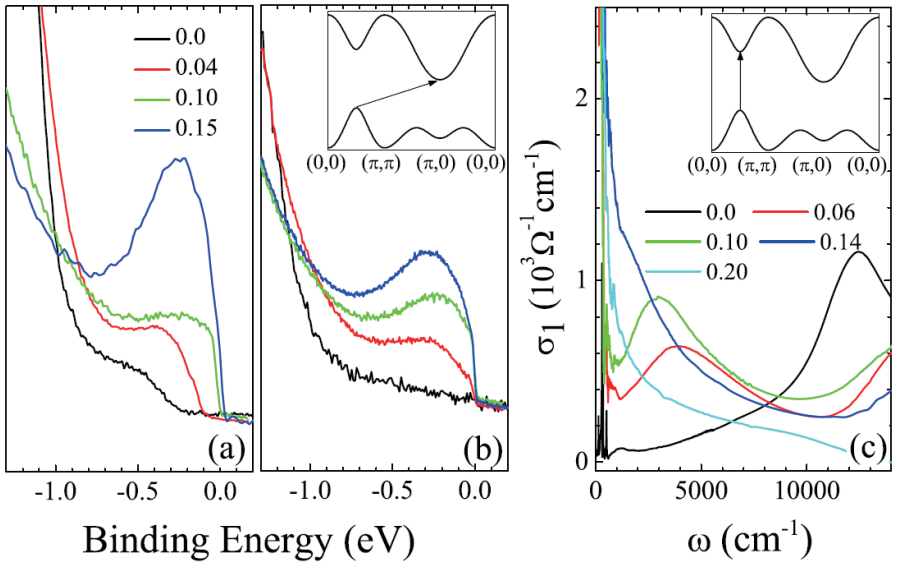

Figure 1.4: ARPES and optical spectra of $Nd_{2-x}Ce_xCuO_4$ [13]. (a),(b) ARPES spectra near $(\pi/2, \pi/2)$ and $(\pi, 0)$, respectively. In (a), the spectrum of Nd_2CuO_4 maintains a finite intensity up to ~ 0.5 eV below E_F. (c) Optical conductivity in the infrared region. Insets of (b) and (c) illustrate indirect and direct excitations.

1.3 Role of annealing

Annealing in a reducing atmosphere plays an essential role in realizing the superconductivity in the electron-doped cuprates. As-grown samples are non-SC antiferromagnets, and superconductivity appears only after annealing. A large impact of annealing on the long-range AF order or AF fluctuations will be discussed in the next section. Annealing is typically conducted at a high temperature around 900 K for $10 \sim 24$ hours under a low oxygen pressure, in the flow of gas such as N_2 and Ar or in vacuum. The effect of annealing is directly observed in the oxygen content. The reduction of the sample weight due to the oxygen removal has been observed by thermogravimetric analyses [20,21]. However, the reduction is as small as around ~ 0.07 out of 4 oxygen atoms, and it becomes even smaller (~ 0.01) with increasing Ce content [22, 23]. It is surprising that such a small amount of oxygen reduction critically affects the superconductivity in the electron-doped cuprates. An early-stage neutron scattering measurement has revealed that oxygen atoms exist at the apical sites as impurities in as-grown Nd_2CuO_4, and that their content is significantly reduced by annealing [24, 25]. It has been pointed out that the apical oxygen should significantly perturb the Madelung potential at the Cu site below it [2], and can also polarize the spin around it [26], acting as a strong scattering center. Although this view has been strongly supported historically,

rather recent Raman and crystal-field infrared transmission studies have proposed a different scenario [27, 28]. They detected oxygen atoms at the apical site for $Nd_{2-x}Ce_xCuO_4$ and $Pr_{2-x}Ce_xCuO_4$, but the content did not change by annealing. Instead, oxygen atoms were removed from the LnO (Ln: Lanthanoid) layer at low (0-0.05) Ce-doping, and from CuO_2 planes at higher (> 0.10) doping. There is another scenario which is attracting attentions. A partial decomposition of the materials by annealing has been observed for $Nd_{2-x}Ce_xCuO_4$ by X-ray and neutron scattering measurements, with a new impurity phase of (Nd, Ce)$_2$O$_3$ [29]. This impurity phase has also been found in $Pr_{0.88}LaCe_{0.12}CuO_4$ by Kang *et al.* [30], and they have concluded that defects of Cu atoms in as-grown sample are compensated by creating a new impurity phase of Ln_2O_3 in the course of annealing. It should be noted that Kang *et al.* observed elongation of the c-axis lattice parameter by annealing, whereas according to the studies which claimed removal of apical oxygen atoms, the contraction of the c-axis length has been observed [24, 25]. Difference in the samples might lead to the difference in the annealing effect: if the as-grown sample does not have Cu defects, O atoms are removed (from the apical sites, LnO layers, or CuO_2 planes) and the lattice shrinks in the c direction, and if the as-grown sample contains Cu defects, they are compensated by creating Ln_2O_3, leading to the elongation of the c-axis parameter. Thus, the microscopic description of the annealing process is still controversial and remains elusive.

Since the removal of oxygens could induce electrons on Cu, electron doping by annealing has been discussed. A neutron scattering study has shown that a plot of the Néel temperature T_N of annealed samples against the Ce content x corresponds to that of as-grown one rigidly shifted by $\Delta x \sim 0.03$ [31] [Fig. 1.5(a)], suggesting additional electron doping through annealing although T_N is not the quantity which is entirely controlled by carrier concentration. On the other hand, the difference between annealing and Ce doping has been reported in some previous studies. The oxygen-content dependence of the resistivity has been measured for the overdoped $Pr_{2-x}Ce_xCuO_4$ by varying the annealing condition [32]. If the oxygen reduction simply means electron doping, it is expected that the more oxygen is reduced, the more T_c is lowered because of the further overdoping. However, actually the T_c is enhanced and the residual resistivity is decreased with reducing the oxygen content [Fig. 1.5(b)]. This suggests that the oxygen reduction suppresses the scattering of quasi-particles significantly rather than simply dopes electrons to drive superconductivity. The temperature dependence of the Hall coefficient also shows a different behavior according to the change of the Ce concentration or oxygen content, indicating a different role of the oxygen reduction from the simple electron doping as shown in Fig. 1.5(c) [33]. Thus, annealing introduces many effects on the electronic structure and the detail is still unclear.

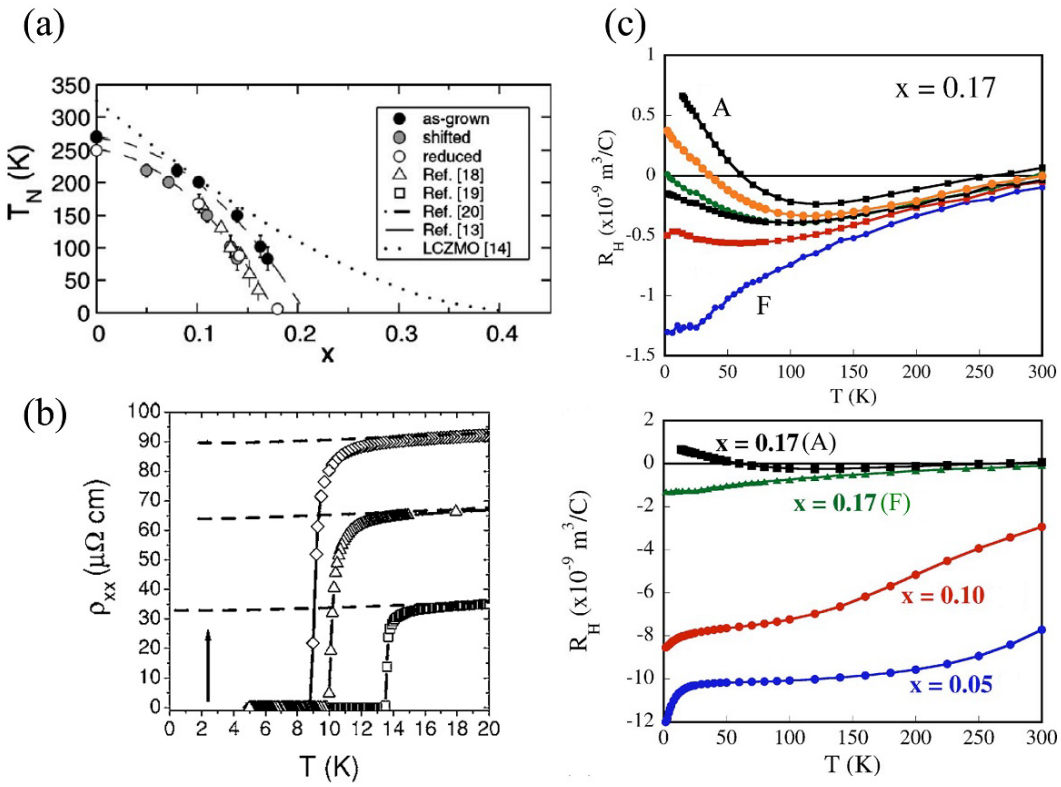

Figure 1.5: Annealing dependence of physical properties of the electron-doped cuprates. (a) Néel temperature $T_{\rm N}$ plotted against x in $Nd_{2-x}Ce_xCuO_4$ [31]. The curve of the annealed sample can be reproduced by rigidly shifting that of the as-grown one by $\Delta x \sim 0.03$. (b) In-plane resistivity of $Pr_{1.83}Ce_{0.17}CuO_4$ thin films annealed under various conditions [32]. Samples are annealed in $1 \times 10^{-4}(\square)$, $1 \times 10^{-3}(\triangle)$ and $2.3 \times 10^{-3}(\diamond)$ Torr of N_2O. (c) Temperature dependence of Hall coefficient $R_{\rm H}$ of $Pr_{2-x}Ce_xCuO_4$ thin films annealed under various conditions (top), or x (bottom) [33]. In the top panel, x is fixed at 0.17, and the oxygen content is increased from samples A to F.

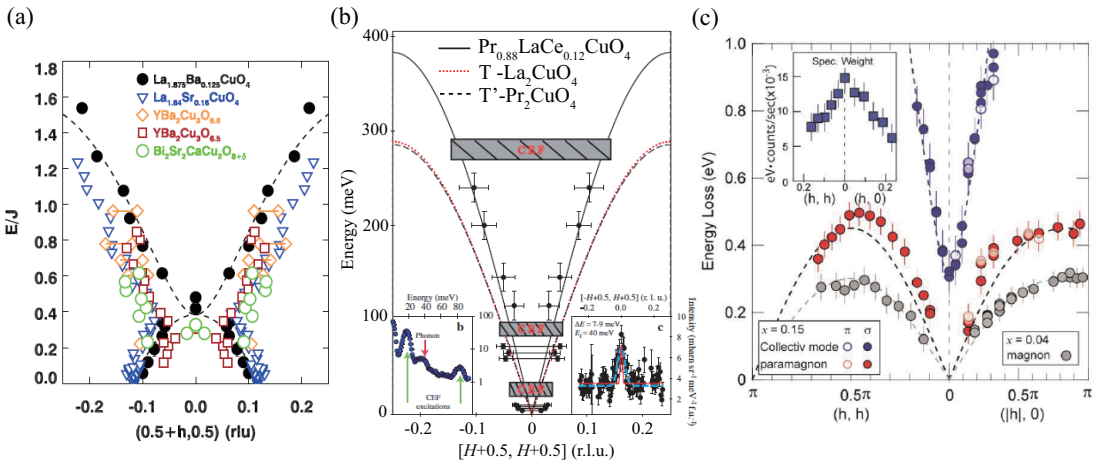

Figure 1.6: Momentum dispersions of magnetic excitations in cuprate superconductors. (a) Dispersions in various hole-doped cuprate superconductors observed by neutron scattering [34]. The vertical axis is the energy measured in units of J for each AF parent compound. (b) Dispersion in SC $Pr_{0.88}LaCe_{0.12}CuO_4$, AF T'-$Pr_2CuO_4$, and AF T-$La_2CuO_4$ observed by neutron scattering [35]. (c) Dispersions in $Nd_{2-x}Ce_xCuO_4$ ($x = 0.04$ and 0.15) observed by resonant inelastic X-ray scattering [36].

1.4 Antiferromagnetic pseudogap

Magnetic fluctuations have been considered to be intimately related to the superconductivity in the cuprate superconductors, and investigated by neutron scattering measurements. In both electron- and hole-doped cuprates, a gap opens in the magnetic excitation below T_c due to the opening of the SC gap [37] and the missing spectral weight piles up near the gap edge [35, 38]. This enhancement of magnetic excitation is called "spin resonance", and the energy of the peak position universally follows $E_{\rm peak} = 1.3\Delta$ (Δ: SC gap) irrespective of the system including iron-based superconductors and heavy-fermion superconductors [39]. A big difference between the electron- and hole-doped cuprates can be found in the dispersion of the excitation. In the hole-doped cuprates, a so-called hour-glass dispersion has been observed universally as shown in Fig. 1.6(a) [34]. The incommensurate low energy part seems associated with the particle-hole excitation with a finite spin gap [40], while the dispersion in the higher energy part can be regarded as a spin-wave excitation of the remnant local AF moment coupled with nearest-neighbors through exchange interaction $J \sim 0.1$ eV. On the other hand, the excitation in the electron-doped cuprates is basically commensurate at low energies as shown in Fig. 1.6(b) and (c) regardless of whether the sample is AF or SC [35, 36]. A simple Fermi-liquid treatment in the random phase approximation (RPA) using

an experimentally obtained band structure has failed to reproduce the commensurate excitation in the low energy region [41], suggesting a localized character of the spin excitation. In addition, inelastic neutron scattering studies have revealed that the spectral weight of low-energy spin excitation does not change significantly over the wide electron-doping range of 0.07-0.18 (AF insulating to overdoped SC states) [42]. Thus, a localized spin character strongly remains in the low energy region even throughout the whole phase diagram in electron-doped cuprates [34].

AF correlation persists up to the optimal doping in the electron-doped cuprates and profoundly affects their electronic structure. From the underdoped to optimally doped regions of the electron-doped cuprates, a band gap opens even in the SC state due to AF ordering or correlation. This pseudogap has been observed as a dip-like feature in the optical conductivity [10, 43] [Fig. 1.7(a)] or peaks at higher bias voltages in the scanning tunneling spectrum [44] [Fig. 1.7(b)]. Angle-resolved photoemission (ARPES) studies have shown a pseudogap opening around the "hot spots", crossing points between the Fermi surface and the boundary of the AF Brillouin zone (BZ) [Fig. 1.7(c)] [45–51]. In Fig. 1.8(a), the pseudogaps of hole- and electron-doped cuprate superconductors are compared. The pseudogap of hole-doped cuprates opens around (π, 0) and (0, π), and its origin is still unclear despite extensive studies. On the other hand, the pseudogap of electron-doped cuprates opens at the "hot spots", and its origin is considered to be AF correlation or AF short-range order. When spins are ordered or fluctuating with the (π ,π) wave vector, the system has a $\sqrt{2} \times \sqrt{2}$ superstructure, and its BZ is reduced as shown in Fig. 1.8(a). Consequently bands along the new BZ boundary split and an energy gap opens at the "hot spot" [Fig. 1.8(b)].

The overall band structure is basically consistent with that calculated using the tight-binding model of the square lattice consisting of the Cu $3d_{x^2-y^2}$ orbitals with the $\sqrt{2} \times \sqrt{2}$ AF order,

$$\begin{aligned}\epsilon - \mu =& \epsilon_0 \pm \sqrt{\Delta_{AF}^2 + 4t^2(\cos\, k_x a + \cos\, k_y a)^2} \\ & - 4t' \cos\, k_x a \, \cos\, k_y a - 2t"(\cos\, 2k_x a + \cos\, 2k_y a),\end{aligned} \tag{1.1}$$

where t, t', and t" are transfer integrals between the nearest-neighbor, second-nearest-neighbor, and third-nearest-neighbor Cu sites, respectively. $2\Delta_{\mathrm{AF}}$ represents the potential deference between the two spin sublattices. However, the magnitude of Δ_{AF} was shown to decrease with approaching antinodal region [46], and could be regarded as zero at (0, π) and (π, 0) as reported by Ikeda *et al.* [50]. One possibility is that Δ_{AF} is actually momentum dependent as predicted by a variational Monte Carlo study by Chou and Lee [52]. Another explanation was raised by Park *et al.* [47] focusing on the absence of band folding in the antinodal region that, besides the AF bands, a paramagnetic band disperses uninterrupted through the AF BZ boundary because antiferromagnetism is inhomogeneous and

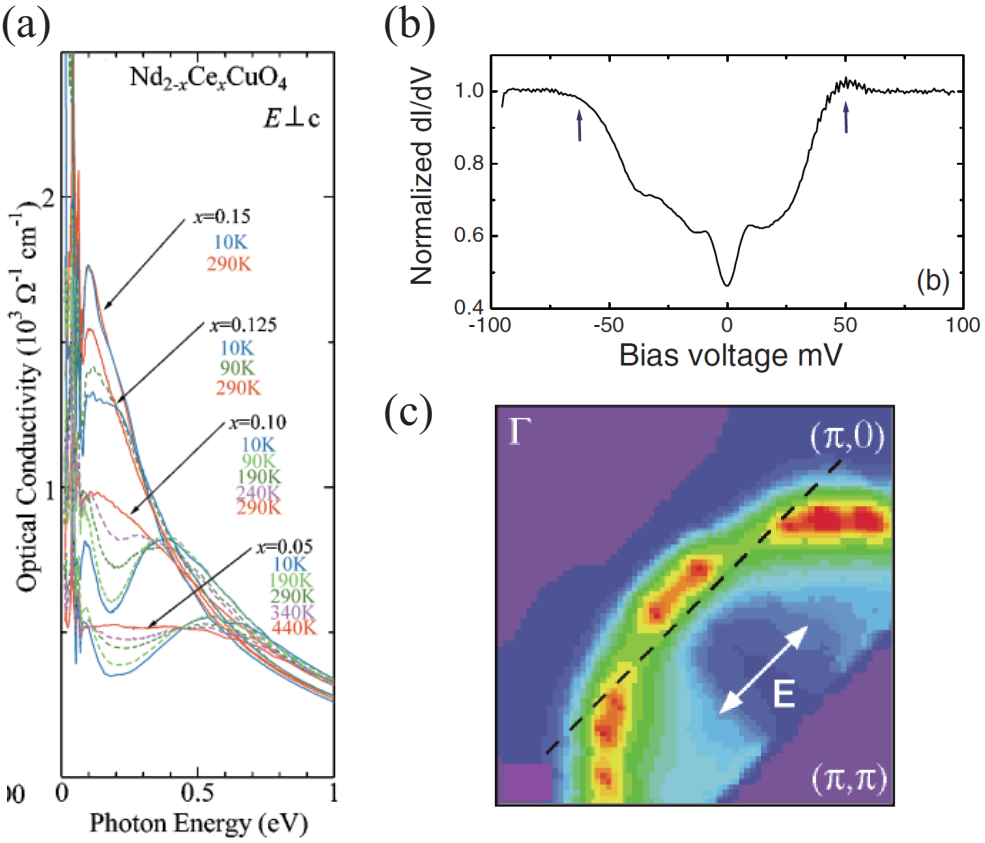

Figure 1.7: AF pseudogap observed by various experimental probes. (a) Optical-conductivity spectra of $Nd_{2-x}Ce_xCuO_4$ [43]. Dip features around 0.2 eV correspond to the AF pseudogap. (b) Tunneling spectrum of $Sr_{1.85}Ce_{0.15}CuO_4$ [44]. An AF pseudogap opens between two peaks indicated by arrows. (c) Fermi surface of $Nd_{1.85}Ce_{0.15}CuO_4$ measured by ARPES. [45]. Intensity is suppressed at the "hot spots" (explained in the text), indicating the opening of an AF pseudogap at those points.

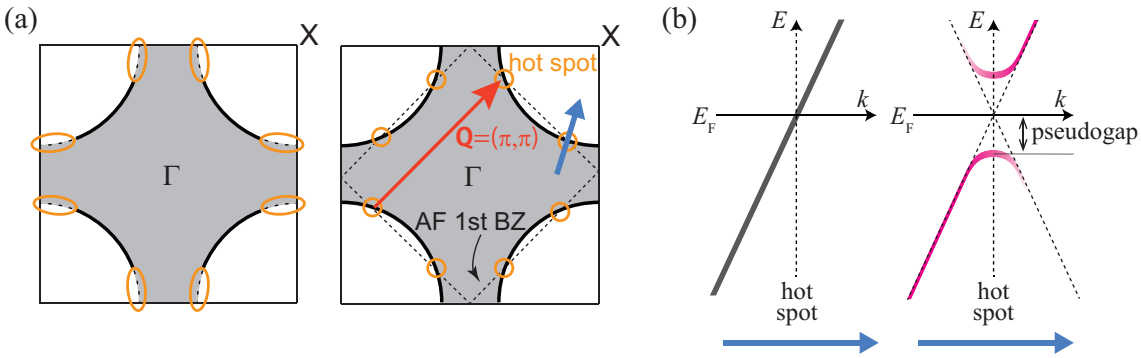

Figure 1.8: Schematic explanation of the AF pseudogap in the electron-doped cuprates. (a) Fermi surface of a hole-doped cuprate (left) and an electron-doped cuprates (right). Momentum region where the pseudogap is observed is indicated by orange circles. (b) Band dispersion along the line indicated by the blue arrow in (a) without and with AF correlation (left and right, respectively) in the electron-doped cuprates.

short-ranged, causing the apparent reduction of Δ_{AF} in the antinodal region. The nature of the AF pseudogap thus remains elusive.

Annealing process plays a crucial role in the competition between antiferromagnetism and superconductivity. ARPES studies have revealed that the annealing reduces the intensity of the AF-folded bands and that the spectral intensity generally increases at E_{F} [49,51,53] as shown in Fig. 1.9. Nevertheless, the pseudogap of the AF origin at the "hot spots" has been seen in all the electron-doped cuprates from the underdoped to overdoped regions studied so far as shown in Fig. 1.10 [48]. Therefore, the AF pseudogap has been regarded as a hallmark of the electron-doped cuprates and the relationship between the antiferromagnetism and superconductivity has been considered as an essential ingredient of the electron-doped cuprates.

The coexistence of antiferromagnetism and superconductivity in the electron-doped cuprates has been discussed for a long time. A neutron scattering study has revealed that spin stiffness goes to zero at the boundary between the AF and SC phases in $Nd_{2-x}Ce_xCuO_4$, and a genuine long-range AF order does not coexist with superconductivity [54]. Park *et al.* [47] has explained the band structure of the SC $Sm_{1.85}Ce_{0.15}CuO_4$ by considering a short-range AF order. On the other hand, another ARPES study has shown that the disconnected Fermi surface forms a hole pocket around $(\pi/2, \pi/2)$ in the SC $Sm_{1.85}Ce_xCuO_4$, and concluded that a quasi-long-range antiferromagnetism coexists with superconductivity [55]. The

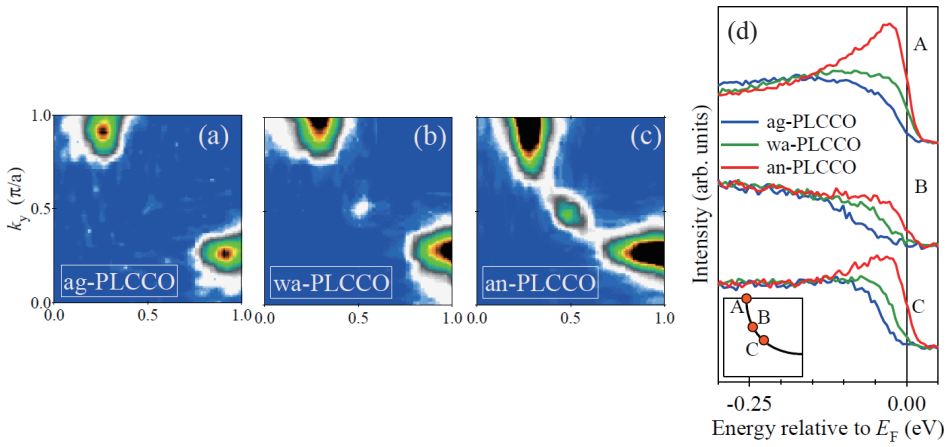

Figure 1.9: Annealing dependence of the pseudogap in $Pr_{1.3-x}La_{0.7}Ce_xCuO_4$ ($x = 0.12$) observed by ARPES [53]. (a)-(c) Fermi surfaces of as-grown, weakly annealed, and well annealed samples, respectively. Weakly annealed and well annealed samples are annealed in Ar flow at 925 °C for 24 hours and in N_2 flow at 925 °C for 24 hours, respectively. (d) EDC's of the three samples at the momenta indicated in the inset.

existence of the small hole pocket is also confirmed by the quantum oscillation in the SC $Pr_{2-x}Ce_xCuO_4$ [56, 57]. Thus, the AF correlation is so robust that a quasi-long-range antiferromagnetism coexists with superconductivity and opens a pseudogap at all the doping levels in electron-doped cuprates.

1.5 Superconducting gap

The symmetry of the SC gap provides a strong clue for the origin of unconventional superconductivity and has been intensively studied for the cuprate, heavy-fermion, and organic superconductors. It is now firmly established that the SC gap of the hole-doped cuprate superconductors have *d*-wave symmetry [58, 59]. While the penetration depth of the hole-doped cuprates exhibits a clear linear temperature dependence [60], consistent with the *d*-wave symmetry of the SC gap, early-stage penetration-depth studies on the electron-doped cuprates $Nd_{2-x}Ce_xCuO_4$ showed an exponential temperature dependence [61, 62], and hence the electron-doped cuprates was regarded as a BCS-like *s*-wave superconductor. However, Cooper [63] have shown that the penetration depth of $Nd_{2-x}Ce_xCuO_4$ is affected by paramagnetism arising from Nd^{3+} ions and shows power-low behavior associated with (dirty) *d*-wave superconductors [63]. Although some penetration-depth studies still claim *s*-wave symmetry [64], most of the previous studies including phase-sensitive measurements have supported *d*-wave symmetry [65–69]. Fur-

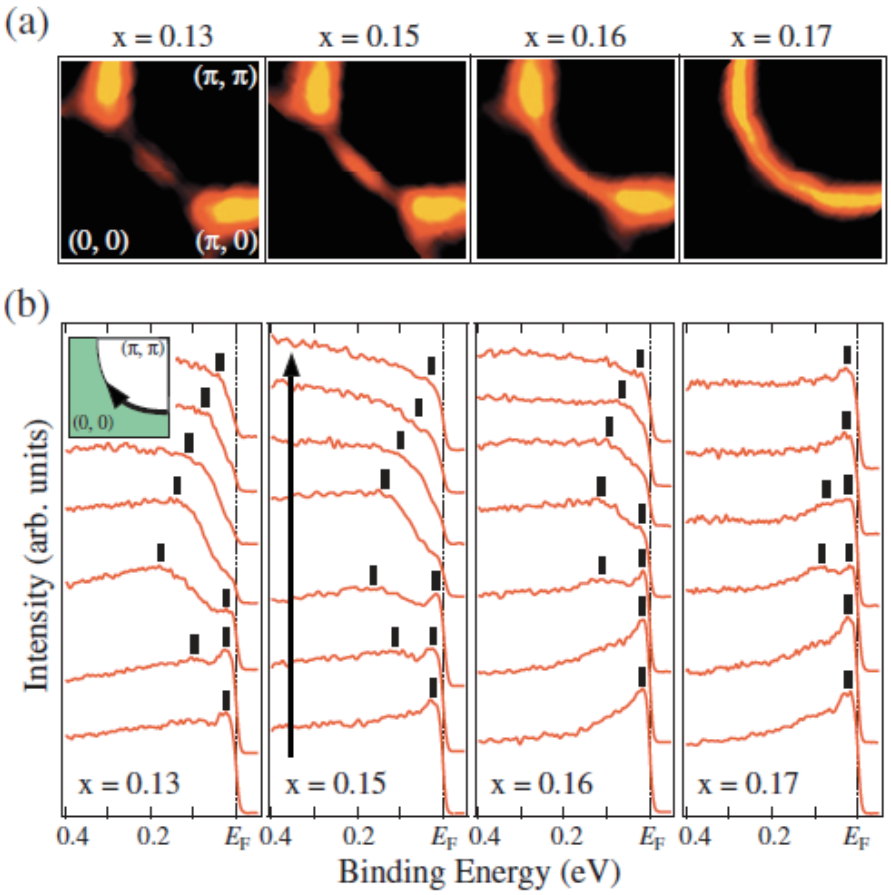

Figure 1.10: Doping dependence of the pseudogap in $Nd_{2-x}Ce_xCuO_4$ observed by ARPES [48]. The samples were annealed at 920 °C for 12 hours in Ar flow. (a) Fermi surfaces. (b) Energy distribution curves along the Fermi surface as shown in the inset. The positions of the peaks or humps are denoted by black bars. Band splitting is due to AF correlation and is observed even in the overdoped sample of $x = 0.17$.

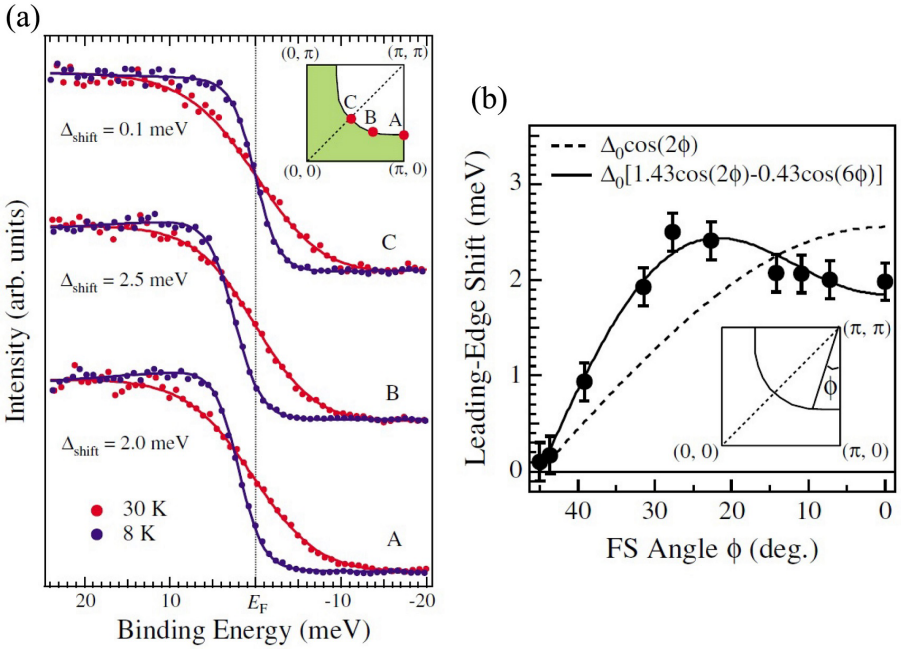

Figure 1.11: SC gap of $Pr_{1-x}La_{0.7}Ce_xCuO_4$ ($x = 0.11$) measured by ARPES. [69] (a) ARPES spectra taken below and above T_c at three momentum positions indicated in the inset. (b) Magnitude of the leading-edge shift plotted against Fermi surface angle defined in the inset.

thermore, Raman scattering [68] and angle-resolved photoemission spectroscopy (ARPES) [69] studies have revealed that the SC gap exhibits not only the simple $d_{x^2-y^2}$-wave momentum dependence but also a maximum near the hot spot, where antiferromagnetic (AF) Brillouin zone boundary and Fermi surface cross each other (Fig. 1.11), and large contribution of AF spin fluctuations to the superconductivity has been proposed.

1.6 New electron-doped cuprate superconductors

As mentioned in section 1.3, the annealing process is a crucial factor for superconductivity in the electron-doped cuprates, and the SC properties depend on the annealing condition. Kim *et al.* [23] annealed a polycrystalline $Nd_{1.85}Ce_{0.15}CuO_4$ sample in vacuum with varying temperature and oxygen pressure. They have shown that higher temperature and lower oxygen pressure led to the decomposition of the sample, but the highest T_c was achieved when the sample was close to the limit of decomposition. This suggests the possibility that T_c is further enhanced if one can avoid the decomposition even under a severe annealing condition.

Brinkmann *et al.* [70] annealed thin single crystals of $Pr_{2-x}Ce_xCuO_4$ sandwiched by $Pr_{2-x}Ce_xCuO_4$ polycrystals in order to protect the samples from decomposition. The samples were annealed at 1080 °C for 72 hours, at higher temperature and for much longer time than usually used, and superconductivity was successfully realized with the Ce concentration as low as 4% , where the sample had been considered to be AF as shown in Fig. 1.12(a).

Recently in thin films [Fig. 1.12(b)] [19, 71, 73, 77–86] and powdered samples [Fig. 1.12(c)] [72,87] of electron-doped cuprates, superconductivity has been found even without Ce substitution. Surprisingly, T_c goes up with decreasing Ce concentration x, achieving the highest T_c at $x = 0$ as shown in Fig. 1.13(a). This superconductivity at $x = 0$ can be attributed to the effectiveness of annealing in thin films and powdered samples, that is, oxygen can diffuse more easily in those systems than in single crystals.

Systematic measurements of the resistivity have been done on $La_{1.85}Y_{0.15}CuO_4$ thin films, which become SC without Ce, with varying annealing conditions [Fig. 1.13(a)-(c)] [73]. With decreasing oxygen partial pressure, increasing annealing temperature, and increasing annealing time, insulating sample becomes metallic and superconductivity eventually emerges. This change is similar to that induced by Ce doping [Fig. 1.13(d)]. However, excessive annealing (too high temperature or too long time) leads to the increase of resistivity and the degradation of superconductivity [Fig. 1.13(b),(c)], whereas the suppression of superconductivity by overdoping should be accompanied by the decrease of the resistivity, suggesting that the effect of annealing is different from Ce doping. Tsukada *et al.* [73] have claimed that moderate annealing removes apical oxygen atoms and induce superconductivity, but oxygen atoms in the CuO_2 planes also diffuse out by excessive annealing, which increases the resistivity and suppresses the superconductivity rapidly, and hence superconductivity occurs without oxygen defects in CuO_2 planes, that is, without any electron doping. Electron doping level of the SC parent compound has also been discussed from the viewpoint of the lattice constant. Since the Cu-O bond has antibonding character [88], the in-plane lattice constant increases when electrons are doped into the CuO_2 plane as shown in Fig. 1.14(a) [75]. However, the in-plane lattice constant of $La_{1.85}Y_{0.15}CuO_4$ was independent of the oxygen pressure during annealing, that is, of the oxygen content in the sample [Fig. 1.14(b)], although the sample changed from an insulator to a superconductor with decreasing oxygen pressure as shown in Fig. 1.13(a). This suggests that the superconductivity in the parent compound of the electron-doped cuprates might occur exactly at half filling without additionally doped electrons through the removal of oxygen.

From a theoretical point of view, dynamical mean-field theory (DMFT) studies have claimed that the band gap seen in the parent compound of the electron-doped cuprates is not a charge-transfer gap, but a gap opened due to the AF correlation as shown in Fig. 1.15, and have classified electron-doped cuprates as Slater insulators,

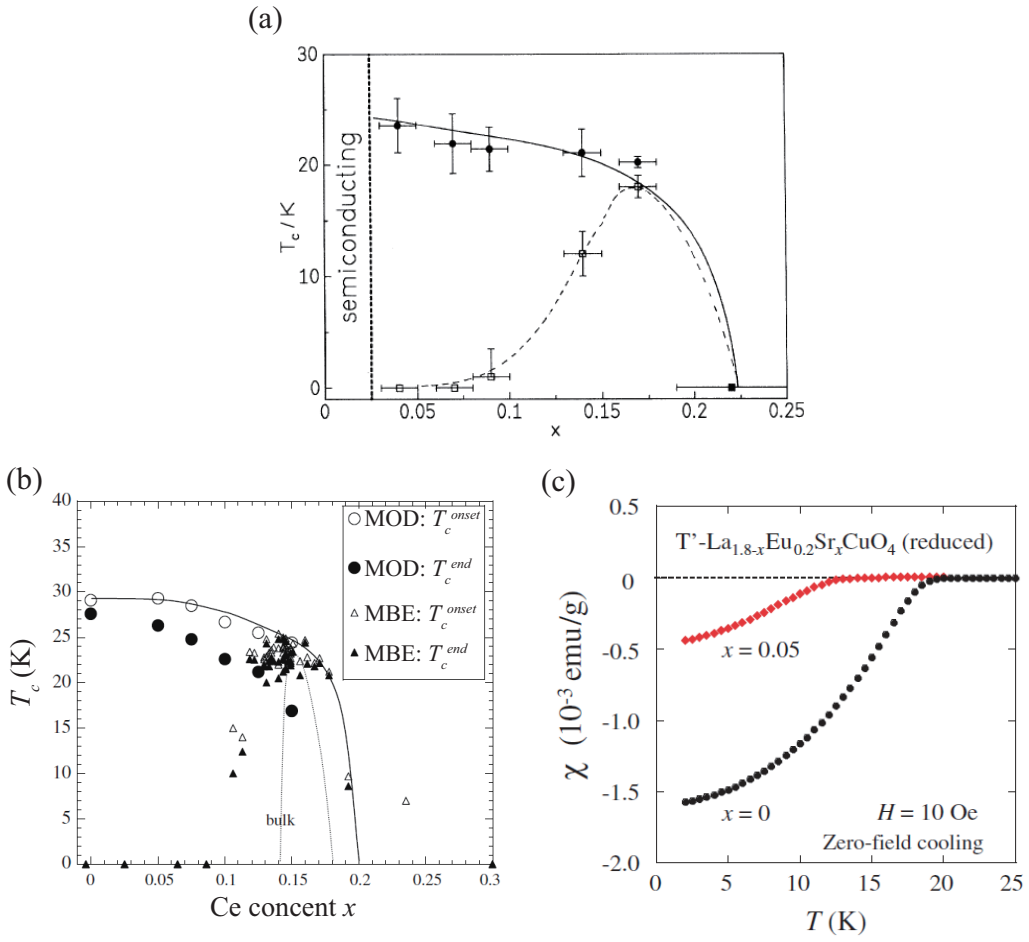

Figure 1.12: Superconductivity with low or zero Ce concentration in electron-doped cuprates. (a) Phase diagram of thin single-crystalline $Pr_{2-x}Ce_xCuO_4$ annealed at 1080 °C for 72 hours with its top and bottom covered with two polycrystalline pellets of the same composition (solid line), and annealed at 950 °C for 10 hours without the pellets (dashed line) [70]. The sample annealed with the pellets shows superconductivity with Ce concentration as low as 0.04. (b) Phase diagram of $Nd_{2-x}Ce_xCuO_4$ thin films grown by MBE or metal organic deposition (MOD) [71]. The sample grown by MOD achieves superconductivity at $x = 0$. (c) Magnetic susceptibility of T'-$La_{1.8-x}Eu_{0.2}Sr_xCuO_4$ plotted against temperatures [72]. The sample with $x = 0$ shows superconductivity without electron doping by Ce substitution.

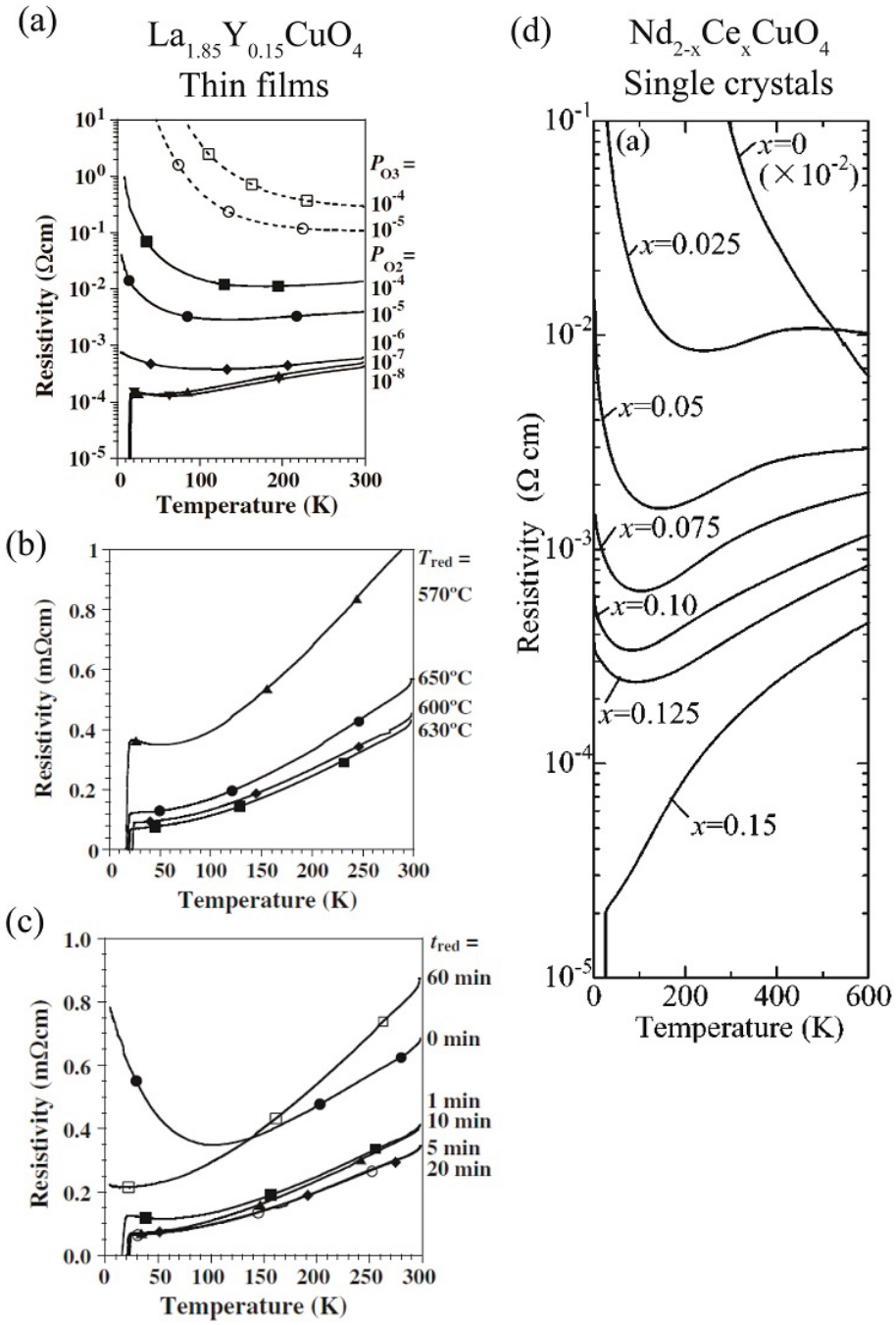

Figure 1.13: Resistivity of electron-doped cuprates which can be SC without Ce substitution. (a-c) Temperature dependence of the resistivity of $La_{1.85}Y_{0.15}CuO_4$ thin films annealed with varying (a) oxygen partial pressure, (b) temperature, and (c) time [73]. (d) Temperature dependence of the resistivity of annealed $Nd_{2-x}Ce_xCuO_4$ single crystals [74].

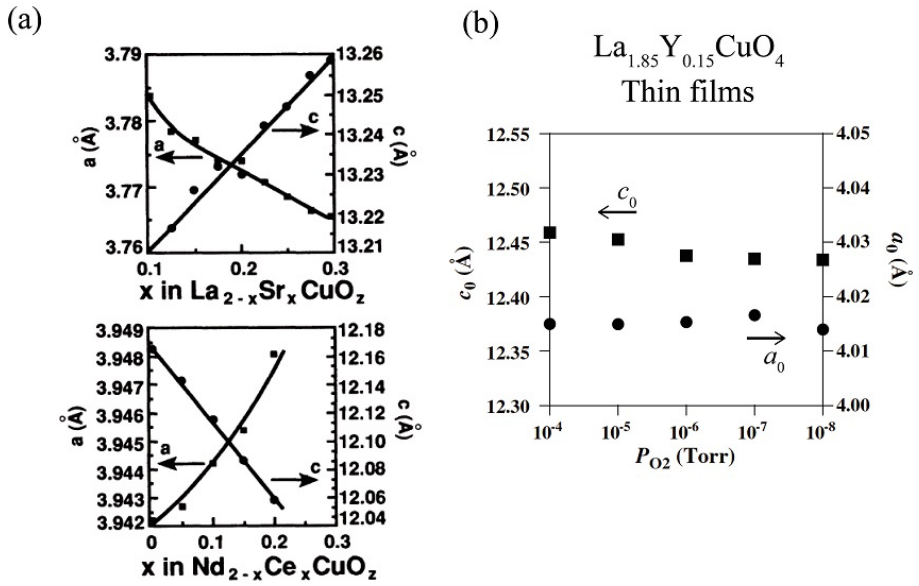

Figure 1.14: Effects of Ce doping and annealing on the lattice constant of electron-doped cuprates. (a) Lattice constants a and c plotted against x for $La_{2-x}Sr_xCuO_4$ (top) and $Nd_{2-x}Ce_xCuO_4$ (bottom) [75]. (b) Lattice constants a_0 and c_0 plotted against the oxygen pressure during annealing [73]. Samples annealed in 10^{-4}, 10^{-5}, and 10^{-6} Torr of oxygen are insulating, and those in 10^{-7} and 10^{-8} Torr are SC as shown in Fig. 1.13 (a).

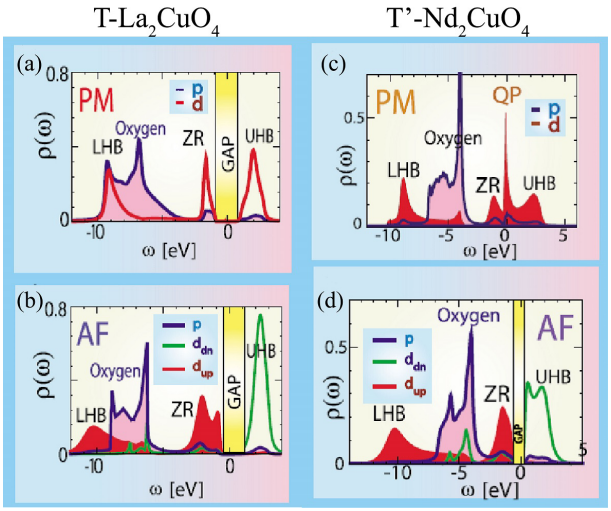

Figure 1.15: LDA + DMFT calculation for the parent compounds of the cuprate superconductors [76]. (a),(b) Calculated density of states of T-La_2CuO_4 in paramagnetic and AF states, respectively. (c),(d) The same as (a) and (b) for T'-Nd_2CuO_4.

and not charge-transfer insulators [76,89]. This result originates from the relatively weak correlation in the electron-doped cuprates, and suggests that the band gap might be closed if the AF correlation could be sufficiently suppressed.

Inspired by the recent discovery of superconductivity without Ce substitution, Adachi *et al.* further improved the annealing method of Brinkmann *et al.* [70], and annealed large bulk single crystals of $Pr_{1.3-x}La_{0.7}Ce_xCuO_4$ ($x = 0.10$) at 800 °C for 24 hours in a vacuum of 10^{-6} Torr with the sample surfaces covered by powders of the same materials with the same compositions [90] [Fig. 1.16 (c)]. They call this new annealing method "protect annealing" method. Although the samples with such a low Ce concentration have not shown superconductivity in previous studies by Sun *et al.* [91] [Fig. 1.16(a)], their samples showed a T_c as high as 27.0 K, even higher than the T_c's of $Pr_{1.3-x}La_{0.7}Ce_xCuO_4$ with higher Ce concentrations, as shown in Fig. 1.16 (b) and (d).

We have previously performed ARPES measurements of PLCCO ($x = 0.10$) single crystals provided by Adachi *et al.* with varying annealing conditions [92,93]. While the as-grown sample showed a large pseudogap, the gap was strongly weakened and became unrecognizable unlike all the other previous ARPES studies, suggesting dramatic reduction of the AF correlation length and/or the magnetic moment by protect annealing. Electron concentration n_{FS} estimated from Fermi surface area ranged from 0.12 to 0.18, which was typically larger than the Ce concentration x. This suggests that samples were doped with excess electrons probably due to oxygen deficiency induced by protect-annealing. While Ce overdoping suppresses T_c rapidly, however, the protect-annealed samples maintain high T_c up to the electron concentration as high as 0.18, suggesting that the protect annealed samples posses larger SC dome than conventionally annealed samples. In order to reveal the effect of protect annealing in more detail, systematic studies with varying both Ce concentration and annealing conditions are required.

1.7 Motivation

The recent studies on electron-doped cuprates have experimentally demonstrated that efficient annealing can induce superconductivity in the parent compound of thin films [19,71,73,77–86] and powdered samples [72,87], and in heavily underdoped ($x \sim 0.05$) bulk single crystals [90], but the electronic structure of those new electron-doped cuprate superconductors is under intense debate. The most critical issue is whether the superconductivity in the parent compounds occurs without any carrier doping or not. It has been claimed that the superconductivity indeed occurs without carrier doping based on the changes in the resistivity and the lattice constant induced by annealing as described in section 1.6. It may be true that excessive annealing creates so many oxygen defects that superconductiv-

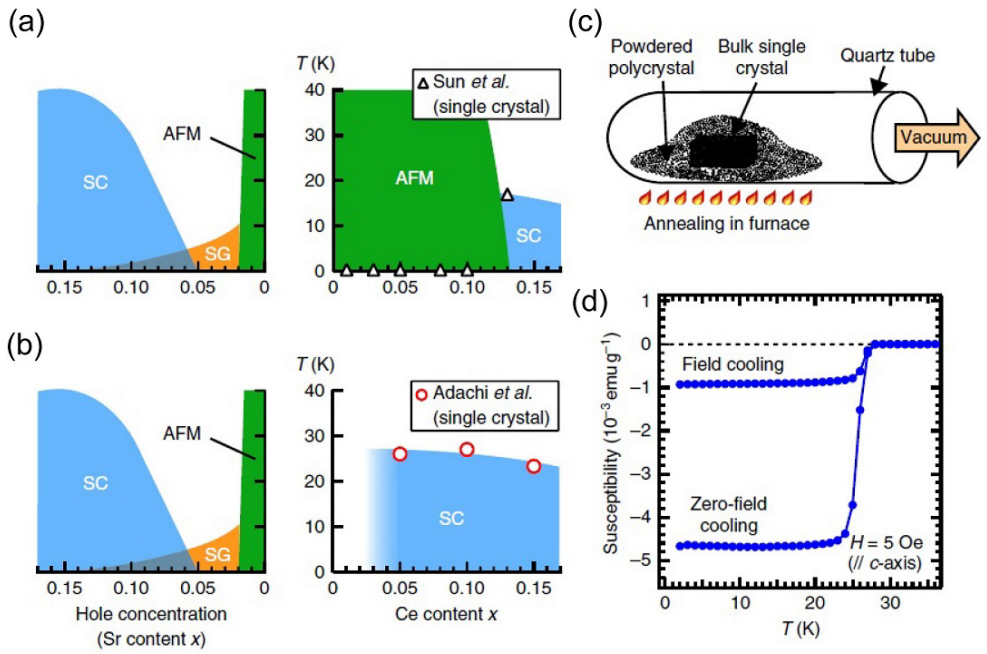

Figure 1.16: SC properties of annealed $Pr_{1.3-x}La_{0.7}Ce_xCuO_4$ [92, 93]. (a) T_c's of $Pr_{1.3-x}La_{0.7}Ce_xCuO_4$ reported in the previous study by Sun *et al.* (closed triangles) [91]. Samples are annealed at 850 °C for 24 hours under Ar gas flow. The long-ranged AF phase and SC one are indicated (Denoted by AF and SC, respectively). A typical phase diagram for a hole-doped cuprate $La_{2-x}Sr_xCuO_4$ is also shown on the left-hand side. (b) The same as (a) for the "protect annealed" samples reported by Adachi *et al.* [90] (open and closed circles) Samples are annealed at 800 °C for 24 hours in vacuum of 10^{-6} Torr with the sample surfaces covered by powders of the same materials with the same compositions. (c) Schematic description of the protect annealing method. (d) Magnetic susceptibility of an annealed PLCCO single crystal which shows a T_c of 27.0 K.

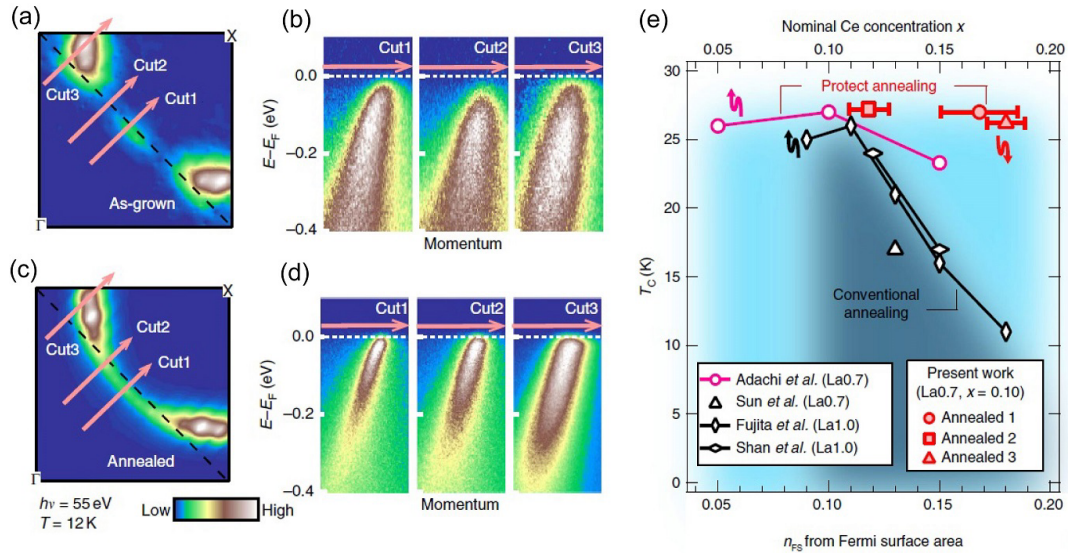

Figure 1.17: ARPES spectra of protect-annealed PLCCO ($x = 0.10$) single crystals [92,93]. (a) Fermi surface mapping for the as-grown sample (b) Band images along the cuts indicated in (a). (c,d) The same plots as (a) and (b) for the sufficiently protect-annealed sample. (e) T_c values of protect annealed PLCCO ($x = 0.10$) plotted against electron concentration n_{FS} estimated from the Fermi surface area. For comparison, the T_c values of conventionally annealed electron-doped cuprates reported in previous studies are also plotted against Ce concentration x.

ity is suppressed, but that fact does not rule out the possibility that appropriately annealed SC parent compound is already oxygen deficient and doped with electrons. The lattice constant is also too indirect for discussion about the carrier concentration. The in-plane lattice constant should be affected not only by the carrier concentration but also by the presence of oxygen defects, and hence one cannot determine the carrier concentration only from the lattice constant. In order to settle this issue, physical quantities which are directly related to the carrier concentration have to be measured.

The role of annealing, which is the key to induce superconductivity, is also highly elusive as described in sections 1.3 and 1.4. Our previous ARPES studies on protect-annealed PLCCO ($x = 0.10$) samples [92, 93] have clearly revealed that efficient annealing strongly suppresses AF correlation and dopes the system with electrons. However, since several effects which may be related with each other are observed at the same time, the precise roles of annealing are still unclear. For the understanding of the mechanism of annealing, more systematic studies are necessary.

1.8 Outline of the thesis

In this thesis, we have first studied the electronic structure of the SC parent compound by ARPES and hard X-ray core-level photoemission spectroscopy in chapters 3 and 4, respectively. Electron concentrations of the SC parent compounds have been determined from observed Fermi surface area and chemical-potential shifts.

We have then studied the effects of annealing in Chapter 5 through systematic ARPES measurements on as-grown and protect-annealed PLCCO single crystals with varying Ce concentrations. Three kinds of annealing effects have been observed: removing Coulomb gap, weakening AF correlation, and doping electrons. In order to remove the influence of the electron doping on the other two effects, we have compared the magnitude of the Coulomb gap and AF gap between as-grown and protect-annealed samples with the same electron concentration (but with different Ce concentrations). We have thus disentangled the roles of annealing. The origin of the observed annealing effects is discussed from the viewpoint of oxygen occupancy.

Chapters 6 and 7 are devoted to the momentum dependence of the AF gap and SC gap of the protect-annealed PLCCO single crystals studied by ARPES, which will advance our understanding of the nature of AF fluctuations and superconductivity in the electron-doped cuprates. Summary and conclusion about the electronic structure of the SC parent compound and the effect of annealing are given in chapter 8.

Chapter 2

Experimental methods and principles

2.1 Photoemission spectroscopy

In this section, the basic principles of photoemission spectroscopy (PES) are summarized.

2.1.1 General formulation

PES is a powerful tool to directly observe the electronic structure of solids. Figure 2.1 illustrates a schematic diagram of PES. Photoemission is a phenomenon that photoelectrons are emitted when photons which have a sufficiently high energy are absorbed by the electrons in solids. From the energy conservation law, kinetic energy in vacuum $E_{\rm kin}^{\rm vac}$ measured from the vacuum level $E_{\rm vac}$ satisfies

$$E_{\rm kin}^{\rm vac} = h\nu - \phi - E_{\rm B}, \tag{2.1}$$

where ϕ is the work function of the solid, and $E_{\rm B}$ is the binding energy relative to the Fermi level ($E_{\rm F}$). Thus, we can know how strongly the electrons are bound in the solid by measuring the kinetic energy of the emitted photoelectrons. In the real experiment, kinetic energy inside the sample measured from $E_{\rm F}$ ($E_{\rm kin}$) rather than $E_{\rm kin}^{\rm vac}$ can be determined. Then, it is convenient to use

$$E_{\rm kin} = h\nu - E_{\rm B}. \tag{2.2}$$

In the one-electron approximation, photoemission process corresponds to the transition of one Bloch electron from the initial state $\phi_{\mathbf{k}j}$ to the final state $\phi_{\mathbf{k}j'}$ above the vacuum level (j and j' are indexes for the states). Assuming that the

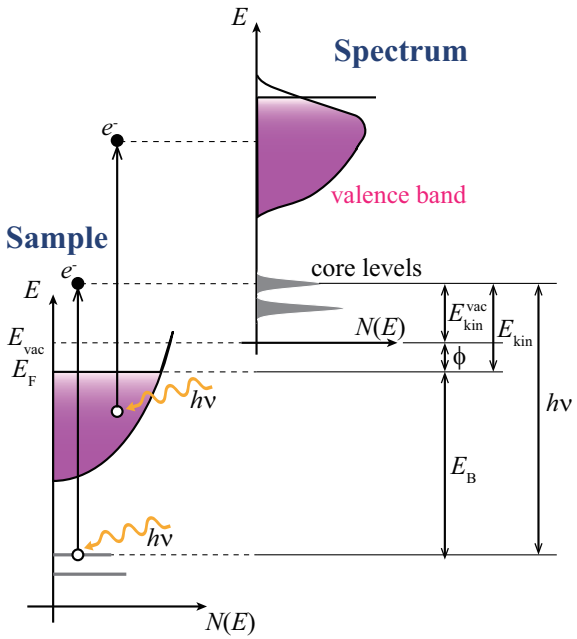

Figure 2.1: Schematic diagram of the principle of PES. The relationship between the energy levels in a solid and the photoemission spectrum.

wave function of other $N-1$ electrons does not change by the sudden removal of one electron, energy conservation gives

$$E_{\mathrm{kin}} = h\nu + \epsilon_{\mathbf{k}}, \tag{2.3}$$

where ϵ_k denotes the energy level of the initial Bloch state. If we apply this approximation, the photoemission spectrum $I(E_{\mathrm{B}})$ can be expressed as

$$I(E_{\mathrm{B}}) \propto \sum_k \delta(E_{\mathrm{B}} + \epsilon_{\mathbf{k}}) \propto N(-E_{\mathrm{B}}). \tag{2.4}$$

Thus, when the one-electron approximation is valid, the photoemission spectrum is proportional to the density of the occupied one-electron states $N(E)$.

2.1.2 Angle-resolved photoemission spectroscopy

Angle-resolved photoemission spectroscopy (ARPES) can probe not only the energies but also the momenta of electrons in solids by using conservation laws, and the band structure is directly determined by combining these informations.

Figure 2.2 schematically shows a diagram of the emission of an electron from a solid to vacuum through the surface. In the photoexcitation by low energy photons,

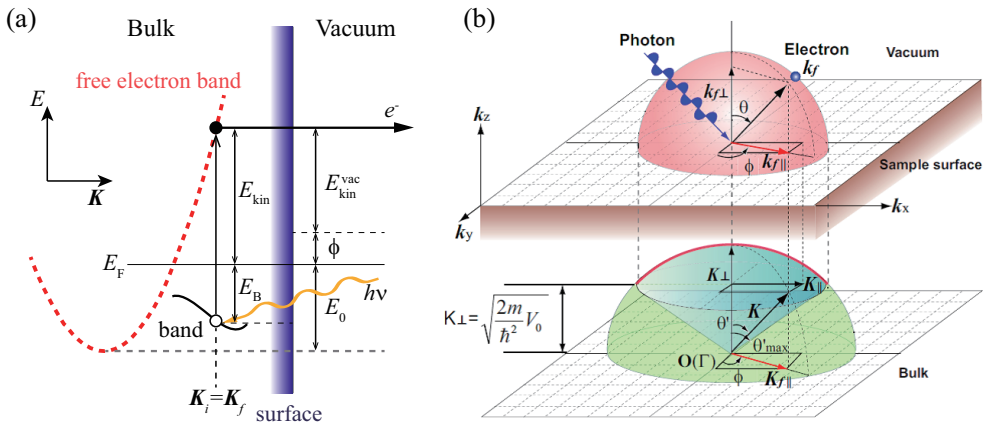

Figure 2.2: Schematic diagram of the principle of ARPES. (a) Energy levels of the electrons after photoexcitation or emission through the surface. (b) Relation of the wave vectors before and after the emission through the sample surface. Upper and lower figures show the situation of outside and inside the sample, respectively.

the momentum of the incident photon $h\nu/c$ is small enough to be neglected, and the wave number of the electron is conserved before and after the photoexcitation except for the reciprocal lattice vector of the initial state ($\boldsymbol{K}_i$) and that of the final one ($\boldsymbol{K}_f$):

$$\boldsymbol{K}_f = \boldsymbol{K}_i + \boldsymbol{G}, \tag{2.5}$$

where $\boldsymbol{G} = (2n_x\pi/a, 2n_y\pi/a, 2n_z\pi/a)$ is a reciprocal lattice vector, and n_x, n_y, and n_z are integer.

Assuming that the final state of the excited electron is a free electron with a mass m_e, energy conservation gives

$$E_{\mathrm{kin}} = \frac{\hbar^2(\boldsymbol{K}_{f\parallel}^2 + \boldsymbol{K}_{f\perp}^2)}{2m_e} - E_0, \tag{2.6}$$

where $\boldsymbol{K}_{f\parallel}$ and $\boldsymbol{K}_{f\perp}$ denote the wave vectors of the final state parallel and perpendicular to the surface, respectively. When the electron is emitted from the sample as shown in Fig. 2.2(b), the wave vector parallel to the surface is conserved. Therefore, by considering Eq. (2.5) the following relationship is satisfied between the wave vector of the emitted electron and that of the initial state parallel to the surface, $\boldsymbol{k}_{f\parallel}$ and $\boldsymbol{K}_{i\parallel}$,

$$\boldsymbol{k}_{f\parallel} = \boldsymbol{K}_{f\parallel} = \boldsymbol{K}_{i\parallel} + \boldsymbol{G}_{\parallel}, \tag{2.7}$$

where $\boldsymbol{G}_{\parallel}$ is the component of the reciprocal lattice vector parallel to the surface. The wave vector of the emitted electron parallel and perpendicular to the surface ($\boldsymbol{k}_{f\parallel}$ and $\boldsymbol{k}_{f\perp}$) can be expressed using polar emission angle θ as

$$\hbar\boldsymbol{k}_{f\parallel} = \sqrt{2m_e E_{\mathrm{kin}}^{\mathrm{vac}}}\sin\theta\boldsymbol{e}_{\parallel} \tag{2.8}$$

$$\hbar\boldsymbol{k}_{f\perp} = \sqrt{2m_e E_{\mathrm{kin}}^{\mathrm{vac}}}\cos\theta\boldsymbol{e}_{\perp}, \tag{2.9}$$

where $\boldsymbol{e}_{\parallel}$ and $\boldsymbol{e}_{\perp}$ are unit vectors.

Summarizing Eqs. (2.1), (2.2), (2.6)-(2.9), we can know both the binding energy E_{B} and the momentum $\boldsymbol{K_i}$ of the hole produced by the photoemission process as

$$\hbar\boldsymbol{K}_{i\parallel} = \sqrt{2m_e(h\nu - \phi - E_{\mathrm{B}})}\sin\theta\boldsymbol{e}_{\parallel} + \boldsymbol{G}_{\parallel} \tag{2.10}$$

$$\hbar\boldsymbol{K}_{i\perp} = \sqrt{2m_e[(h\nu - \phi - E_{\mathrm{B}})\cos^2\theta + V_0]}\boldsymbol{e}_{\perp} + \boldsymbol{G}_{\perp}. \tag{2.11}$$

$V_0 = E_0 + \phi$ is called "inner potential ''and should be assumed in the experiment. If the material under study is a two-dimensional system such as a high-T_c cuprate, E_{B} and $\boldsymbol{K}_{i\parallel}$ give enough information to map the entire band structure. Using polar emission angle ϕ, $\boldsymbol{K}_{i\parallel}$ can be further decomposed to K_{ix} and K_{iy} as

$$\hbar K_{ix} = \sqrt{2m_e(h\nu - \phi - E_{\mathrm{B}})}\sin\theta\cos\phi + \frac{2n'_x\pi}{a} \tag{2.12}$$

$$\hbar K_{iy} = \sqrt{2m_e(h\nu - \phi - E_{\mathrm{B}})}\sin\theta\sin\phi + \frac{2n'_y\pi}{b}, \tag{2.13}$$

where n'_x and n'_y are integers.

2.1.3 Spectral function and self energy

The one-electron approximation described above is no longer valid in a strongly correlated material such as high-T_c superconductors. In this case, one should take many-body effects into account.

In more generalized description, photoemission (inverse photoemission) process is regarded as the removal (addition) of an electron from the ground state $|\Psi_g^N\rangle$ of the N-electron system with the energy E_g^N, leaving the system in an excited state $|\Psi_n^{N-1}\rangle$ ($|\Psi_n^{N+1}\rangle$) of the $(N-1)$-electron ($(N+1)$-electron)system with the energy E_n^{N-1} (E_n^{N+1}). Then, using Fermi's golden rule, the intensity of photoemission and inverse photoemission spectrum, which now corresponds to the single-particle excitation spectrum called a "spectral function ''of the system, is expressed as

$$\begin{aligned} A(\mathbf{k},\epsilon) = &\sum_n \left|\langle\Psi_n^{N-1}|c_{\mathbf{k}}|\Psi_g^N\rangle\right|^2 \delta(\epsilon + E_n^{N-1} - E_g^N) \\ &+ \sum_n \left|\langle\Psi_n^{N+1}|c_{\mathbf{k}}^{\dagger}|\Psi_g^N\rangle\right|^2 \delta(\epsilon + E_n^{N+1} - E_g^N) \end{aligned} \tag{2.14}$$

where $c_{\mathbf{k}}$ and $c_{\mathbf{k}}^{\dagger}$ are the annihilation and creation operators of an electron with the momentum $\mathbf{k}$,respectively, and $\epsilon \equiv E_{\rm kin} - h\nu$. This function can be rewritten using single-particle Green's function. Green's function $G(\mathbf{k}, t)$ is defined as

$$G(\mathbf{k}, t) = -\frac{i}{\hbar}\theta(t)\langle \Psi_g^N | \{c_{\mathbf{k}}(t), c_{\mathbf{k}}^{\dagger}\} | \Psi_g^N \rangle, \tag{2.15}$$

where θ denotes the Heaviside step function, $\{A, B\} \equiv AB + BA$, and $A(t) \equiv e^{iHt/\hbar}Ae^{-iHt/\hbar}$. By Fourier-transforming Eq. (2.15) with respect to t, we obtain Green's function as the function of energy $G(\mathbf{k}, \epsilon)$,

$$\begin{aligned}
G(\mathbf{k}, \epsilon) =& -\frac{i}{\hbar}\int_0^{\infty} dt \langle \Psi_g^N | \{c_{\mathbf{k}}(t), c_{\mathbf{k}}^{\dagger}\} | \Psi_g^N \rangle e^{i(\epsilon + i0^+)t/\hbar} \\
=& -\frac{i}{\hbar}\sum_n |\langle \Psi_n^{N+1} | c_{\mathbf{k}}^{\dagger} | \Psi_g^N \rangle|^2 \int_0^{\infty} dt e^{iE_g^N t/\hbar} e^{-iE_n^{N+1}t/\hbar} e^{i(\epsilon + i0^+)t/\hbar} \\
& -\frac{i}{\hbar}\sum_n |\langle \Psi_n^{N-1} | c_{\mathbf{k}} | \Psi_g^N \rangle|^2 \int_0^{\infty} dt e^{iE_n^{N-1}t/\hbar} e^{-iE_g^N t/\hbar} e^{i(\epsilon + i0^+)t/\hbar} \\
=& \sum_n \frac{|\langle \Psi_n^{N+1} | c_{\mathbf{k}}^{\dagger} | \Psi_g^N \rangle|^2}{\epsilon + i0^+ - E_n^{N+1} + E_g^N} + \sum_n \frac{|\langle \Psi_n^{N-1} | c_{\mathbf{k}} | \Psi_g^N \rangle|^2}{\epsilon + i0^+ + E_n^{N-1} - E_g^N} \qquad (2.16) \\
=& \sum_n |\langle \Psi_n^{N+1} | c_{\mathbf{k}}^{\dagger} | \Psi_g^N \rangle|^2 \left\{ \frac{P}{\epsilon - E_n^{N+1} + E_g^N} - i\pi\delta(\epsilon - E_n^{N+1} + E_g^N) \right\} \\
& + \sum_n |\langle \Psi_n^{N-1} | c_{\mathbf{k}} | \Psi_g^N \rangle|^2 \left\{ \frac{P}{\epsilon + E_n^{N-1} - E_g^N} - i\pi\delta(\epsilon + E_n^{N-1} - E_g^N) \right\}, \qquad (2.17)
\end{aligned}$$

where P denotes the principal value of the integral. Here, the relation $1/(x \mp i0^+) = P(1/x) \pm i\pi\delta(x)$ has been used. Then, the imaginary part of $G(\mathbf{k}, \epsilon)$ gives the above mentioned spectral function $A(\mathbf{k}, \epsilon)$ as

$$\begin{aligned}
-\frac{1}{\pi}{\rm Im}G(\mathbf{k}, \epsilon) =& \sum_n |\langle \Psi_n^{N+1} | c_{\mathbf{k}}^{\dagger} | \Psi_g^N \rangle|^2 \delta(\epsilon - E_n^{N+1} + E_g^N) \\
& + \sum_n |\langle \Psi_n^{N-1} | c_{\mathbf{k}} | \Psi_g^N \rangle|^2 \delta(\epsilon + E_n^{N-1} - E_g^N) \\
=& A(\mathbf{k}, \epsilon). \qquad (2.18)
\end{aligned}$$

In the one-electron approximation, defining the energy of one Bloch state $\phi_{\mathbf{k}j}$ as $\epsilon_{\mathbf{k}}$,

$$E_n^{N+1} - E_g^N = \epsilon_{\mathbf{k}} (\text{if } \phi_{\mathbf{k}j} \text{ is unoccupied}) \tag{2.19}$$

$$E_n^{N-1} - E_g^N = -\epsilon_{\mathbf{k}} (\text{if } \phi_{\mathbf{k}j} \text{ is occupied}). \tag{2.20}$$

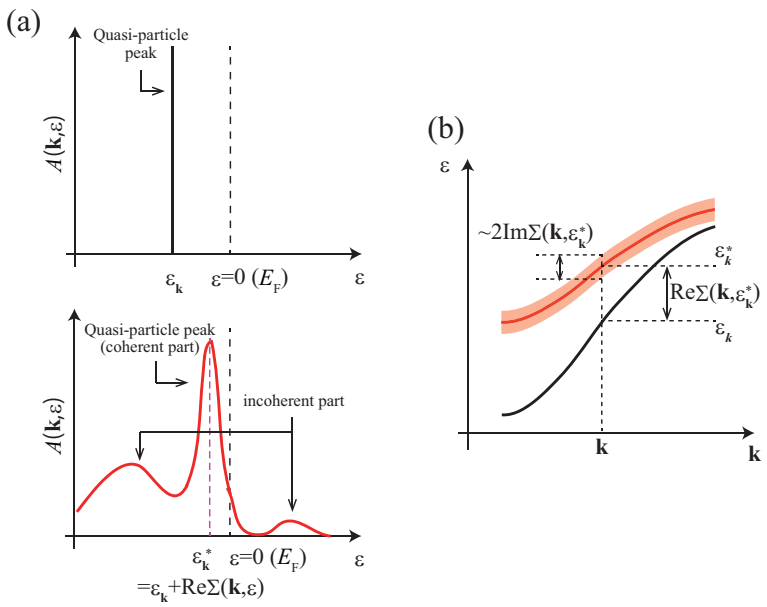

Figure 2.3: Schematic diagram of the photosmission spectral function $A(\mathbf{k}, \epsilon)$. (a) Spectral function $A(\mathbf{k}, \epsilon)$ at a given $\mathbf{k}$ when the one-electron approximation is valid (top) and when the many body effect is taken into account (bottom). (b) Deviation of the band dispersion affected by the electron-electron interaction from the bare band.

By substituting Eqs. (2.19) and (2.20) for Eq. (2.16), the Green's function in the one-electron approximation can be written as

$$G(\mathbf{k}, \epsilon) = \frac{1}{\epsilon - \epsilon_{\mathbf{k}} + i0^{+}}, \tag{2.21}$$

and the following equation is obtained.

$$A(\mathbf{k}, \epsilon) = \delta(\epsilon - \epsilon_{\mathbf{k}}). \tag{2.22}$$

This is nothing else but the relation obtained in Eq. (2.4). The resulting spectral function at a fixed momentum and obtained band dispersion are displayed in Fig. 2.3(a) and (b), respectively.

In the many body system, the self energy $\Sigma(\mathbf{k}, \epsilon)$, which includes a renormalization from all the interactions between electrons, is introduced to the single-particle Green's function as

$$G(\mathbf{k}, \epsilon) \equiv \frac{1}{\epsilon - \epsilon_{\mathbf{k}} - \Sigma(\mathbf{k}, \epsilon)}. \tag{2.23}$$

This equation is called Dyson's equation. In this case, the spectral function is written as

$$\begin{aligned} A(\mathbf{k},\epsilon) &\equiv -\frac{1}{\pi}\mathrm{Im}G(\mathbf{k},\epsilon) \\ &= -\frac{1}{\pi}\frac{\mathrm{Im}\Sigma(\mathbf{k},\epsilon)}{(\epsilon-\epsilon_{\mathbf{k}}-\mathrm{Re}\Sigma(\mathbf{k},\epsilon))^2+(\mathrm{Im}\Sigma(\mathbf{k},\epsilon))^2}. \end{aligned} \tag{2.24}$$

Then, the solution of the equation

$$\epsilon = \epsilon_{\mathbf{k}} + \mathrm{Re}\Sigma(\mathbf{k},\epsilon), \tag{2.25}$$

$\epsilon = \epsilon^*_{\mathbf{k}}$, gives a peak of $A(\mathbf{k},\epsilon)$, and momentum dispersion of this peak gives a band dispersion. $\mathrm{Re}\Sigma(\mathbf{k},\epsilon)$ shifts the energy at a momentum $\mathbf{k}$ and $\mathrm{Im}\Sigma(\mathbf{k},\epsilon)$ broaden the spectral width as shown in Fig. 2.3(b).

From a Taylor expansion of the $\mathrm{Re}\Sigma(\mathbf{k},\epsilon)$ around $\epsilon = \epsilon^*_{\mathbf{k}}$ substituting it for Eq. (2.24),

$$A(\mathbf{k},\epsilon) \simeq -\frac{Z_{\mathbf{k}}(\epsilon^*_{\mathbf{k}})}{\pi}\frac{Z_{\mathbf{k}}(\epsilon^*_{\mathbf{k}})\mathrm{Im}\Sigma(\mathbf{k},\epsilon)}{(\epsilon-\epsilon^*_{\mathbf{k}})^2+(Z_{\mathbf{k}}(\epsilon^*_{\mathbf{k}})\mathrm{Im}\Sigma(\mathbf{k},\epsilon))^2}, \tag{2.26}$$

where

$$Z_{\mathbf{k}}(\mathbf{k},\epsilon^*) \equiv \left(1-\frac{\partial \mathrm{Re}\Sigma(\mathbf{k},\epsilon)}{\partial\epsilon}\bigg|_{\epsilon=\epsilon^*_{\mathbf{k}}}\right)^{-1} < 1. \tag{2.27}$$

$Z_{\mathbf{k}}(\epsilon^*_{\mathbf{k}}) < 1$ is called a renormalization factor. As shown in Fig. 2.3(a), the peak position of the quasi-particle, which is called *coherence part*, is located at $\epsilon = \epsilon^*_{\mathbf{k}}$ with a spectral weight of $Z_{\mathbf{k}}(\epsilon^*_{\mathbf{k}})$ and a full width at half maximum (FWHM) of $-2z_{\mathbf{k}}(\epsilon^*_{\mathbf{k}})\mathrm{Im}\Sigma(\mathbf{k},\epsilon^*_{\mathbf{k}})$. The remaining spectral weight is distributed in the *incoherent part* away from E_{F}.

In the vicinity of E_{F}, $\epsilon^*_{\mathbf{k}}$ can be written as $\epsilon^*_{\mathbf{k}} = v^*_{\mathbf{k}}(k-k_{\mathrm{F}})$, where $v^*_{\mathbf{k}}(\equiv|\nabla\epsilon^*_{\mathbf{k}}|)$ is the renormalized Fermi velocity and $\mathbf{k}$ is taken perpendicular to the Fermi surface. Then the momentum distribution curve (MDC) is given by

$$A(\mathbf{k},\epsilon) = -\frac{Z_{\mathbf{k}}/v^*_{\mathbf{k}}}{\pi}\frac{Z_{\mathbf{k}}\mathrm{Im}\Sigma(\mathbf{k},\epsilon)/v^*_{\mathbf{k}}}{(k-(k_{\mathrm{F}}+\epsilon/v^*_{\mathbf{k}}))^2+(Z_{\mathbf{k}}\mathrm{Im}\Sigma(\mathbf{k},\epsilon)/v^*_{\mathbf{k}})^2}. \tag{2.28}$$

Thus, the MDC is given by a Lorentzian with FWHM of $\Delta k(\epsilon) = 2|Z_{\mathbf{k}}\mathrm{Im}\Sigma(\mathbf{k},\epsilon)/v^*_{\mathbf{k}}|$, if the k-dependence of $Z_{\mathbf{k}}$, $\mathrm{Im}\Sigma(\mathbf{k},\epsilon)$ and $v^*_{\mathbf{k}}$ along the cut can be neglected.

Since the Green's function is a linear response function, the real and imaginary part of it follows a Kramers-Kronig relation. Therefore, $\mathrm{Re}\Sigma(\mathbf{k},\epsilon)$ and $\mathrm{Im}\Sigma(\mathbf{k},\epsilon)$

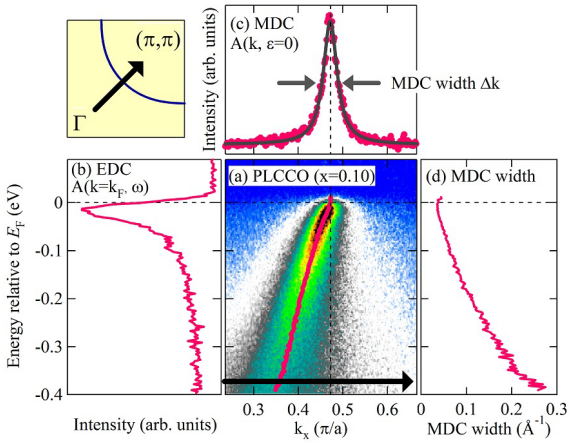

Figure 2.4: Data taken with the angular mode of a Scienta analyzer for $Pr_{1.3-x}La_{0.7}Ce_xCuO_4$. (a) Intensity plot in the energy-momentum space at the nodal direction. (b) EDC at $k = k_F$. (c) MDC at $E = E_F$. (d) Energy dependence of the MDC width derived from fitting the MDCs to a Lorentzian.

also follows a Kramers-Kronig relation as

$$\mathrm{Re}\Sigma(\mathbf{k},\epsilon) = \frac{1}{\pi} P \int_{-\infty}^{\infty} \frac{\mathrm{Im}\Sigma(\mathbf{k},\omega)}{\epsilon-\omega} d\omega \tag{2.29}$$

$$\mathrm{Im}\Sigma(\mathbf{k},\epsilon) = -\frac{1}{\pi} P \int_{-\infty}^{\infty} \frac{\mathrm{Re}\Sigma(\mathbf{k},\omega)}{\epsilon-\omega} d\omega. \tag{2.30}$$

This relation must be satisfied regardless of the nature of the system, hence is useful to estimate the self energy of the target system.

Figure 2.4 summarizes a relationship between the obtained ARPES spectra, momentum distribution curve (MDC), and energy distribution curve (EDC).

2.1.4 Electron escape depth

Photoemission spectroscopy is a surface sensitive technique. The escape depth of photoelectrons are determined by electron-electron and electron-phonon interactions. Generally, electron-phonon scattering plays a role only at low energies below the phonon frequencies. The escape depth of the electrons λ is then determined by electron-electron interaction. The cross-section for electron-electron scattering σ is given by

$$\frac{d^2\sigma}{d\Omega d\varepsilon} = \frac{\hbar^2}{\pi e a_0} \frac{1}{q^2} \mathrm{Im} - \frac{1}{\epsilon(\boldsymbol{q},\varepsilon)}\ , \tag{2.31}$$

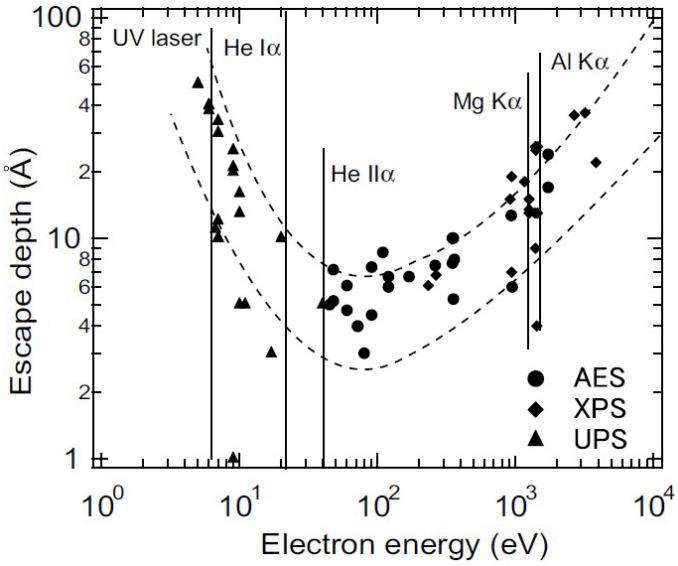

Figure 2.5: The escape depth of electrons in solids. Dashed curves indicate the approximate range for the experimental data [94]. Photoemission using VUV light is highly surface sensitive with the escape depth of $\sim$ 10 Å, and while hard X-ray photoemission is relatively bulk sensitive with the escape depth of $\sim$ 100 Å. Reprinted from ref. [95]

where $\epsilon(\boldsymbol{q}, \varepsilon)$ is the dielectric function, $\hbar q$ is the momentum transfer and ε is energy transfer in the scattering process. $a_0 = 0.529$ Å, and Ω is the solid angle into which the electrons are scattered. Although $\epsilon(\boldsymbol{q}, \varepsilon)$ is material dependent, the escape depth as a function of energy roughly follows the universal curve as shown in Fig. 2.5 [94,95]. Then, except for small energies (< 10 eV), the electrons in solids can be approximately described by free-electron gas. In that case, the plasma frequency, which is a function of only the electron density or the mean electron-electron distance r_s determines the loss function Imϵ. The inverse escape depth λ^{-1} is thus described by r_s, which is roughly equal for all materials, and one obtains

$$\lambda^{-1} \cong \sqrt{3}\frac{a_0 R}{E_{\text{kin}}} r_s^{-3/2} \ln\left(\frac{4}{9\pi}\right)^{3/2} \frac{E_{\text{kin}}}{R} r_s \,, \tag{2.32}$$

where $R = 13.6$ eV, and r_s is measured in units of a_0. Therefore, electron-escape depth λ is given as a function of kinetic energy of electron E_{kin} as observed experimentally in Fig. 2.5, and almost all materials show a similar dependence of the mean electron escape depth.

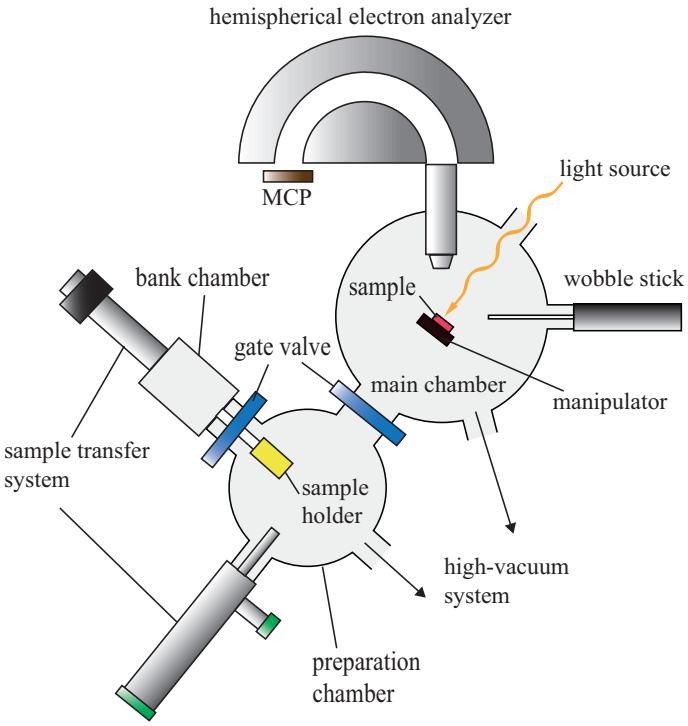

Figure 2.6: Schematic description of the photoemission measurement system.

2.2 Experimental setup

2.2.1 Photosmission measurement system

Figure 2.6 shows a schematic description of the photoemission measurement system. The sample is introduced in the bank chamber and transferred to the main chamber via the preparation chamber. Under the ultra-high vacuum in the main chamber, the sample is cleaved for the clean surface not degraded by gas molecules. Electrons are emitted by the excitation of the incident photons, entering the electron lens, and are focused by electrostatic fields. The photoelectrons are deaccelerated by a retarding potential V_{R} before entering a hemispherical electron analyzer. The analyzer transmits only photoelectrons with a given energy (pass energy E_{P}). The relationship between the retarding potential V_{R} and the pass energy E_{P} is given by

$$E_{\mathrm{P}} = E_{\mathrm{kin}} - eV_{\mathrm{R}} - \phi_{\mathrm{A}} \tag{2.33}$$

$$= \frac{eV_{\mathrm{P}}}{R_2/R_1 - R_1/R_2}, \tag{2.34}$$

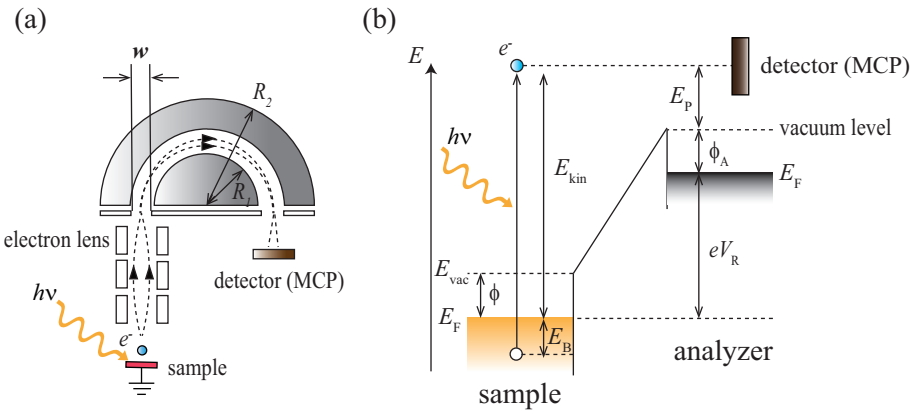

Figure 2.7: Schematic diagram inside of the analyzer, and energy levels of the sample and analyzer. (a) The loci of the emitted photoelectrons through the hemispherical electron analyzer. (b) The diagram showing potential and energy levels for the sample and analyzer.

where ϕ_{A} is the work function of the analyzer as shown in Fig. 2.7(b), and V_{P} is the applied voltage between the inner and outer spheres of the hemispherical analyzer. Electrons are multiplied by a micro-channel plate (MCP) and finally detected by a CCD camera as light spots on the fluorescent screen. This multi-channel detection system using MCP has a high detection efficiency because each channel can multiply the electrons which have different momenta and energies at the same time.

The energy resolution ΔE is determined by the slit width w and the radii of the inner and outer hemispheres, R_1 and R_2:

$$\Delta E = \frac{w E_{\mathrm{P}}}{R_1 + R_2}. \tag{2.35}$$

In order to sweep E_{kin}, either E_{P} or V_{R} has to be swept considering Eq. (2.33). In a real experiment, however, E_{P} is usually kept as a constant and V_{R} is swept so that ΔE is kept constant regardless of E_{kin}.

2.2.2 MBE growth system

Figure 2.8 schematically shows MBE growth system in NTT Basic Research Laboratories. The MBE growth is carried out by electron beam co-evaporation from metal sources in a custom designed UHV chamber. As an oxidizing agent, either O_3 gas with ~ 10 % concentration or O^* generated from RF-activated source is used. To monitor the evaporation rate element specifically, electron impact emission spectroscopy (EIES) is employed. Inside the EIES sensor, thermal electrons

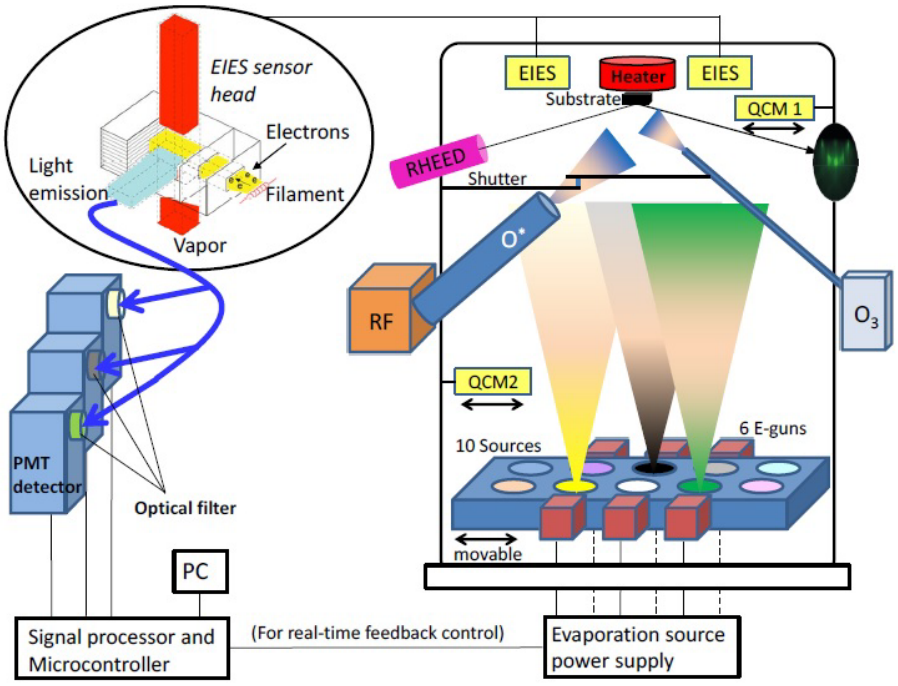

Figure 2.8: Schematic illustration of the multi-source oxide MBE setup in NTT Basic Research Laboratories [96]. EIES: Electron Impact Emission Spectroscopy sensor, PMT: PhotoMultiplier Tube, RHEED: Reflection High-Energy Electron Diffraction, QCM; Quartz Crystal Microbalance.

from the filament hit the evaporated metal and excite it. The light emitted in the course of relaxation is guided to the photomultiplier tube (PMT) through an optical filter. Since the wave length of emitted light depends on the element, one can obtain element-specific information about the evaporation by using the proper filter. The detected signal is converted to the electrical one, and utilized for the stable evaporation of the metal.

Chapter 3

Film growth and angle-resolved photoemission spectroscopy of the superconducting parent compound Pr_2CuO_4

Part of this chapter has been published in "As-grown superconducting Pr_2CuO_4 under thermodynamic constraints", Y. Krockenberger, M. Horio, H. Irie, A. Fujimori, and H. Yamamoto, Appl. Phys. Express **8**, 053101 (2015).

3.1 Introduction

After 30 years since the discovery of high-temperature superconductivity in cuprates, it is now well established that the superconductivity emerges by doping holes into antiferromagnetic (AF) insulating parent compounds. On the other hand, superconductivity emerging by doping electrons is far less investigated. Ln_2CuO_4 (Ln: rare earth) with the T' structure, where Cu takes a square-planar coordination, is the parent material of the electron-doped cuprate superconductors and widely considered to be an AF Mott insulator. Generally, electron doping by substituting Ce^{4+} for Ln^{3+} alone cannot induce superconductivity to the T'-type cuprates, but an additional procedure of post-growth annealing in a reducing atmosphere is required [1]. In early neutron-scattering studies, it has been concluded that oxygen atoms which occupy the apical sites diffuse out of the sample by annealing [24,25], but in a more recent Raman-scattering study, it has been suggested that the removal takes place from the regular (CuO_2- and/or LnO layer-) oxygen sites [28]. Although the microscopic effect of annealing thus remain elusive, as-grown samples typically have excess oxygen [97] and a small fraction of the

oxygen atoms are removed by annealing. Iodometric titration and thermogravimetric analyses have revealed that the amount of the removed oxygen depends on Ce concentrations [22, 23]: 0.07 out of 4 oxygen atoms is removed from the parent compound Nd_2CuO_4, while only 0.01 oxygen is removed from the optimally doped $Nd_{2-x}Ce_xCuO_4$. That small amount of reduction, however, dramatically suppresses the AF order (reduce the AF correlation length and/or the local magnetic moment) [28] and reduces quasi-particle scattering [26], inducing superconductivity to the Ce-doped sample.

Recently, it has been demonstrated that thin-film samples of T'-type cuprates can exhibit superconductivity without any Ce doping by properly annealing them [19,71,73,77–86]. Surprisingly, a superconducting (SC) transition temperature (T_c) of the SC parent compound is typically 1-3 K higher than those of the conventional optimally Ce-doped superconductors with doping level of ~ 0.15. The observation has brought about much controversy, casting doubt on the general assumption that the parent compound of the cuprate superconductor is an AF Mott insulator. In a depth-resolved μSR study, it has been observed that fast relaxation due to AF spin ordering is suppressed inside the bulk of the SC Pr_2CuO_4 thin films [98], suggesting that the superconductivity indeed occurs in the bulk. The fact that the parent compound can be SC, however, does not straightforwardly mean that the T'-type cuprates can be SC at half-filling, since oxygen reduction by annealing could affect the carrier concentration. In fact, changes in the Néel temperature [31] and the optical conductivity [99] for bulk $Nd_{2-x}Ce_xCuO_4$ crystals caused by annealing have been found to be similar to that by 0.03-0.05 Ce doping, although those physical properties are not directly related to electron concentrations. Furthermore, our recent angle-resolved photoemission spectroscopy (ARPES) studies as well as an ARPES study by Wei *et al.* have directly revealed additional electron doping with annealing by estimating carrier concentration from observed Fermi surface area [93,100]. In order to answer the critical question of whether T'-type cuprates can be SC at half-filling or not, experimental probes sensitive to the carrier concentration need to be applied to the SC parent compounds.

In the present chapter, we report ARPES measurements on the SC parent compound Pr_2CuO_4 and directly estimate carrier concentration. Since surface sensitive measurements using vacuum ultraviolet (VUV) light are necessary for high-resolution ARPES, sample surfaces have to be kept clean without exposure to air. However, for the reduction annealing, which has been mandatory to induce superconductivity in the parent compounds, one has to take the sample out fof the ultra-high-vacuum (UHV) growth chamber, and then the sample surface is immediately contaminated. To solve this problem, we synthesized SC parent compounds Pr_2CuO_4 without *ex-situ* annealing.

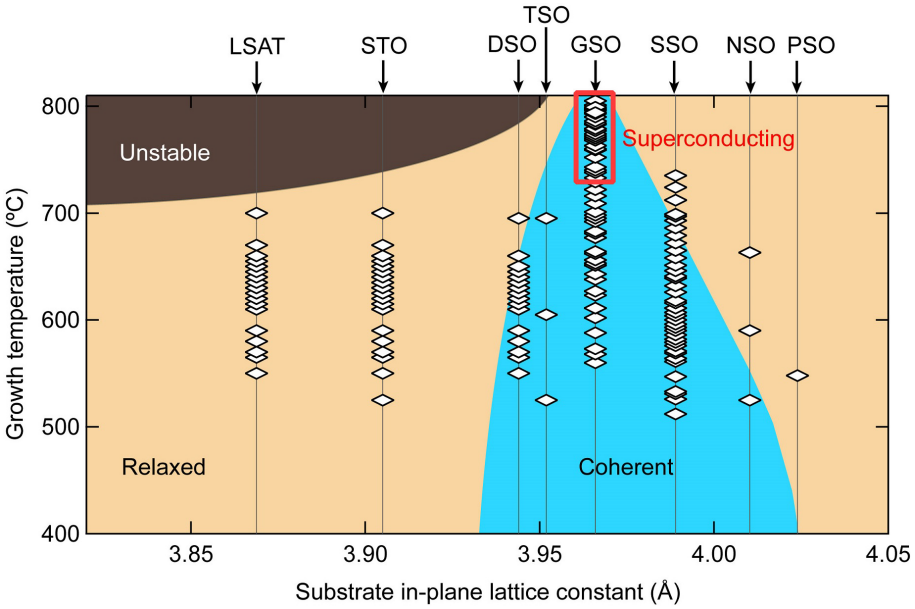

Figure 3.1: Growth temperature-substrate lattice constant phase diagram of Pr_2CuO_4 thin films synthesized on (001) $SrTiO_3$ (STO), (110) $GdScO_3$ (GSO), and (110) $SmScO_3$ (SSO). The same quantities on (001) $(LaAlO_3)_{0.3}(Sr_2AlTaO_6)_{0.7}$ (LSAT), (110) $DyScO_3$ (DSO), (110) $TbScO_3$ (TSO), (110) $NdScO_3$ (NSO), and (110) $PrScO_3$ (PSO) were taken from ref. [101] and plotted together. The partial oxygen pressure during the growth was 1×10^{-7} Torr.

3.2 Growth of as-grown superconducting Pr_2CuO_4 thin films

Photoemission spectroscopy using incident photons in the energy range of soft X rays can probe deep inside the crystal and, therefore, difficult surface treatment is not mandatory, but the photoionization cross-section for the $3d$ orbital is small and both momentum and energy resolutions are not sufficiently good. High resolution photoemission with VUV light, which is unfortunately highly surface sensitive, is, therefore, required for the present purpose. Due to high surface sensitivity of the technique, one must prepare clean sample surfaces without exposing the sample to the air. Most of the SC parent compounds of the electron-doped cuprates reported so far needed annealing in a small furnace under precisely controlled pressure and temperature conditions after taken out of the UHV growth chamber [86], upon which the surface was immediately degraded. For ARPES measurements, therefore, it is mandatory to synthesize SC parent compound inside the UHV growth chamber without *ex-situ* annealing. Recently, it has been reported that La_2CuO_4

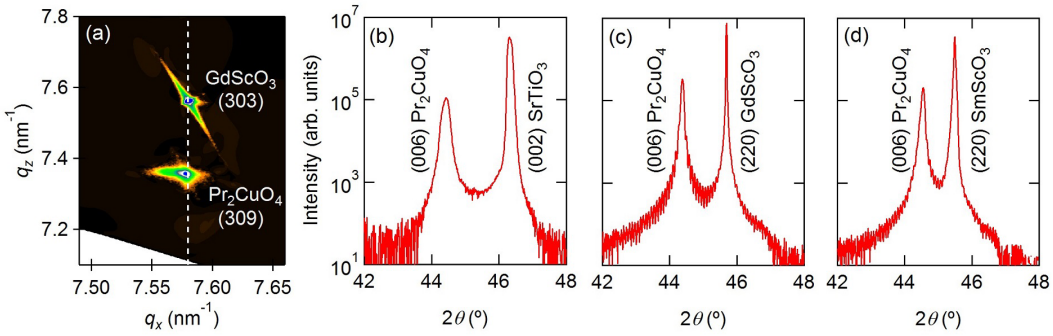

Figure 3.2: X-ray diffraction of Pr_2CuO_4 thin films. (a) Reciprocal space mapping of Pr_2CuO_4 coherently grown on $GdScO_3$ (110). (b)-(d) X-ray diffraction pattern taken around the (006) peak of Pr_2CuO_4 grown on $SrTiO_3$ (001), $GdScO_3$ (110), and $SmScO_3$ (110), respectively.

with the T' structure can be made SC without *ex-situ* annealing [86]. However, the T'-type La_2CuO_4 undergoes a gradual relaxation from the T' to the T structure just after the growth and hence is not suitable for ARPES measurements, which typically take 10-20 hours. Considering that T'-type cuprates with larger lanthanides are empirically easier to be made SC [84], we synthesized Pr_2CuO_4 under various growth conditions, aiming at making the sample SC without *ex-situ* annealing.

Thin films of Pr_2CuO_4 with 100 nm thickness were grown using the molecular beam epitaxy method in a custom designed UHV chamber at NTT Basic Research Laboratories. O_2 in mixture with O_3 was continuously flown into the UHV growth chamber during the growth as an oxidizing agent. Typically, Pr_2CuO_4 thin films are grown at 650-750 °C under the oxygen (O_2 + O_3) pressure of 5×10^{-6} Torr, but contain considerable amount of excess oxygen and are insulating. For the induction of superconductivity, growth conditions at higher temperature and lower oxygen pressure were explored to avoid excess oxygen. Since this exploration brought the growth condition closer to the thermodynamic phase instability, thereby making easier the decomposition of Pr_2CuO_4 into Pr_2O_3, CuO_2, and/or CuO, we used substrates whose in-plane lattice constants were close to that of the bulk Pr_2CuO_4 crystal ($a \sim 3.9588$ Å), specifically, $GdScO_3$ (110) with $a^* = 3.963$ Å and $SmScO_3$ (110) with $a^* = 3.990$ Å where a^* represents a pseudocubic in-plane lattice constant, in addition to the most frequently used $SrTiO_3$ (001) with $a = 3.905$ Å. In general, reducing lattice mismatch enables coherent growth of thin films retaining the lattice constant of the substrate and help the stabilization of desired phases.

Figure 3.1 shows the growth phase diagram of Pr_2CuO_4 thin film plotted against the in-plane lattice constant of the substrate and the growth temperature, and high-

lights the critical role of the substrate for the growth of Pr_2CuO_4 thin films. When synthesized at a low oxygen pressure 1×10^{-7} Torr on a $SrTiO_3$ (001) substrate, a large lattice mismatch made the thin film relaxed and eventually decomposed it at high temperatures above $\sim$ 700 °C. On $SmScO_3$ (110), Pr_2CuO_4 was grown coherently at low temperatures, but it was relaxed above $\sim$ 700 °C. On the other hand, on $GdScO_3O$ (110), whose in-plane lattice constant is the closest to the value of the bulk crystal, Pr_2CuO_4 was grown up to $\sim$ 800 °C without losing coherency. The coherent growth on GSO (110) is evidenced by the reciprocal space mapping shown in Fig. 3.2(a). The diffraction spots from the sample and from the substrate have exactly the same wave number in the x direction, indicating that the in-plane lattice constant is identical. The coherently grown Pr_2CuO_4 film on $GdScO_3$ (110) also exhibits Laue fringes, which are absent in the relaxed film on $SrTiO_3$ (001), and sharper diffraction peaks, indicating a higher degree of crystalline perfection. Coherency thus enables the growth of high-quality thin films under a thermodynamically unstable condition, which is not accessible when the lattice is relaxed.

We have grown more than one hundred Pr_2CuO_4 thin films on $GdScO_3$ (110) and found that with increasing temperature and decreasing oxygen pressure, the c-axis lattice constant of the Pr_2CuO_4 thin film was reduced, suggesting the diffusion of oxygen atoms out of the sample. The lattice contraction along the c-axis was accompanied by the reduction of the resistivity by more than one order of magnitude as shown in Fig. 3.3(a), demonstrating the critical role played by the oxygen content. Eventually, superconductivity was realized in samples with the c-axis parameter shorter than 12.200 Å grown under the condition indicated in Fig. 3.1. In Fig. 3.3(b), the resistivity of a typical as-grown SC Pr_2CuO_4 film is plotted. T_c was 25.0 K and the residual resistivity ratio (RRR) ($= \rho_{30K}/\rho_{300K}$) was 6.1, indicating that the SC state is similar to that in the *ex-situ* annealed Pr_2CuO_4 [19]. Thus, we successfully obtained SC as-grown Pr_2CuO_4 by coherent growth under a reducing condition, instead of annealing it *ex-situ* under a reducing condition after the growth.

3.3 Angle-resolved photoemission spectroscopy of Pr_2CuO_4 thin films

ARPES experiments were carried out at beamline 2A of Photon Factory with circularly polarized $h\nu = 55$ eV photons. The total energy resolution was set at 35 meV. X-ray photoemission measurement was also performed to check the surface condition with linearly polarized $h\nu = 1200$ eV photons. All the measurements were performed under the pressure better than 7×10^{-11} Torr and at 15 K.

Pr_2CuO_4 thin films for ARPES measurement were grown as described in the section 3.2. Two Pr_2CuO_4 samples were measured: one was non-SC with the c-

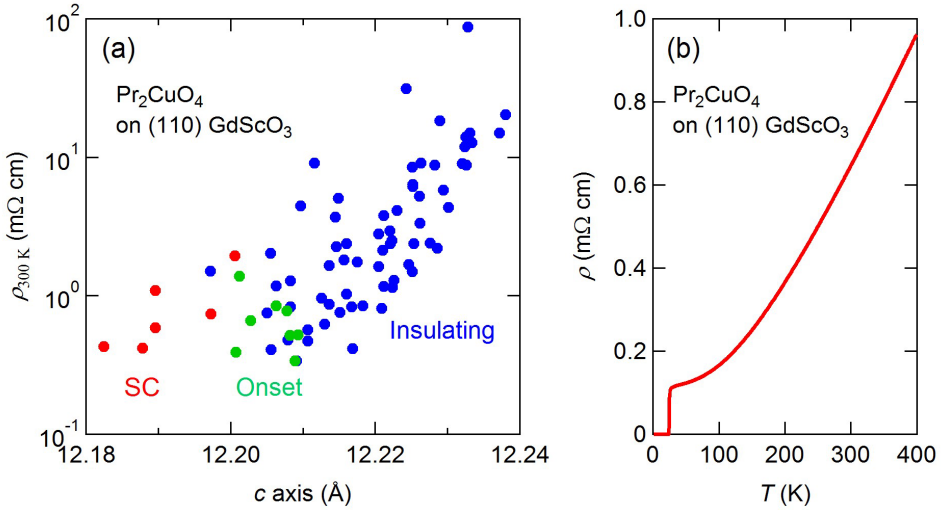

Figure 3.3: Superconductivity in as-grown Pr_2CuO_4 thin films. (a) Resistivity of Pr_2CuO_4 grown on $GdScO_3$ (110) at 300 K (ρ_{300K}) plotted against c-axis length. The samples are classified into three categories: insulating (red circles), metallic with an onset of superconductivity (green circles), and SC (blue circles). (b) Resistivity of a representative SC Pr_2CuO_4 sample grown on $GdScO_3$ (110) at 790 °C and 7×10^{-8} Torr partial oxygen pressure.

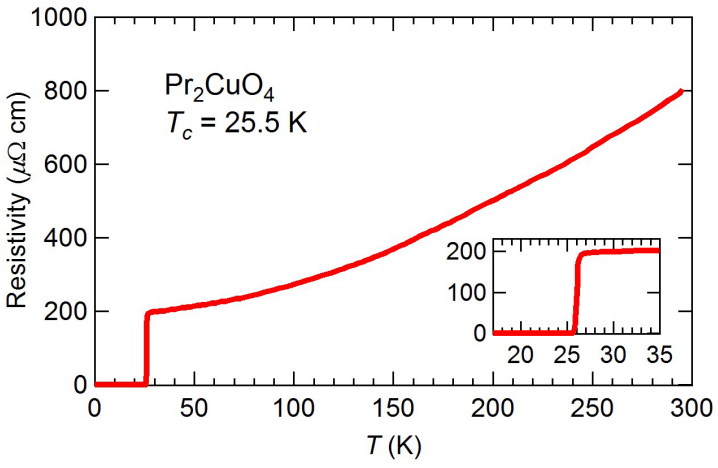

Figure 3.4: Resistivity of the SC Pr_2CuO_4 thin film plotted against temperatures. The inset magnifies the SC transition.

axis length of 12.207 Å and the other was SC with the T_c of 25.5 K, which was confirmed by resistivity measurement after the ARPES measurement as shown in Fig. 3.4, and with the c-axis length of 12.190 ÅḂoth of the samples were grown under the oxygen pressure of 2×10^{-6} Torr, but the growth temperature was set at 780 °C for the SC sample, and 760 °C for the non-SC sample. The distance between a O_3-injection nozzle and the sample, which affected the O_3 concentration at the sample position, was 3 mm and 5 mm for SC and non-SC samples, respectively. In order to keep the surface of as-grown SC Pr_2CuO_4 thin film clean until the ARPES measurement, Se capping was employed. After the growth, the sample was immediately cooled down to 70 °C and amorphous Se was evaporated to the thickness of 50 nm onto the sample under the vacuum of $\sim 1 \times 10^{-9}$ Torr to protect the sample surface before taken out of the growth chamber. Prior to the ARPES measurement, the sample was heated inside the preparation chamber at 150 °C for 30 minutes under the vacuum better than 2×10^{-9} Torr to desorb the Se cap, and then transferred *in-situ* to the measurement chamber. Although this Se-capping method is now widely used for VUV APRES measurements on thin films of the topological insulator Bi_2Se_3 [102] and the iron-based superconductor FeSe [103], it is not trivial if it is also applicable to metal oxides such as Pr_2CuO_4. To examine the surface condition, we first measured core-level photoemission spectra using soft X rays. Figure 3.5(a) shows X-ray photoemission spectra in a wide energy range before and after the decapping procedure. While the spectrum is dominated by Se core-level peaks in the presence of the Se cap, once the sample is heated, core-level peaks of Pr, Cu, and O emerges. The intense Se 3d peaks become unrecognizable after heating [Fig. 3.5(b)], indicating that the desorption of amorphous Se was almost complete. The emergent O 1s core level has a sharp peak and a long tail on the higher binding energy side. The intensity of the shoulder at $\sim$ 531 eV is comparable to that of $Nd_{2-x}Ce_xCuO_4$ single crystals cleaved *in-situ* in a previous soft X-ray photoemission study [104]. Therefore, the Se cap seemingly protected the surface of Pr_2CuO_4 from contamination rather efficiently.

After removing the Se cap, ARPES measurements have been performed using VUV photons. We have measured two Pr_2CuO_4 thin films with different physical properties: One was non-SC and the other was SC with the T_c of 25.5 K as shown in Fig. 3.4. Fermi surfaces and band dispersion were successfully observed for both samples as shown in Fig. 3.6. For the non-SC sample, in moving from the node [Fig. 3.6(b1)] to the hot spot [Fig. 3.6(b2)], where Fermi surface and AF Brillouin-zone boundary cross, the band is gradually gapped. This gap is characteristic of the electron-doped cuprates and called an AF pseudogap. The gap originates from band folding due to AF short range order [45–47, 105]. Approaching the antinode, the upper part of the split band is lowered, crosses E_F, and produces finite spectral intensity just below E_F [Fig. 3.6(b3)]. The resulting Fermi surface shown in Fig. 3.6(a) is discontinuous and unclear other than the antinodal

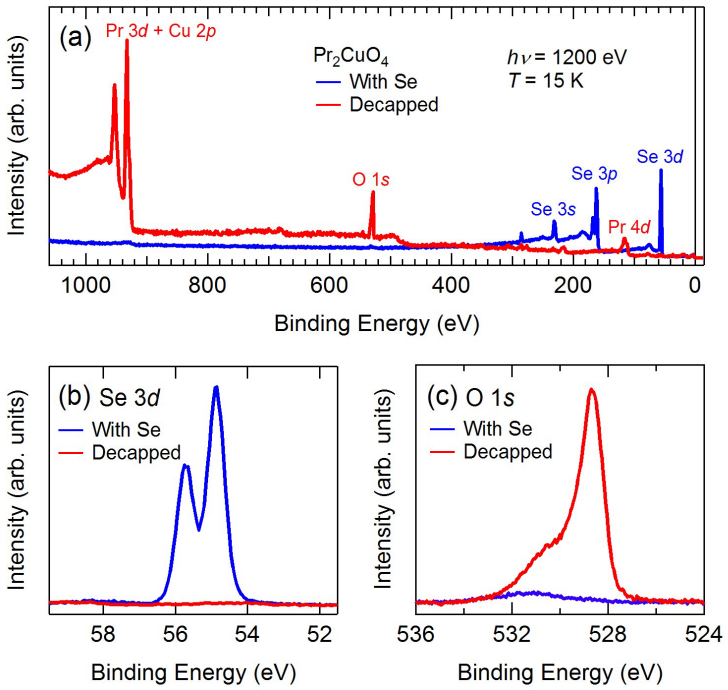

Figure 3.5: X-ray photoemission spectra of Pr_2CuO_4 thin film before and after removing the Se capping layer. (a) Survey spectra in a wide energy range. (b,c) Se 3*d* and O 1*s* spectra, respectively. An integral type background has been subtracted from both spectra.

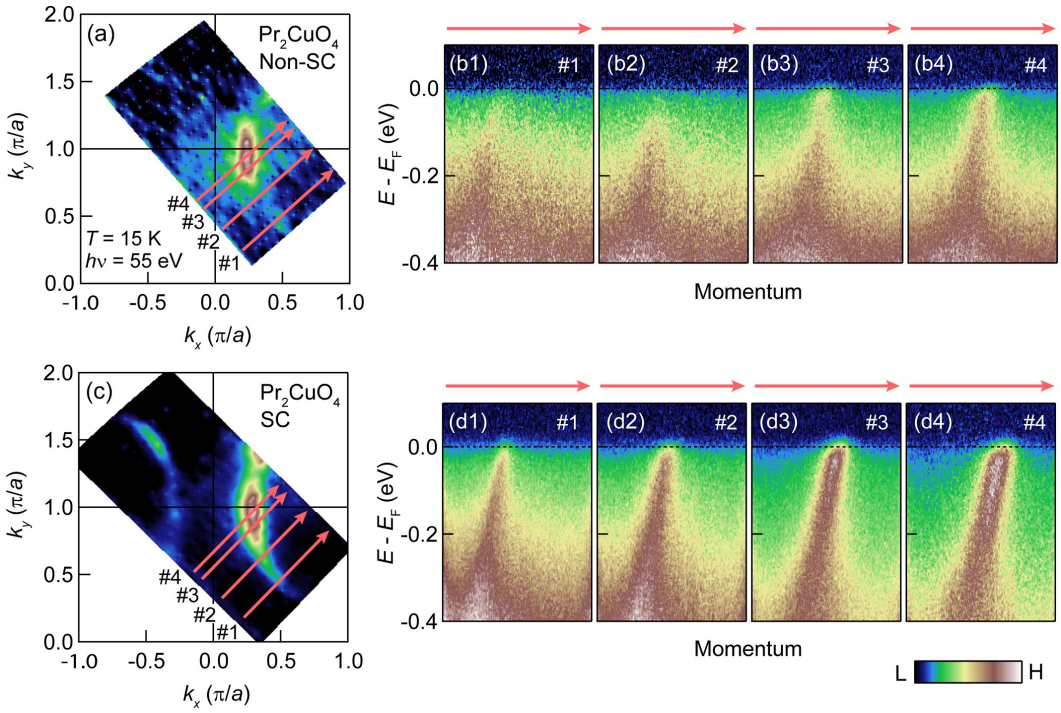

Figure 3.6: ARPES spectra of Pr_2CuO_4 thin films. (a) Fermi surface of non-SC Pr_2CuO_4. (b1-b4) Band images taken along the cuts indicated in (a). (c) Fermi surface of SC Pr_2CuO_4. (d1-d4) Band images taken along the cuts indicated in (c).

segment. On the other hand, for the SC sample, spectral intensity at the hot spot is recovered [Fig. 3.6(d2)] and the Fermi surface becomes continuous [Fig. 3.6(c)], suggesting strong suppression of AF correlation. These changes indicate that the parent compound of the electron-doped cuprates is in the competing state between antiferromagnetism and superconductivity, and the balance can be modified by the oxygen content.

For more detailed information about the electronic structure of SC Pr_2CuO_4, energy distribution curves (EDCs) were extracted from several k_F points from the nodal to antinodal regions [Fig. 3.7(a)]. Spectral intensity is rather weak around the node, and the peak intensity develops on approaching the antinode. However, if an EDC taken from the momentum region near (π, π) is subtracted as the momentum-independent extrinsic background [45] and normalized to the peak height, a sharp quasi-particle peak becomes visible on the entire Fermi surface of the SC film [Fig. 3.7(b)]. There is no gap anywhere on the Fermi surface, but two-peak structure, which is indicative of AF band splitting, is observed for EDCs near the hot spot. The peak intensity was also found to vary along the Fermi

surface by normalizing the EDCs to the intensity at high binding energies (-0.4 eV $\leq E - E_F \leq -0.25$ eV) after the background subtraction, thereby excluding the effect of the momentum-dependent matrix element, as shown in Fig. 3.7(c). The intensity integrated within $E - E_F = \pm 20$ meV is plotted in Fig. 3.7(d) against the Fermi surface angle ϕ defined in the inset. Upon moving away from the node ($\phi = 45°$), the spectral intensity decreases, and takes a minimum at the hot spot, but on approaching the antinode ($\phi = 0°$), the intensity is recovered to the level close to that of the nodal region. The clear suppression of the intensity at E_F around the hot spot can be attributed to the increase of quasi-particle scattering between two hot spots by AF correlation with a propagation vector of (π, π) [45].

The present analysis has thus revealed that the (π, π) AF fluctuations persist in the SC Pr_2CuO_4. It is important to compare the observed AF signature to that of conventional Ce-doped superconductors. Since $Nd_{2-x}Ce_xCuO_4$ has been most systematically studied by ARPES [45, 48, 69] and the traditional phase diagrams for $Nd_{2-x}Ce_xCuO_4$ and $Pr_{2-x}Ce_xCuO_4$ are not very different [5, 106], we made comparisons with $Nd_{2-x}Ce_xCuO_4$. The magnitude of the AF band splitting Δ estimated from the position of the peak at the highest energy was 100 meV for SC Pr_2CuO_4, which is comparable to those observed in optimally to overdoped $Nd_{2-x}Ce_xCuO_4$ (x = 0.15-0.17) [45, 48]. As for the spectral intensity, the lowest energy peak was always the largest in SC Pr_2CuO_4, while in optimally doped $Nd_{2-x}Ce_xCuO_4$ (x = 0.15) measured by Armitage *et al.* with the same photon energy as the present study, the second peak became larger than the lowest energy one near the hot spot [45]. Taking all into account, SC Pr_2CuO_4 has a weaker signature of antiferromagnetism, that is, shorter AF correlation length and/or smaller magnetic moment than the conventional optimally doped $Nd_{2-x}Ce_xCuO_4$. This is intriguing considering the fact that the T_c of SC Pr_2CuO_4 is even higher than that of the optimally doped sample.

Now we discuss the electron concentration of the SC parent compound which can be estimated from the area of the Fermi surface assuming Luttinger theorem [107]. In Fig. 3.8(a), k_F positions of SC Pr_2CuO_4 determined from the peaks of the momentum distribution curves (MDCs) integrated within the energy window of $E_F \pm 10$ meV are plotted. The k_F positions extracted in a wide momentum region shown in Fig. 3.6(c) were gathered to a quarter of the Brillouin zone by symmetry operation, and then symmetrized against Γ-(π, π) line. Error bars were defined as full width at 90 % of the maximum of the fitted curves. Obtained large hole-like Fermi surface centered at (π, π) is consistent with a calculation using local density approximation (LDA) [108], and there is no appreciable distortion around the hot spot, indicating negligible effect of the AF correlation on the Fermi surface. As displayed in Fig. 3.8(a), the Fermi surface was satisfactorily fitted to

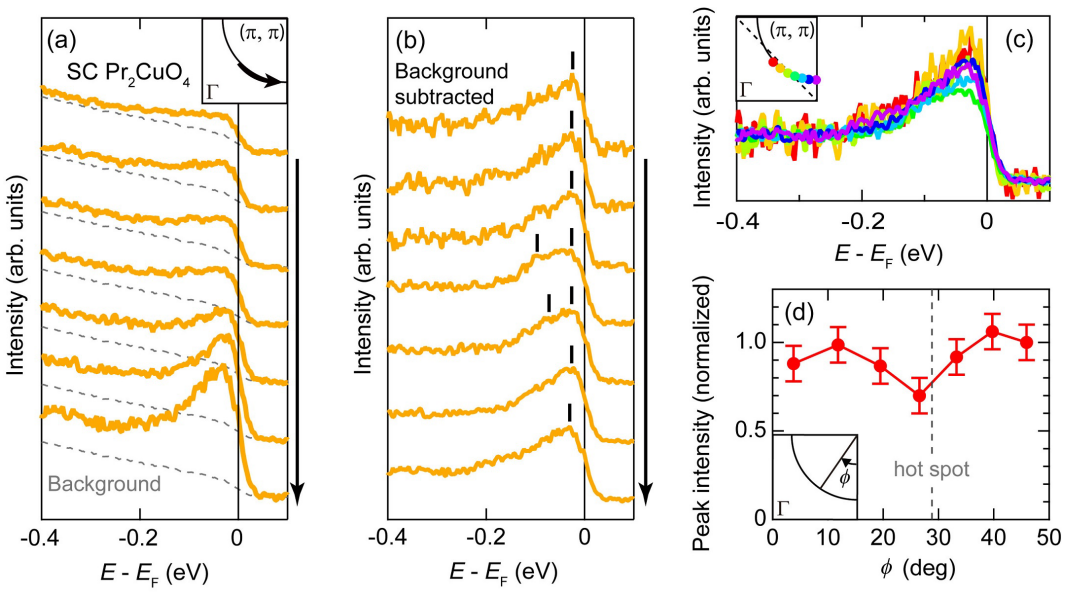

Figure 3.7: EDCs on the Fermi surface of the SC Pr_2CuO_4 sample. (a) EDCs of the SC sample along the Fermi surface from the nodal to antinodal region. The EDCs are not normalized. The background spectrum, which was taken from the momentum region near (π, π), is also plotted (gray dashed curve) with each EDC. (b) EDCs normalized to the peak height after background subtraction. Peak positions are indicated by vertical bars. (c) EDCs normalized to the intensity integrated in the region -0.4 eV $\leq E - E_F \leq -0.25$ eV. after background subtraction. The inset shows the corresponding momentum positions. (d) Momentum dependence of the peak intensity integrated within $E - E_F = \pm 20$ meV. The values have been normalized to that at the nodal point. The Fermi surface angle ϕ is defined in the inset.

the tight-binding model,

$$\begin{aligned}\epsilon - \mu =& \epsilon_0 - 2t(\cos\, k_x a + \cos\, k_y a) \\ & - 4t'\cos\, k_x a\, \cos\, k_y a - 2t"(\cos\, 2k_x a + \cos\, 2k_y a),\end{aligned} \tag{3.1}$$

where t, t', and t'' denote the transfer integrals between the nearest-neighbor, second-nearest-neighbor, and third-nearest-neighbor Cu sites, respectively, and ϵ_0 represents the central energy level of the band relative to the chemical potential μ. Fixing t''/t' at -0.50 in the course of the fitting, we obtained $t'/t = -0.22$ and $\epsilon_0/t = -0.10$. Fitted hole Fermi surface centered at (π, π) occupied 41.5 % of the Brillouin zone, which means that the actual electron-doping level $n_{\rm FS}$ is 0.170 $\pm$ 0.020, considerably deviating from half filling. To demonstrate the experimental accuracy, the Fermi surface whose area corresponds to half filling was reproduced by shifting the chemical potential, and was potted in Fig. 3.8(a). Experimentally determined $k_{\rm F}$ points are unambiguously off the curve, and hence one can safely conclude that SC Pr_2CuO_4 has a larger amount of electrons in the CuO_2 planes than half filling. The present doping level is in the overdoped range of the conventional Ce-doped samples. Since Ce is not substituted in the present samples, the deviation from half filling should be attributed to oxygen non-stoichiometry. In the present case, oxygen deficiency in the CuO_2 planes and/or the PrO layer probably introduced electrons to the parent compound.

As for the non-SC Pr_2CuO_4, the band gap opened around the hot spots and the Fermi surface was reconstructed due to AF fluctuations. However, in the energy region deeper than the magnitude of the AF pseudogap, the original electronic structure without influence of antiferromagnetism should be retained, and hence the constant-energy surface slightly below $E_{\rm F}$ contains the information equivalent to the Fermi surface at $E_{\rm F}$ [49]. In Fig. 3.8, peak positions of the MDCs at 150 meV below $E_{\rm F}$ are plotted for both SC and non-SC Pr_2CuO_4 samples. The constant-energy surface of the non-SC sample is round in shape as in SC sample, although slight distortion is still recognized around the hot spots. Comparing the MDCs along the nodal and antinodal cuts, the peak positions are close to (π, π) for the SC sample (Fig. 3.8(c) and (d), respectively). The size of the constant-energy surface is thus smaller for that of the SC sample with a shorter c-axis parameter, and hence with less oxygen, supporting the claim that oxygen deficiency can dope the system with electrons.

Figure 3.8(e) shows the relationship between $-t'/t$, which controls the curvature of the Fermi surface, and the in-plane lattice constant for various electron-doped cuprates. It has been known from a previous ARPES study on Ce-doped single crystals that $-t'/t$ increases with increasing in-plane lattice constant [50, 93]. The $-t'/t$ of the present SC Pr_2CuO_4 samples is consistent with that tendency, suggesting that not only the carrier concentrations but also basic parameters characterizing the electronic structure such as hopping parameters are similar between

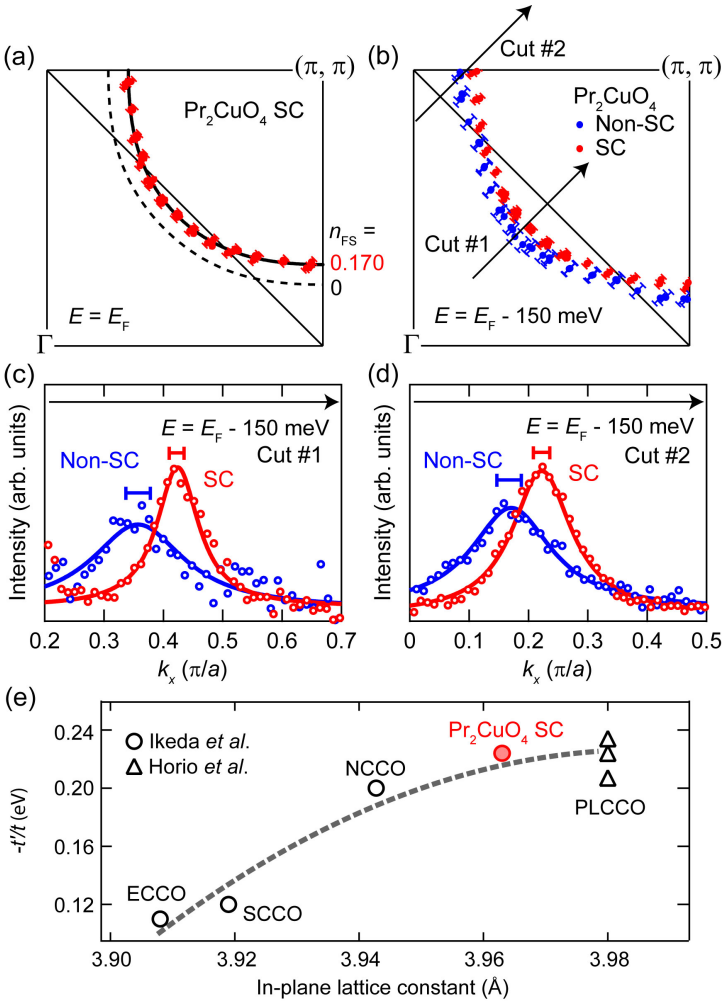

Figure 3.8: Fermi surfaces of Pr_2CuO_4 films. (a) k_F points of the SC sample determined from the peak positions of the MDCs integrated within $E_F \pm 10$ meV (red dots) and fitted to the tight-binding model (solid curve). The area of the fitted Fermi surface corresponds to the electron concentration n_{FS} of 0.170. For comparison, the Fermi surface for $n_{FS} = 0$ (dashed curve) obtained by shifting the chemical potential is also plotted. (b) Peak positions of MDCs at $E = E_F - 150$ meV integrated within the energy window of ± 10 meV for the SC and non-SC Pr_2CuO_4 samples. (c,d) MDCs at the energy of $E = E_F - 150$ meV taken along the cut #1 and #2 indicated in (b) and fitted to a Lorentzian. Error bars of the peak positions are indicated by horizontal bars. (e) $-t'/t$, which represents the curvature of the Fermi surface, obtained by tight-binding fit for various electron-doped cuprates plotted against the in-plane lattice constant. The values for $Eu_{1.85}Ce_{0.15}CuO_4$ (ECCO), $Sm_{1.85}Ce_{0.15}CuO_4$ (SCCO), $Nd_{1.85}Ce_{0.15}CuO_4$ (NCCO), and $Pr_{1.2}La_{0.7}Ce_{0.1}CuO_4$ (PLCCO) are taken from previous studies [50, 93]. The present SC Pr_2CuO_4 thin film follows the trend of the other electron-doped cuprates.

the SC parent compound and the Ce-doped superconductors.

So far, we have revealed that the electronic structure of the SC parent compound Pr_2CuO_4 is close to that of the overdoped superconductors in terms of the AF correlation and the electron concentration. The situation is schematically described in the phase diagram shown in Fig. 3.9. This is apparently at odds with the fact that the T_c of SC Pr_2CuO_4 is even higher than those of conventional optimally Ce-doped superconductors. The difference between the SC parent compound and the Ce-doped SC compounds may originate from the difference in the source of doping. The superconductivity driven by carrier doping always suffers from disorder introduced by chemical substitutions. In the case of electron doping by Ce substitutions, the optimum doping level for $Nd_{2-x}Ce_xCuO_4$ and $Pr_{2-x}Ce_xCuO_4$, ~ 0.15, is close to the solubility limit for the single crystal (~ 0.18) [31], implying the inclusion of the considerable amount of disorder which suppresses T_c. It is plausible that oxygen deficiency at regular sites is less destructive to the superconductivity, and hence T_c remains high even at larger electron concentrations. Similar behavior has recently been observed in our previous study on efficiently annealed $Pr_{1.3-x}La_{0.7}Ce_xCuO_4$ ($x = 0.10$) single crystals, where the T_c became higher than that at the optimum doping level previously reported [91] in return for the drastic increase of electron concentration up to ~ 0.18 and strong suppression of the AF pseudogap after annealing [90, 93]. Based on this idea, the superconductivity in the T'-type cuprates may be optimized at higher electron concentration than previously believed.

Although the present SC Pr_2CuO_4 samples are doped with electrons, we cannot exclude the possibility of superconductivity at half filling in the T'-type cuprates. In the present case, the samples were grown in a reducing condition to prevent the inclusion of excess oxygen, but it probably led to the oxygen deficiency at the regular sites and electrons were doped. If one grows the sample with supplying a sufficient amount of oxygen to avoid oxygen defects at the regular sites, impurity oxygen is also introduced and superconductivity is suppressed. Thus, it is impossible at present to make a sample with the ideal T' structure [109]. The present study has demonstrated that Pr_2CuO_4 grown under a reducing condition can be SC with a large amount of doped electrons, but it is not clear whether the superconductivity is maintained or not when the oxygen defects are filled without introduction of impurity oxygen. If one become able to remove or place oxygen atoms site selectively, an unambiguous answer would be obtained. A possible way to solve the problem is to apply a gate voltage and introduce holes [110] to the SC parent compound, thereby bring the sample back to half-filling without introducing impurity oxygen, and to see whether the superconductivity persists or not.

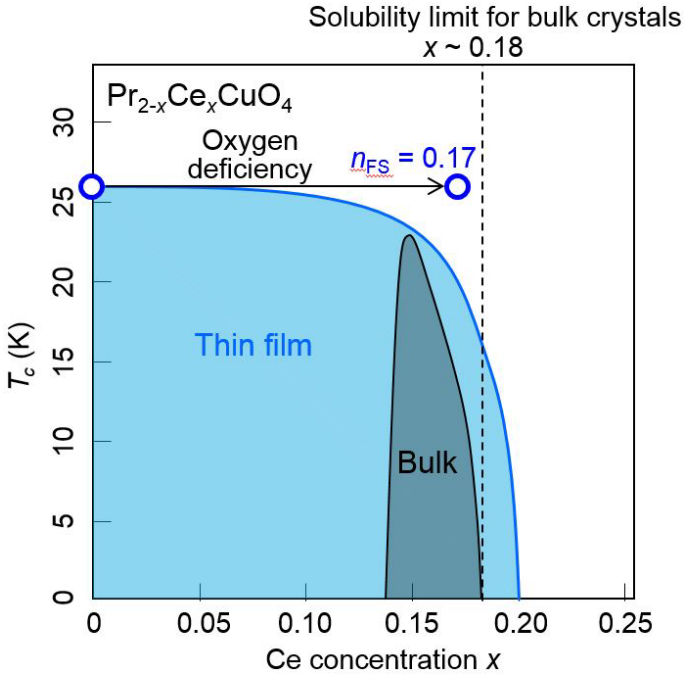

Figure 3.9: Nature of the SC parent compound. Phase diagrams for thin films and bulk crystals are schematically illustrated. Bulk SC dome is close to the solubility limit of Ce (dashed line), and hence T_c is suppressed by disorder. The SC parent compound is doped with electrons only by oxygen deficiency. The oxygen deficiency may be less destructive to the superconductivity, and hence higher T_c is realized.

3.4 Conclusion

In this chapter, we have studied the electronic structure of SC parent compounds of electron-doped cuprates and related materials by means of ARPES. In order to carry out surface sensitive ARPES measurements to reveal detailed low energy electronic structure, we have synthesized SC parent compound Pr_2CuO_4 without *ex-situ* annealing. The key to achieve superconductivity was grow thin films coherently under highly reducing condition (high temperature and low oxygen partial pressure), thereby avoiding the introduction of excess oxygen. The SC properties of thus obtained samples were close to those of *ex-situ* annealed SC parent compound in terms of the T_c and RRR.

We have then performed ARPES measurements on the SC and non-SC Pr_2CuO_4 thin films. While the non-SC sample showed a large AF pseudogap which is indicative of AF long-range or short-range order, the SC sample showed no gap along the Fermi surface, although the spectral intensity was slightly suppressed at the hot spot. The electron-doping level of the SC sample estimated from Fermi surface area was 0.170 ± 0.020, clearly deviating from half filling. Probably, oxygen defects in CuO_2 planes and/or PrO layers are the origin of the additional electrons. The overall electronic structure of the present SC Pr_2CuO_4 resembled that of the Ce-overdoped conventional superconductors, despite the fact that the T_c was even higher than that of the optimally Ce-doped conventional superconductors. The oxygen deficiency may be less destructive to the superconductivity than Ce substitutions, and hence the highest T_c is achieved when electrons are doped only by the oxygen deficiency. Since the present SC Pr_2CuO_4 does not have the ideal T' structure in the sense that oxygen is deficient, the possibility of superconductivity at half filling cannot be excluded at present. Resistivity measurements with varying carrier concentration by applying gate voltage will provide a clue for the possibility.

Chapter 4

Core-level electronic structure of the superconducting parent compound Nd_2CuO_4 and Ce-doped compounds $Nd_{2-x}Ce_xCuO_4$

4.1 Introduction

In the last chapter, we have presented the result of angle-resolved photoemission spectroscopy (ARPES) measurements on the superconducting (SC) parent compound and have revealed that the electron concentration estimated from the area of the Fermi surface is by far larger than the half-filling. In the present chapter, we report the result of relatively bulk sensitive hard X-ray photoemission spectroscopy (HAXPES) and soft X-ray absorption spectroscopy (XAS) measurements on the core levels of the parent compound of T'-type SC cuprates Nd_2CuO_4 and Ce-doped samples $Nd_{2-x}Ce_xCuO_4$. Although core levels reside deeply below the Fermi level (E_F), their spectra reflect changes near E_F so sensitively that core-level spectroscopy provides rich information about the low energy electronic structure, including the position of the chemical potential.

4.2 Experimental

$Nd_{2-x}Ce_xCuO_4$ ($x = 0, 0.15$, and 0.19) thin films for HAXPES and XAS measurements with the thickness of 200 nm, 100 nm, and 100 nm, respectively, were grown on (001) $SrTiO_3$ substrates by molecular beam epitaxy. One of the Nd_2CuO_4

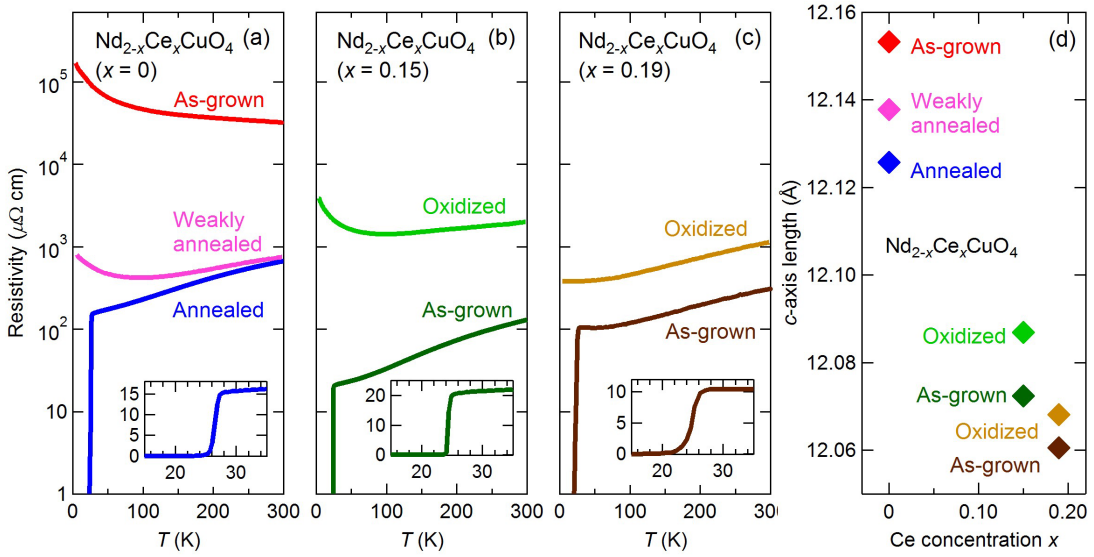

Figure 4.1: Physical properties of $Nd_{2-x}Ce_xCuO_4$ thin films. (a-c) Resistivity versus temperature for the $x = 0$, 0.15, and 0.19 samples, respectively. The inset magnifies the SC transition in each composition. (d) c-axis lengths plotted against Ce concentration x.

samples were annealed in a furnace first at 675 °C under the O_2 partial pressure of 2.5×10^{-4} Torr for 1 hour, and then at 525 °C under UHV for 10 minutes. The annealed Nd_2CuO_4 sample showed superconductivity with the T_c of 25.0 K, while as-grown one was insulating. A weakly annealed Nd_2CuO_4 sample, that is, a sample annealed first at 690 °C under the O_2 partial pressure of 1.0×10^{-3} Torr for 1 hour, and then at 500 °C under UHV for 10 minutes, was metallic at high temperatures but resistivity showed an upturn below 95 K. Ce-doped samples were SC without *ex-situ* annealing with the T_c's of 24.0 K and 21.5 K for $x = 0.15$ and for $x = 0.19$, respectively. The Ce-doped samples were cut into pieces and one of them was oxidized by heating up to 600 °C for 10 minutes under the O_3 pressure of 1×10^{-6} Torr, and the superconductivity was suppressed. Resistivity curves and c-axis lengths of all the samples are plotted in Fig. 4.1. HAXPES measurements were performed at beamline 47-XU of SPring-8 with $h\nu = 7.94$ keV photons with grazing incidence to maximize the photoemission intensity [111]. The total energy resolution was set at 0.3 eV. XAS measurements were performed at beamline 07-LSU of SPring-8. Two kinds of linearly polarized light, with polar angle $\theta = \pi/2$ (parallel to the sample surface) and $\theta = \pi/6$, were used for the measurements. All the measurements were performed under the pressure better than 5×10^{-9} Torr and at 300 K.

4.3 Results and discussion

Figure 4.2 shows Cu $2p_{3/2}$ core-level HAXPES spectra of as-grown and annealed Nd_2CuO_4 samples normalized to the total intensity in the displayed region, and the difference between them. The large repulsive potential between the core hole created by photoemisson at the Cu $2p$ level and holes which originally exist at the Cu $3d$ level gives rise to lower energy final state where electrons are transfered from O $2p$ to Cu $3d$ to screen the core-hole potential, making the spectrum of the as-grown sample split into two groups: $2p^5 3d^9$ unscreened final state leading to a satellite at $\sim$ 943 eV and the charge-transfer screened final state leading to the main peak at $\sim$ 934 eV. The main peak consists of four features reflecting different types of core-hole screening. As has been discussed for the Cu $2p$ spectrum of insulating cuprates such as La_2CuO_4 [112, 113] and $Sr_2CuO_2Cl_2$ [114, 115] using multi-site cluster calculation, the peak at the highest binding energy corresponds to the final state usually denoted by $2p^5 3d^{10}\underline{L}$ where an electron is transferred from neighboring oxygen (local screening), and the two peaks in the middle to the final state where an electron is transferred from oxygen in the neighboring CuO_4 plaquette thereby creating a Zhang-Rice singlet (non-local screening). Apart from the unassigned peak at the lowest energy labeled as α in Fig. 4.2 which shall be discussed in the following, the shape of the main peak resembles those of other insulating cuprates with two-dimensional CuO_2 planes, supporting the previous proposal of the universality of the core-hole screening process in two-dimensional Cu-O network [115].

Upon annealing, the peak α is strongly enhanced and the overall line shape of the main peak drastically changes. The binding energies of the charge-transferred final state are related to the energy levels of the electronic states from which the electron is transferred to screen the core-hole potential. Therefore, the enhancement of the lowest energy peak indicates the development of electronic states closer to the Fermi level (E_F). Peak α has also been observed in previous HAXPES studies on $Nd_{2-x}Ce_xCuO_4$ ($x = 0.15$) [112,116] and attributed to final states where core hole is screened by conduction electrons introduced by Ce substitution. The observed change in the present Cu $2p$ spectra thus suggests that conduction electrons were introduced by annealing, consistent with the occurrence of superconductivity observed in the annealed Nd_2CuO_4.

The effect of the annealing on the Nd and O core levels is shown in Fig. 4.3. Upon annealing, the Nd $3d_{5/2}$ peak is shifted toward higher binding energy by 0.22 eV [Fig. 4.3(a)]. As for the O $1s$ peak, a shift of similar amount (0.21 eV) is observed at the edge, but the spectral line shape is also modified by annealing: the full width at half maximum (FWHM) decreased from 1.44 eV to 1.16 eV and a long high binding energy tail emerges above $\sim$ 529.5 eV [Fig. 4.3(b)]. Such changes have not been detected in the doping and annealing dependence of the O

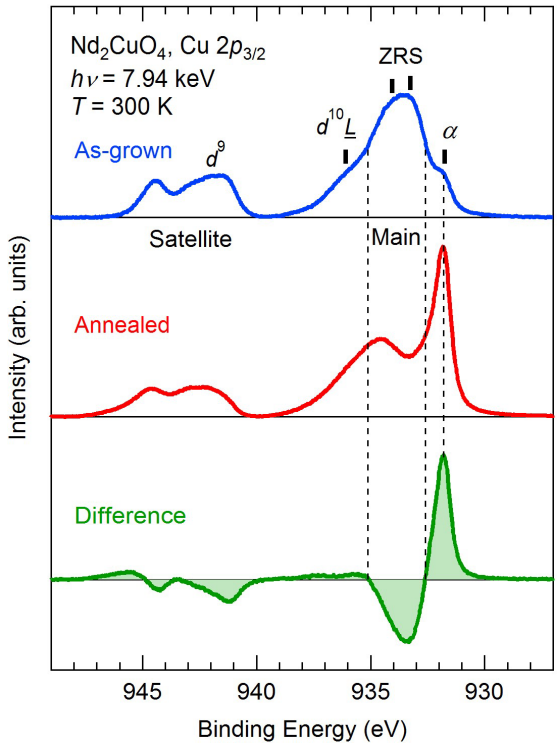

Figure 4.2: Cu $2p_{3/2}$ core-level HAXPES spectra of as-grown Nd_2CuO_4 (top), annealed Nd_2CuO_4 (middle), and their difference (bottom). Final states where the core holes are unscreened ($2p^5 3d^9$), screened by an electron transferred from neighboring oxygen atoms ($2p^5 3d^{10}\underline{L}$), screened by an electron transferred from neighboring CuO_4 plaquettes thereby creating a Zhang-Rice singlet (ZRS), or screened by conduction electrons (α) were observed.

$1s$ photoemission spectra of $Nd_{2-x}Ce_xCuO_4$ reported in previous studies [104,117]. In order to disentangle this complicated spectral deformation, the O $1s$ spectrum of as-grown sample has been closely examined as follows.

Calculation method	O_{NdO} (eV)	O_{CuO_2} (eV)
(i)	527.93	528.36
(ii)	527.81	528.38
(iii)	527.54	528.53

Table 4.1: O $1s$ binding energies estimated from DFT calculations. Details of the calculations are described in the text.

The peak region of the O $1s$ spectrum of the as-grown sample is rather flat, indicating the existence of two components in different chemical states, and we attributed them to oxygen atoms in the NdO layers (O_{NdO}) and those in the CuO_2 planes (O_{CuO_2}) which are contained in Nd_2CuO_4 with equal amount. In order to ascribe each peak to each oxygen atom, O $1s$ binding energies observable by photoemission spectroscopy were estimated from the calculation of Slater transition states [118] using density functional theory (DFT). Calculations were carried out using the generalized gradient approximations (GGA). For the $4f$ orbital, since GGA generally yields unrealistically high density of states (DOS) in a narrow energy window around E_F, which could affect the O $1s$ binding energy, we have carried out three different kinds of calculations:
(i): Nd_2CuO_4 with GGA
(ii): La_2CuO_4 with the lattice constant of Nd_2CuO_4 with GGA
(iii): Nd_2CuO_4 with GGA+U ($U_{4f} = 9$ eV)
in (ii), Nd is replaced by La, where $4f$ levels are unoccupied, and the $4f$ level is located far above E_F. In (iii), on-site Coulomb repulsion $U = 9$ eV is introduced to the Nd $4f$ orbitals thereby splitting the $4f$ DOS away from E_F. All the calculations were performed with spin polarization and the O $1s$ binding energies were finally determined by taking the average of spin-down and -up binding energies. The calculated O $1s$ binding energies are listed in Table. 4.1. Although the magnitude of the difference between the O_{NdO} and O_{CuO_2} $1s$ binding energies depends on the calculation method, O_{NdO} always resides at a lower binding energy and O_{CuO_2} at a higher binding energy. Therefore, we assumed that the O_{NdO} peak is at a lower binding energy for the analysis of the experimental spectra.

The O $1s$ spectrum of as-grown Nd_2CuO_4 was fitted to a superposition of a Voigt function (for O_{NdO}) and Mahan line shape $\frac{1}{\Gamma(\alpha)}\frac{e^{-(E_B-E_0)/\xi}}{|(E_B-E_0)/\xi|^{1-\alpha}}\Theta(E_B - E_0)$ convolved with a Voigt function (for O_{CuO_2}). The asymmetric Mahan line shape was assumed for O_{CuO_2} considering core-hole screening by low energy particle-hole excitation characteristic of a metallic states. The FWHM of the Lorentian

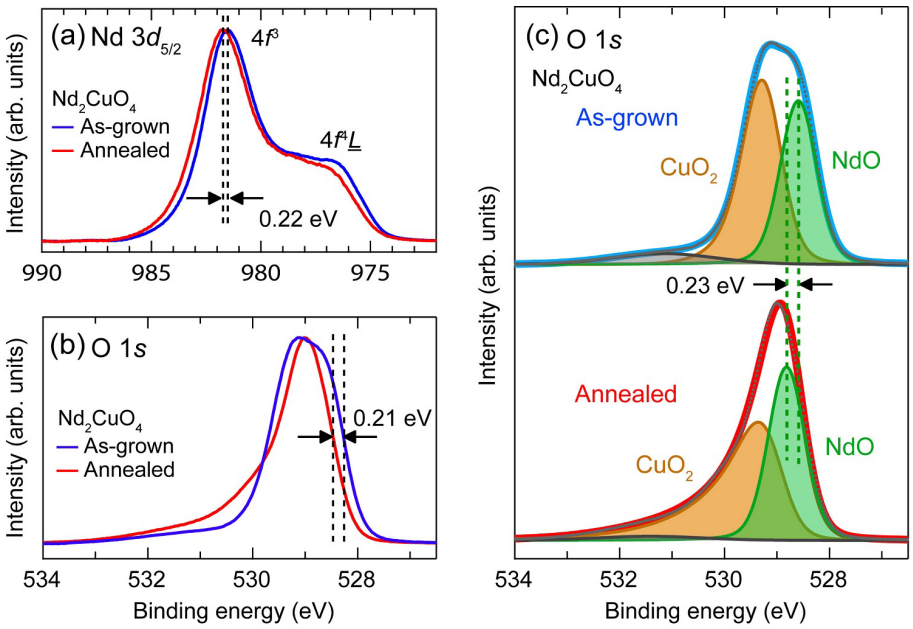

Figure 4.3: Effect of annealing on the Nd and O core levels. (a,b) Nd $3d_{5/2}$ and O $1s$ core-level peaks, respectively, for as-grown and annealed Nd_2CuO_4 samples. The spectra have been normalized to the peak height. (c) O $1s$ spectra of as-grown (top) and annealed (bottom) samples fitted to a superposition of a Voigt function (for O in the NdO layers, green), Mahan line shape $\frac{1}{\Gamma(\alpha)}\frac{e^{-(E_B-E_0)/\xi}}{|(E_B-E_0)/\xi|^{1-\alpha}}\Theta(E_B-E_0)$ convolved with a Voigt function (for O in the CuO_2 planes, orange), and another Voigt function (for contamination O, black).

and Gaussian in the Voigt function was assumed to be the same for both peaks. Another Voigt function was added to the fitting function to reproduce a weak component at ~ 531 eV, which probably arose from contamination at the surface. The fitting yielded two peaks for the as-grown sample with the area ratio 0.45 : 0.55, as shown in the top panel of Fig. 4.3(c), consistent with the fact that the number of oxygen atoms in the NdO layers and the CuO_2 planes are the same. The obtained value of α, which determines the asymmetry of the Mahan line shape, was 0.10. The obtained FWHM of the Lorentzian was 0.15 eV, which is close to the inherent O 1s core-hole lifetime of 0.16 eV observed for H_2O [119], while the FWHM of the Gaussian was 0.74 eV, which is larger than the experimental total resolution of 0.3 eV possibly due to the contribution from phonons [120]. The

The O 1s spectrum of the annealed sample was then fitted to the same functional form with the FWHM of the Lorentzian and the Gaussian fixed to the values of the as-grown sample. While the area of each component was almost preserved, the peak at higher binding energy was deformed and became highly asymmetric ($\alpha = 0.63$), reproducing the long tail of the experimental spectrum. The asymmetry for the O_{CuO_2} peak arising from the low energy particle-hole excitations for screening core-hole potential is consistent with the increase of the electrical conductivity in CuO_2 planes by annealing. On the other hand, the peak of O_{NdO} shifted toward higher binding energy with annealing by 0.23 eV, nearly the same amount as the edge shift of the total spectra [Fig. 4.3(b)]. Thus, the present analysis enables us to explain the change in O 1s spectra induced by the annealing: The edge shift originated from the shift of the O_{NdO} peak, and the apparent narrowing and the long tail arose from the strong asymmetry of the O_{CuO_2} peak caused by the dramatic increase of the conductivity in the CuO_2 planes.

Thus, annealing shifted Nd $3d_{5/2}$ peak and the O_{NdO} 1s peak by almost the same amount without remarkable change in the line shapes. The shift of the core-level binding energy is given by [121]

$$\Delta E_B = \Delta\mu - K\Delta Q + \Delta V_M - \Delta E_R, \tag{4.1}$$

where $\Delta\mu$ is the change in the chemical potential, ΔQ is the change in the number of valence electrons, K is a constant, ΔV_M is the change in the Madelung potential, and ΔE_R is the change in the extra-atomic screening of the core-hole potential by conduction electrons and/or dielectric polarization of surrounding media. Almost identical shifts observed for Nd 3d and O_{NdO} 1s core levels indicate that ΔV_M is negligibly small because it would shift the core levels of the O^{2-} anion and the Nd^{3+} cation in different ways. ΔE_R cannot be the main origin of the observed shifts, either because the increase of conduction electrons by annealing would shift the core-level peaks toward lower binding energy, in the opposite direction to the experimental observation. Therefore, we conclude that the observed shifts are largely due to the chemical potential shift $\Delta\mu$. The increase of the core-level

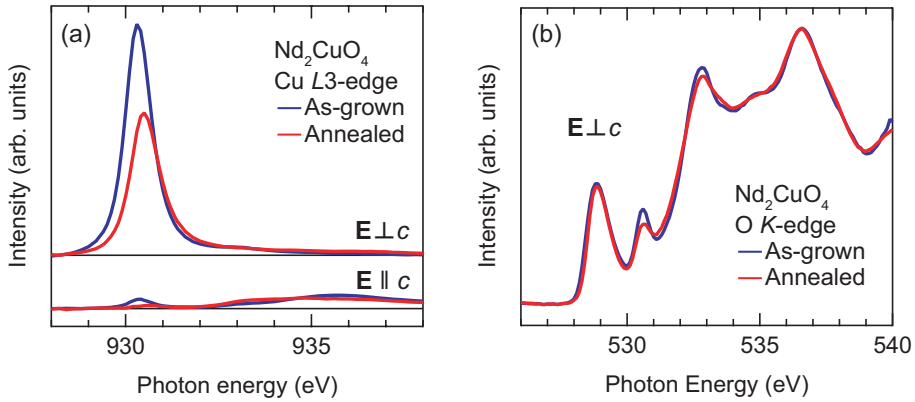

Figure 4.4: XAS spectra of Nd_2CuO_4 thin films. (a) Cu $L3$-edge XAS spectra for $\mathbf{E} \perp c$ (top) and $\mathbf{E} \parallel c$ (bottom). The spectra for $\mathbf{E} \parallel c$ was obtained by subtracting the contribution of $\mathbf{E} \perp c$ from the spectra measured with $\theta = \pi/6$ polarization. The spectra have been normalized to the intensity of the Nd XAS peak at 978 eV. (b) O K-edge XAS spectra taken with $\mathbf{E} \perp c$ and normalized to the intensity integrated from 532 eV to 540 eV.

binding energies by annealing indicates the increase of $\Delta\mu$ due to the addition of electrons. The observed shifts are close to those previously observed between as-grown Nd_2CuO_4 and as-grown $Nd_{2-x}Ce_xCuO_4$ ($x = 0.15$) single crystals (~ 0.22 eV) [117], suggesting that annealing introduced ~ 0.15 electrons to the Nd_2CuO_4 thin film.

The orbital character of the doped electrons can be studied by polarization dependent XAS measurements. Using Fermi's golden rule, matrix elements for Cu L-edge absorption relevant to the present study with light polarized along $\mathbf{n} = (\sin\theta\cos\phi, \sin\theta\sin\phi, \cos\theta)$ can be written as follows [122]:

$$\langle 2p_{\mathrm{in-plane}} | H' | 3d_{x^2-y^2} \rangle^2 = \sum_{i=x,y} \langle 2p_i | H' | 3d_{x^2-y^2} \rangle^2 = M_{if}^2 \sin^2\theta \quad (4.2)$$

$$\langle 2p_{\mathrm{in-plane}} | H' | 3d_{3z^2-r^2} \rangle^2 = \sum_{i=x,y} \langle 2p_i | H' | 3d_{3z^2-r^2} \rangle^2 = \frac{1}{3} M_{if}^2 \sin^2\theta \quad (4.3)$$

$$\langle 2p_z | H' | 3d_{x^2-y^2} \rangle^2 = 0 \quad (4.4)$$

$$\langle 2p_z | H' | 3d_{3z^2-r^2} \rangle^2 = \frac{2}{3} M_{if}^2 \cos^2\theta, \quad (4.5)$$

where H' is the Hamiltonian for electron-photon interaction, and M_{if} is a reduced matrix element. Therefore, absorption with polarization perpendicular to the c axis ($\mathbf{E} \perp c$, $\theta = \pi/2$) is 75 % due to the transition into the $3d_{x^2-y^2}$ orbital, and that with polarization parallel to the c axis ($\mathbf{E} \parallel c$, $\theta = 0$) is entirely due to transitions

into the $3d_{3z^2-r^2}$ orbital. Experimentally obtained Cu $L3$-edge XAS spectra for $\mathbf{E} \parallel c$ and $\mathbf{E} \perp c$ for as-grown and annealed Nd_2CuO_4 are shown in Fig. 4.4(a). The spectra for $\mathbf{E} \parallel c$ were obtained by subtracting the contribution of $\mathbf{E} \perp c$ from the spectra measured with $\theta = \pi/6$ polarization. While the XAS spectra for $\mathbf{E} \perp c$ show an intense peak at ~ 930 eV and its intensity decreases with annealing by 30 %, suggesting the reduction of unoccupied DOS near E_F as reported for Ce-doped samples [122–124], spectra for $\mathbf{E} \parallel c$ are negligibly weak. The ratio of $3d_{3z^2-r^2}$ weight to $3d_{x^2-y^2}$ weight in the lowest-energy peak is as small as 4 % and 2 % for as-grown and annealed Nd_2CuO_4, respectively, in agreement with the values reported in previous studies [122, 124]. Therefore, the $3d_{3z^2-r^2}$ orbitals are almost completely filled regardless of whether annealed or not, and additional electrons are doped into the $3d_{x^2-y^2}$ orbitals by annealing. On the other hand, as shown in Fig. 4.4(b), the pre-edge peak (~ 529 eV) in O K-edge XAS measured with $\mathbf{E} \perp c$, which represents the transition from O $1s$ to in-plane O $2p$ orbitals hybridized with the upper Hubbard band, shows only a slight change (5 %) in contrast to Cu L-edge XAS for $\mathbf{E} \perp c$. This agrees with the changes observed by Ce doping in the previous studies and suggests that the orbital character of the upper Hubbard band is dominated by $3d_{x^2-y^2}$ [122–125].

Having established that the chemical potential of Nd_2CuO_4 was shifted due to additionally introduced electrons by annealing, we compare the core-level spectral line shapes of Nd_2CuO_4 with those of Ce-doped compounds with varying oxygen content either by annealing or oxidation. In Fig. 4.5, core-level HAXPES spectra for Nd_2CuO_4 (as-grown, weakly annealed, annealed) and $Nd_{2-x}Ce_xCuO_4$ ($x = 0.15, 0.19$, as-grown, oxidized) are plotted. The Nd and Ce peak positions are shifted between samples, but their spectral line shapes are almost identical. On the other hand, the O $1s$ peaks change their shape with varying doping level and oxygen content. In fact, the spectral line shapes are similar among annealed Nd_2CuO_4 and as-grown $Nd_{2-x}Ce_xCuO_4$ ($x = 0.15, 0.19$), suggesting that the line-shape deformation seen in Fig. 4.3(b) is not specific to the SC parent compound, but general for the T'-type cuprate superconductors including Ce-doped ones although it has not been detected in previous studies [104, 117]. Low intensity of the contamination peak at ~ 531 eV due to the bulk sensitivity of HAXPES and high energy resolution (300 meV) is probably the key to observe the subtle changes in the line shape. Because the changes in the O $1s$ peaks can be understood within the above scenario, we compare the low energy edges of different samples as representing the O_{NdO} peak position, and summarize them in Fig, 4.6(a). Not only the Nd $3d$ and O $1s$ core-level peaks, but also the Ce $3d$ peaks are shifted by the same amount for every sample (The origins of the shifts of the Ce $3d$ were set at the Nd $3d$ shift for the $x = 0.15$ oxidized sample.), confirming that the core-level shift corresponds to the chemical-potential shift.

The chemical-potential shift relative to the as-grown Nd_2CuO_4, $\Delta\mu$ defined

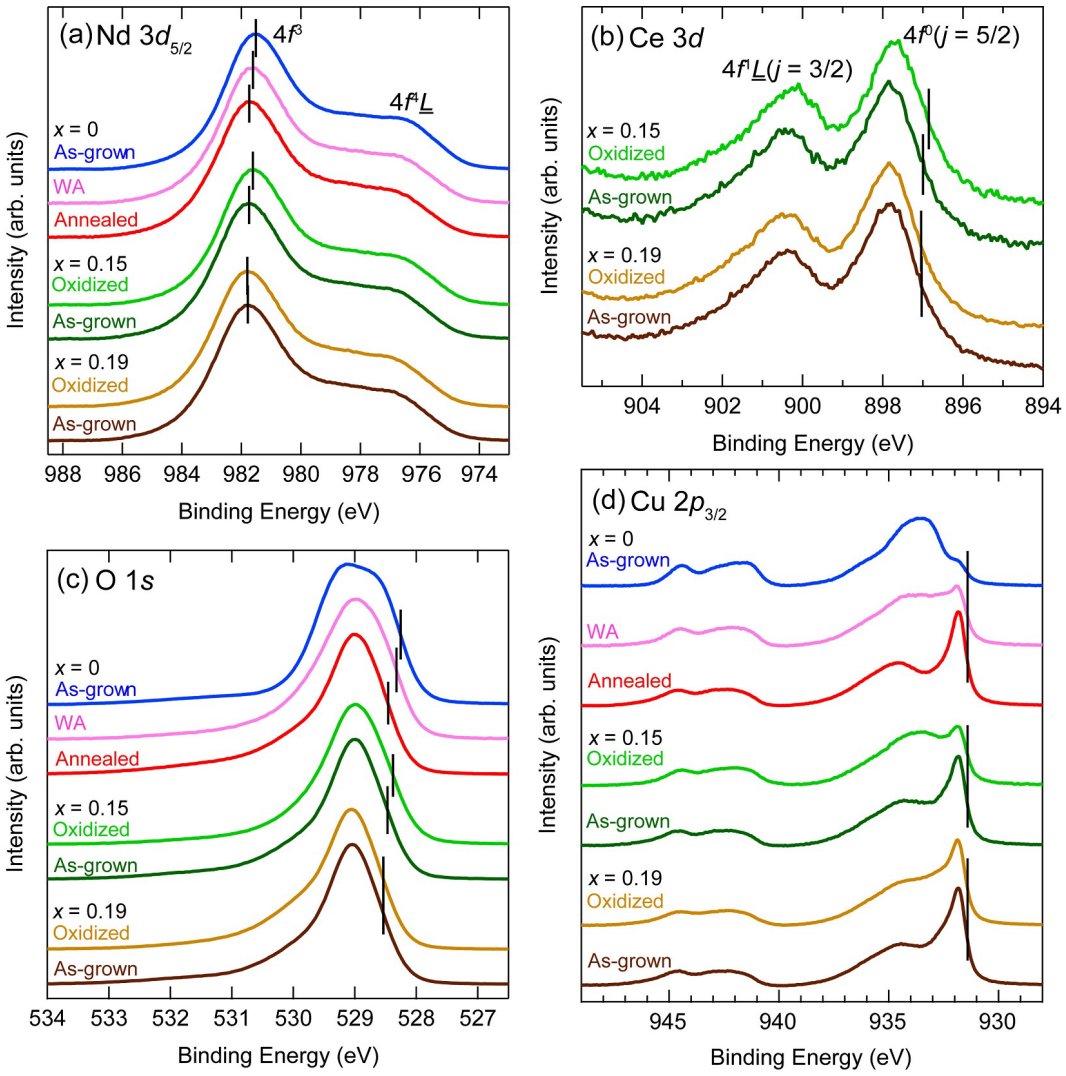

Figure 4.5: Core-level HAXPES spectra of $Nd_{2-x}Ce_xCuO_4$ thin films. (a) Nd $3d_{5/2}$. (b) Ce $3d$. (c) O $1s$. (d) Cu $2p_{3/2}$. The weakly annealed Nd_2CuO_4 sample is labeled as "WA". Peak or edge positions are indicated by vertical bars.

as the average shift of Nd $3d$ and O $1s$, are plotted in Fig, 4.6(b) against Ce concentration x together with those for $Nd_{2-x}Ce_xCuO_4$ as-grown non-SC single crystals reported by Harima *et al.* [117]. For Nd_2CuO_4, the chemical potential is shifted upwards with annealing by the amount depending on the annealing condition. On the other hand, for $Nd_{2-x}Ce_xCuO_4$ ($x = 0.15$), the chemical potential is shifted downwards by oxidation. Actual electron concentration n_μ for each thin film was estimated from comparison with the chemical-potential shift of the as-grown $Nd_{2-x}Ce_xCuO_4$ bulk single crystals in the previous study, assuming that the electron concentrations of the as-grown single crystals are the same as the amount of doped Ce x. Using the relationship $\Delta\mu = 1.44x$ obtained from the bulk single crystals, n_μ was evaluated to be 0.149 ± 0.035 for annealed SC Nd_2CuO_4, which is quite large in spite of the absence of Ce. For $Nd_{2-x}Ce_xCuO_4$ ($x = 0.15$), as-grown SC sample had $n_\mu = 0.156 \pm 0.035$, while oxidized sample had $n_\mu = 0.082 \pm 0.035$ which is remarkably smaller than the Ce content. These results demonstrates that the position of the chemical potential, i.e., carrier concentrations, can be controlled in both directions by varying oxygen content. The n_μ for the annealed Nd_2CuO_4 sample, which is considerably larger than the Ce concentration, could be explained if oxygen atoms were removed from regular (CuO_2-plane and/or NdO-layer) sites. Although annealing was intended to remove excess oxygen atoms at the apical site, oxygen could also be removed from the regular site, leading to the total oxygen content less than the stoichiometric one. On the other hand, upon oxidation of $Nd_{2-x}Ce_xCuO_4$ ($x = 0.15$), impurity oxygen was probably introduced to the apical site and doped holes, bringing n_μ smaller than the Ce concentration.

While the Nd, O, and Ce core levels were shifted by a few hundreds meV, the shifts observed for the edge of the lowest energy peak in the Cu $2p$ core-level spectrum was rather small as plotted in Fig. 4.6(a). The smallness of the Cu 2p peak-edge shift can be understood considering the similarity between the well-screened final states of the Cu $2p$ core-level spectra and the Cu $3d$ valence-band spectra [126, 127]. Upon photoemission from the Cu $2p$ core level, a Cu $3d$ valence hole is ejected out of the core-hole site (an electron is transferred to the Cu $3d$ core-hole site) due to the strong repulsive potential U_{cd} between the Cu 2p core hole and the valence hole in Cu $3d$. In the case of photoemission from the Cu $3d$ valence band, large repulsive potential U between the two valence holes in the Cu $3d$ band similarly pushes one of the valence holes out. Since the values of U_{cd} and U are close to each other (20-30 % difference), the structure of Cu $2p$ and $3d$ photoemission spectra resemble each other and the low energy edge of the Cu $2p$ spectra would correspond to the Fermi edge in the Cu $3d$ spectra. Thus, it is reasonable that the binding energy of the Cu $2p$ peak edge is insensitive to the chemical-potential shift [126]. The analogy between the Cu $2p$ and $3d$ spectra can also be seen in the deformation of the Cu $2p$ main peak upon electron doping as presented in Fig. 4.2, where annealing and resulting electron doping caused redistribution of the spectral

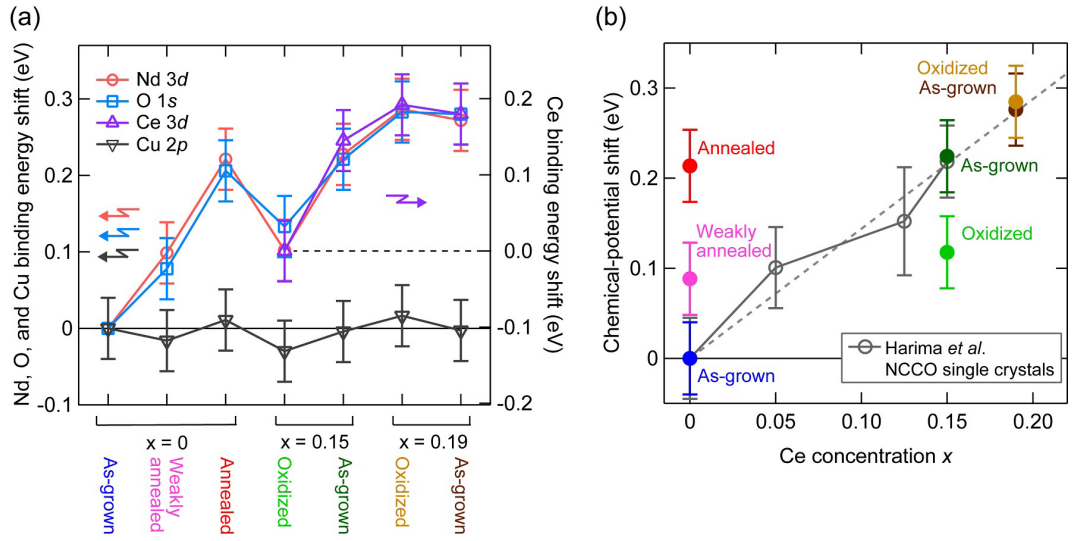

Figure 4.6: Chemical-potential shift in $Nd_{2-x}Ce_xCuO_4$ thin films. (a) Binding energy shifts of the Nd $3d$, O $1s$, Ce $3d$, and Cu $2p$ core levels. The shifts were estimated at the peak top for Nd $3d$ and at the peak edge for O $1s$, Ce $3d$, and Cu $2p$. The origin of the shifts of Ce $3d$ are set at the shift of Nd $3d$ for the $x = 0.15$ oxidized sample. (b) Chemical-potential shifts $\Delta\mu$ defined as the average shift of Nd $3d$ and O $1s$ plotted against Ce concentration x. The same quantities from the previous soft X-ray photoemission study on as-grown non-SC $Nd_{2-x}Ce_xCuO_4$ single crystals by Harima *et al.* [117] are also plotted. A dashed line represents $\Delta\mu = 1.44x$, which is obtained by assuming the linearity between $\Delta\mu$ and x from the previous result by Harima *et al.*

weight in the main peak. Interestingly, however, the spectral weight transfer to the lowest energy peak occurred mainly from the final states where Zhang-Rice singlet is formed rather than from the $2p^5 3d^{10}\underline{L}$ final state. This certainly reflects the spectral-weight transfer from Zhang-Rice singlet band to near-E_F state observed in the valence band of $Nd_{2-x}Ce_xCuO_4$ single crystals with electron doping [12], which is characteristic of a charge-transfer insulator [128, 129].

Finally, we emphasize a peculiar behavior observed for the $Nd_{2-x}Ce_xCuO_4$ ($x = 0.19$) samples. As-grown and oxidized $x = 0.19$ samples showed negligible difference in their n_μ values as shown in Fig. 4.6(b) (0.192 ± 0.035 and 0.198 ± 0.035, respectively). This is consistent with the fact that the elongation of the c-axis lattice parameter by oxidization is rather small for the $x = 0.19$ sample (0.06 %) compared to that for $x = 0.15$ sample (0.12 %), indicating the tiny amount of oxygen incorporation by oxidation. This behavior is basically consistent with the tendency which has been observed in single crystals of $Nd_{2-x}Ce_xCuO_4$ that the amount of the change in the oxygen content by annealing decreases with increasing Ce concentrations [22, 130, 131] although the present composition ($x = 0.19$) is beyond the solubility limit of the single crystal ($x = 0.18$) [31]. It is surprising that the tiny amount of additional oxygen suppressed the superconductivity in $Nd_{2-x}Ce_xCuO_4$ ($x = 0.19$) as shown in Fig. 4.1(c) with maintaining the electron concentration higher than the other SC samples such as the annealed $x = 0$ and the as-grown $x = 0.15$ samples, suggesting that the tiny amount of impurity apical oxygen atoms indeed give rise to strong pair-breaking scattering [26]. Although we have revealed that oxygen content changes the electron concentrations, one should also pay special attention to the critical role of the tiny amount of the excess oxygen, which may make post-growth annealing mandatory to induce the superconductivity to bulk Ce-doped crystals.

4.4 Conclusion

In this chapter, we have studied the electronic structure of SC parent compounds of electron-doped cuprates Nd_2CuO_4 and Ce-doped materials with various oxidizing condition by relatively bulk sensitive HAXPES and XAS. When the parent compound Nd_2CuO_4 was annealed and made SC, Nd 3d and Ce 3d HAXPES peaks were shifted toward higher binding energy, and the line shapes of Cu 2p and O 1s HAXPES peaks were strongly modified. We have shown that these changes arose from the chemical-potential shift due to doped electrons and the enhancement of the conductivity in the CuO_2 planes. XAS measurements on Nd_2CuO_4 have supported introduction of additional electrons into the Cu $3d_{x^2-y^2}$ orbital by annealing. Extending the study to the Ce-doped materials, we have found that the chemical potential was shifted upward by annealing, but was shifted downward by

oxidizing $Nd_{2-x}Ce_xCuO_4$ ($x = 0.15$), suggesting that the chemical potential can be controlled in both directions by oxygen non-stoichiometry: The upward shift may be due to the creation of oxygen defects at the regular sites and resulting electron doping, and the downward shift may be due to the introduction of impurity oxygen at the apical site and resulting hole doping. From comparison with the chemical-potential shifts reported in a previous photoemission study on as-grown $Nd_{2-x}Ce_xCuO_4$ single crystals, we have estimated the electron-doping level in the SC Nd_2CuO_4 to be $n_\mu = 0.149 \pm 0.035$.

Chapter 5

Effect of protect annealing versus Ce doping on the electronic structure of underdoped $Pr_{1.3-x}La_{0.7}Ce_xCuO_4$

5.1 introduction

Since the superconductivity in the parent compounds of the electron-doped cuprate superconductors in thin film form was reported [19, 71, 73, 77–86], their electronic structure has attracted much interest. Inspired by this breakthrough, Adachi *et al.* [90] has developed a new annealing method for bulk single crystals, which is called protect annealing, where the single crystal is covered with polycrystals of the same material and with the same composition during the annealing procedure. Owing to the polycrystals protecting the surfaces of the single crystal, more strongly reducing condition can be applied than before without decomposing the surfaces, enabling us to remove the excess oxygen atoms more efficiently. In fact, it has been shown that protect-annealed $Pr_{1.3-x}La_{0.7}Ce_xCuO_4$ (PLCCO) single crystals exhibit superconductivity down to heavily underdoped region (Ce concentration $x \sim 0.05$), while PLCCO single crystals annealed using the conventional method showed superconductivity only above $x \sim 0.13$ in the previous study by Sun *et al.* [91]. Our angle-resolved photoemission spectroscopy (ARPES) study on the protect-annealed PLCCO ($x = 0.10$) has revealed that a pseudogap of the AF origin is strongly suppressed by protect annealing, suggesting the reduction of the AF correlation length and/or the magnetic moment, which is accompanied by the increase of the electron concentration estimated from the Fermi surface area by up to $\sim$ 0.08 [93]. The electron doping effect of oxygen reduction has also been observed for thin films of the parent-compound superconductor Pr_2CuO_4 and

Nd_2CuO_4 in chapters 3 and 4 of the present thesis. However, considering the fact that electron doping by Ce substitution alone cannot induce superconductivity in bulk samples, the essential role of the annealing may not be electron doping but another unknown effect. Therefore, it is important to reveal the unknown role of annealing other than the doping effect.

In the present chapter, we report ARPES measurements on underdoped PLCCO ($x = 0 - 0.10$) single crystals with varying annealing conditions to investigate the different effects of Ce doping and annealing on the electronic structure.

5.2 Experimental

Single crystals of PLCCO with $x = 0$, 0.02 ,0.05, and 0.10 were synthesized by the traveling-solvent floating-zone method and then protect annealed. The $x = 0$ and 0.05 samples were annealed first at 800 °C for 24 hours and then at 400 °C for 48 hours. The $x = 0.02$ sample was annealed first at 825 °C for 24 hours and then at 400 °C for 48 hours. The $x = 0.10$ sample was annealed at 800 °C for 24 hours. We performed ARPES measurements on six samples: as-grown samples with $x = 0.05$ and 0.10, and annealed samples with $x = 0, 0.02, 0.05$, and 0.10. The resistivity-temperature curves for all the six samples are plotted in Fig. 5.1. While the resistivity of as-grown samples diverged at low temperatures [Fig. 5.1(c) and (d)], the annealed samples did not show divergence even for $x = 0$ [Fig. 5.1(a)]. The annealed $x = 0.02$ sample showed metallic behavior at high temperatures, but was not superconducting. [Fig. 5.1] The annealed $x = 0.05$ sample showed an onset of superconductivity at T $\sim$ 26 K, but the resistivity did not reach zero Fig. 5.1(c). The annealed $x = 0.10$ sample showed bulk superconductivity with the $T_c = 27$ K. According to muon spin relaxation measurements, annealed samples with $x = 0.10$ showed short-range AF order at 10 K, where ARPES measurements were performed, while the AF order in annealed sample with $x = 0.05$ was either long-ranged with very small internal field or short-ranged. All of the other samples exhibited long-range AF order at 10 K. ARPES measurements were carried out at beamline 5-4 of Stanford Synchrotron Radiation Lightsource. Circularly polarized light with $h\nu = 16.5$ eV was used for the measurements. The total energy resolution was set at 15 meV. The sample was cleaved *in-situ* under pressure better than 3×10^{-11} Torr and measured at 10 K. An Energy distribution curve (EDC) near (π, π) has been subtracted as a momentum independent background from all of the ARPES spectra shown in the present chapter. X-ray core-level photoemission spectroscopy measurements were also performed with laboratory-based X-ray photoemission (XPS) apparatus using Al $K\alpha$ line ($h\nu = 1486.6$ eV) and at beamline 2A of Photon Factory with $h\nu = 1400$ eV. The XPS measurements were performed at $T = 300$ K under the pressure better than 3×10^{-9} Torr and 2×10^{-10} Torr for

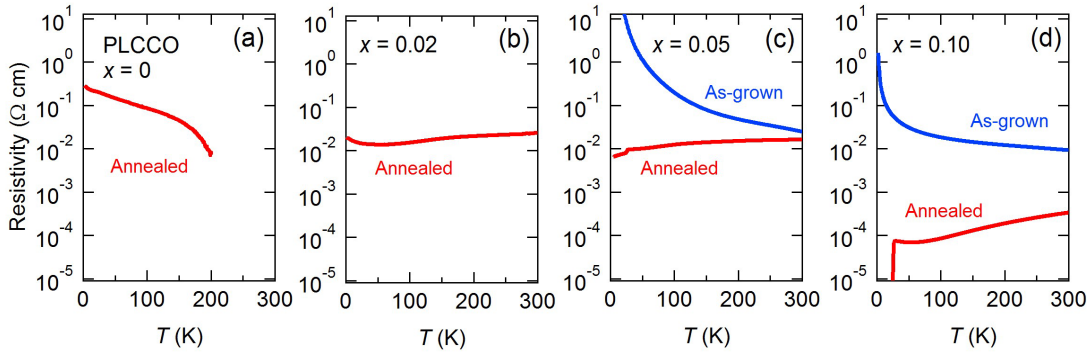

Figure 5.1: Resistivity of PLCCO single crystals plotted against temperatures. (a) Annealed $x = 0$ sample. (b) Annealed $x = 0.02$ sample. (c) As-grown and Annealed $x = 0.05$ samples. (d) As-grown and annealed $x = 0.10$ samples.

laboratory-based apparatus and at Photon Factory, respectively.

5.3 Results and discussion

Figures 5.2(a1)-(a6) show the Fermi surface mappings of the PLCCO samples. Surprisingly a Fermi surface was found to exist even for the $x = 0$ sample after the sufficient annealing although it has been reconstructed from the original large hole Fermi surface centered at (π, π) to the small electron Fermi surface centered at (0, π), probably due to AF order [46–48, 50, 51] [Fig. 5.2]. The same reconstruction occurs for the other samples, except for the annealed $x = 0.10$ sample, which shows a large hole Fermi surface free from the reconstruction, suggesting suppression of the AF order or AF fluctuations in this sample, as our ARPES study previously reported [93].

The strength of the AF order or AF fluctuations can be evaluated from the magnitude of the AF band splitting, $2\Delta_{\mathrm{AF}}$. Around the node, the upper band of the antiferromagnetically split bands resides above the Fermi energy (E_{F}), and hence the E_{F} lies within the AF gap. In moving away from the node and approaching the antinode, the upper band is lowered, crosses E_{F}, and produces finite spectral intensity below E_{F}. Then the $2\Delta_{\mathrm{AF}}$ can be determined from the energy separation between the upper and lower band (See chapter 6 for more details). In Figs. 5.2(b1)-(b6), EDCs at several k_{F} points from the node to antinode are plotted with estimated $2\Delta_{\mathrm{AF}}$ values for each sample. Comparing the as-grown and annealed samples with the sample Ce concentration, annealing dramatically reduces the $2\Delta_{\mathrm{AF}}$ both for the $x = 0.05$ and $x = 0.10$ samples, indicating the weakening of the AF correlation by annealing. (Although the AF pseudogap was not visible in the previous our study on protect-annealed PLCCO ($x = 0.10$) sin-

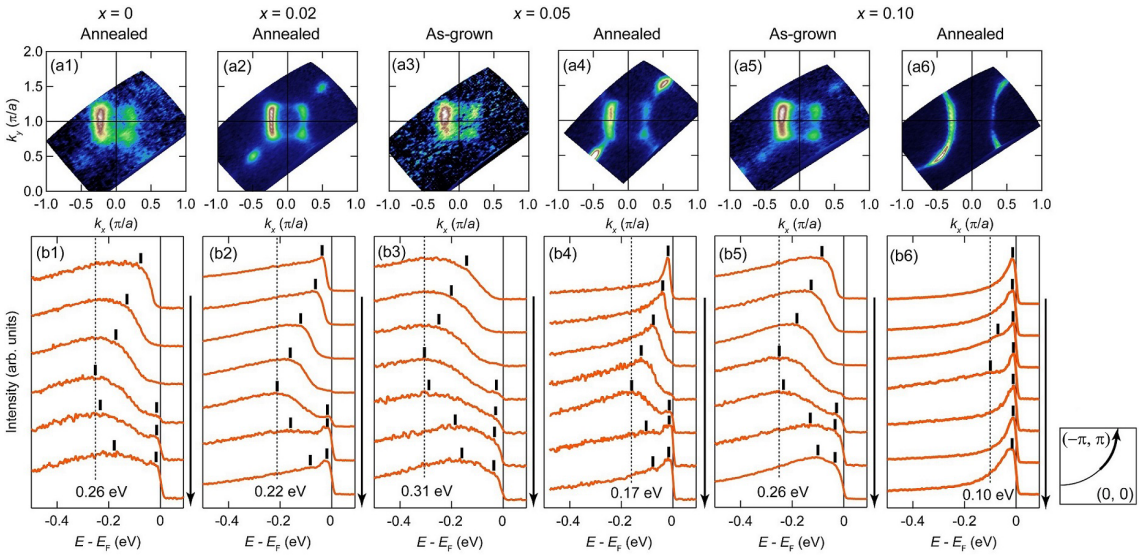

Figure 5.2: ARPES spectra of PLCCO samples. (a1-a6) Fermi surface mapping obtained by integrating spectral intensity within the energy of $E_F \pm 20$ meV. (b1-b6) EDCs at several k_F points from the nodal to antinodal region. Peak positions are indicated by vertical bars. The $2\Delta_{AF}$ estimated from the separation between the lower and upper bands is shown in each panel.

gle crystals [93], we observed a weak signature of the AF pseudogap in the present annealed $x = 0.10$ sample, possibly due to a subtle difference in the annealing condition beyond control.)

In order to clarify if the weakening of the AF correlation is an inherent effect of annealing or is simply due to electron doping, we first estimated the electron concentration n_{FS} from the area of the Fermi surface assuming Luttinger's theorem. For the determination of the Fermi surface, k_F positions were estimated from the peak positions in momentum distribution curves (MDCs) integrated within the energy range of $E_F \pm 10$ meV and plotted in Figs. 5.3(a)-(f). For antiferromagnetically reconstructed Fermi surfaces, that is, except for the Fermi surface of annealed $x = 0.10$ sample, k_F positions were fitted to the curve of $|k_x/r|^\alpha + |k_y/r|^\alpha = 1$, which was found to show good agreement with the experimental data. The Fermi surface of annealed $x = 0.10$ sample was well reproduced by the simple tight-binding model,

$$\begin{aligned}\epsilon - \mu =& \epsilon_0 - 2t(\cos\, k_x a + \cos\, k_y a) \\ & - 4t' \cos\, k_x a \cos\, k_y a - 2t"(\cos\, 2k_x a + \cos\, 2k_y a),\end{aligned} \tag{5.1}$$

where t, t', and t" are transfer integrals between the nearest-neighbor, second-nearest-neighbor, and third-nearest-neighbor Cu sites, respectively. By calculating

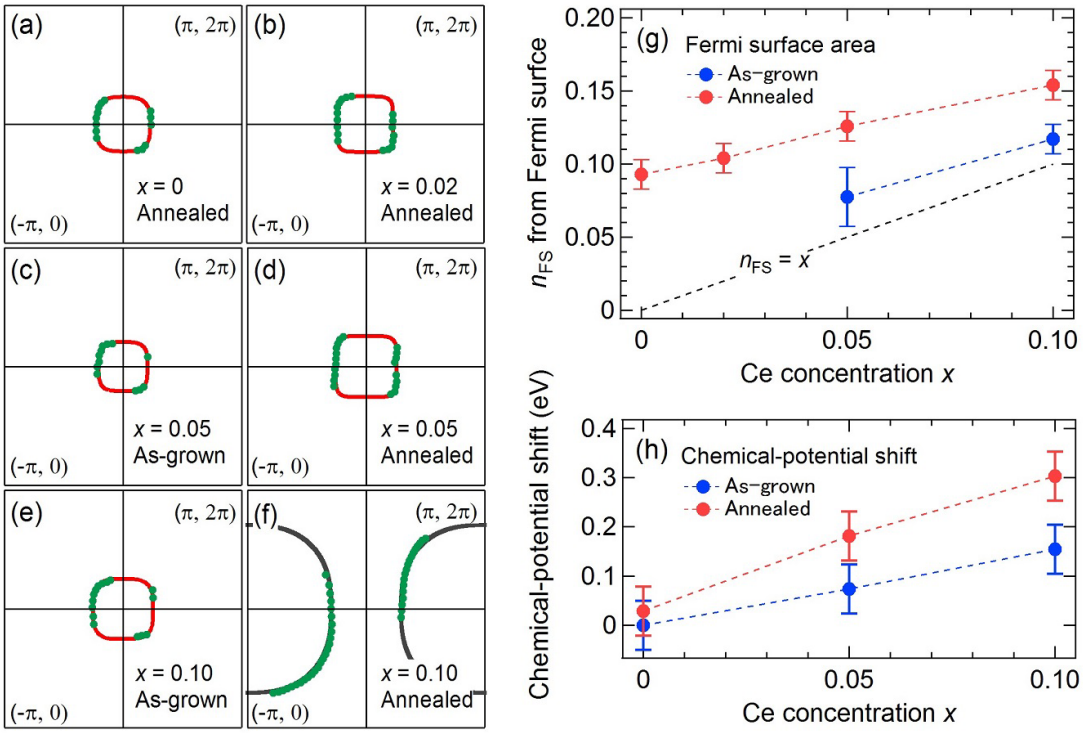

Figure 5.3: Electron concentration of PLCCO samples. (a)-(f) Peak positions of MDCs integrated within the energy range of $E_F \pm 10$ meV (green dots). The peak positions in (a)-(e) are fitted to the curve of $|k_x/r|^\alpha + |k_y/r|^\alpha = 1$ (red curve), whereas those in (f) are fitted to the paramagenetic tight-binding model. (g) Electron concentration n_{FS} estimated from the area of the fitted Fermi surface plotted against Ce concentration x. The black dashed line represents $n_{FS} = x$. (h) Chemical-potential shifts estimated from the shifts of the La $3d$, Pr $3d$, and O $1s$ core-level peaks measured by XPS, and plotted against Ce concentration x.

the area of the fitted Fermi surfaces, we estimated the electron concentration n_{FS} for each sample and plotted it against Ce concentration x in Fig, 5.3(g). While the n_{FS}'s of the as-grown samples are close to the Ce concentration (deviation is only 0.02-0.03), those of the annealed samples are larger than the Ce concentration by 0.05-0.09, suggesting that the samples were doped with excess electrons by protect annealing under strongly reducing condition. The positions of the chemical potential, which was estimated from the positions of the La, Pr, and O core-level peaks measured by XPS, was also found to shift upwards by annealing for the $x = 0.05$ and $x = 0.10$ samples, consistent with the electron doping by annealing, although the chemical-potential shift observed for the annealed $x = 0$ was somewhat small compared to the area of the Fermi surface and the reason is unclear at present.

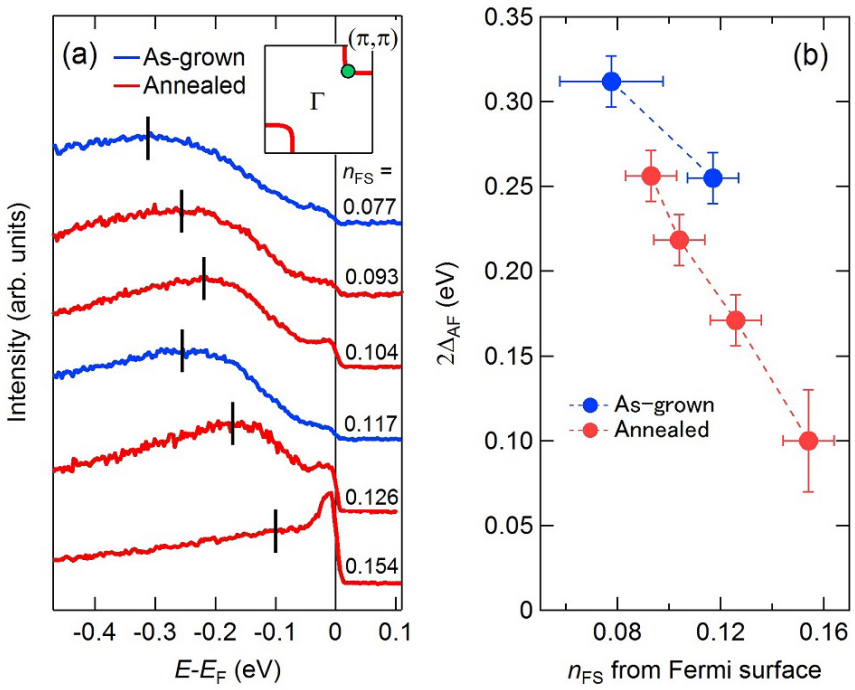

Figure 5.4: Magnitude of AF band splitting versus electron concentration for the as-grown and annealed PLCCO. (a) EDCs at the momentum position indicated in the inset plotted in the order of n_{FS} from top to bottom. Peak positions are indicated by vertical bars. (b) Magnitude of the AF band splitting $2\Delta_{AF}$ plotted against n_{FS}.

Having evaluated the electron concentration for each sample, we examine its relevance to AF correlation. In Fig. 5.4(a), EDC at the momentum position where the bottom of the upper AF band touches E_F is plotted for each sample in the order of n_{FS} from top to bottom. As mentioned above, $2\Delta_{AF}$ can be evaluated from the peak separation between the lower and upper AF band, which corresponds to the binding energy of the lower-band peak in the EDCs plotted in Fig. 5.4(a). The lower-band peak position does not depend monotonically on n_{FS} because $2\Delta_{AF}$ of the as-grown $x = 0.10$ sample with $n_{FS} = 0.117$ is larger than that of the annealed $x = 0.02$ sample with smaller n_{FS} ($= 0.104$), and almost the same with that of the annealed $x = 0$ sample with even smaller n_{FS} ($= 0.093$). Therefore, as summarized in Fig. 5.4(b), one can conclude that the increase of electron concentration weakens the AF correlation but that annealing, thereby removing excess oxygen atoms, further weakens the AF correlation in addition to the electron doping.

The effect of annealing was also observed in the ARPES spectra recorded in the antinodal region. Figure 5.5(a) shows EDCs taken at the antinode and normalized

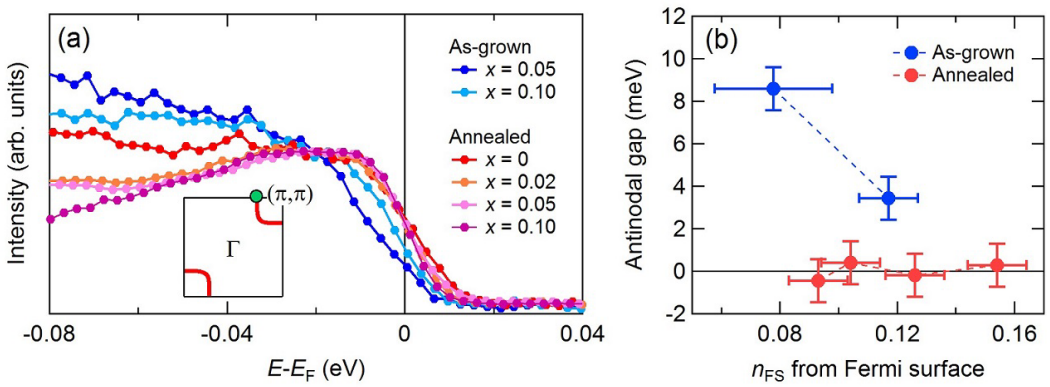

Figure 5.5: Antinodal gap observed for the as-grown PLCCO samples. (a) EDCs taken at the antinode, which is indicated in the inset, and normalized to the height of the lowest energy peak. (b) The shift of the leading-edge midpoint estimated from (a) and plotted against n_{FS}.

to the peak height. For the as-grown samples with $x = 0.05$ and 0.10, a small gap is observed whereas annealed samples do not show a gap irrespective of the Ce concentration. The magnitude of the gap is 4-8 meV, which is much smaller than the energy scale of the AF band splitting (a few hundreds meV). Since this gap is not related to n_{FS} as shown in Fig. 5.5(b), it should be characteristic of as-grown samples. The gap observed at the antinode, where the bands should cross E_{F} regardless of the presence of AF band reconstruction, suggests the gap opening on the entire Fermi surface, which is consistent with the divergence of resistivity seen in the as-grown samples (Fig. 5.1). Considering the fact that the quasi-particle peak is suppressed for the as-grown samples [Fig. 5.5(a)], as-grown samples may contain a large amount of disorder which leads to the opening of Coulomb gap [132], and the gap is closed by annealing.

Thus, we have revealed that an important role of annealing other than electron doping is to weaken the AF band splitting and eliminate the Coulomb gap. Since we have excluded the influence of the electron concentration, not only the opening of the Coulomb gap but also the enhancement of the AF band splitting in the as-grown samples probably originated from disorder. In the as-grown samples, the disorder of the electrostatic potential would localize carriers, resulting in the development of local AF correlation around the disorder [90, 133]. Increase of the disorder may make the AF correlation more long-ranged and/or increase the magnitude of the local magnetic moment, enhancing the AF band splitting. The most plausible candidate for the disorder is excess oxygen atoms at the apical site since it has long been believed that those apical oxygen atoms are removed by annealing [24]. The more strongly the sample is annealed, the more thoroughly

the disorder is removed, but at the same time, oxygen atoms at the regular site also diffuse out, leading to electron doping as observed in the present study as well as in the previous ARPES studies [93, 100]. While sufficiently annealed thin films of the parent compound Pr_2CuO_4 shows superconductivity with $n_{FS} = 0.170$ as revealed in chapter 3, the present bulk protect-annealed PLCCO ($x = 0$) single crystals with $n_{FS} = 0.093$ does not show superconductivity. Bulk single crystals of the parent compound would also be SC if one could anneal the sample more thoroughly and increase n_{FS}.

5.4 conclusion

In conclusion, we have performed ARPES and core-level XPS measurements on $Pr_{1.3-x}La_{0.7}Ce_xCuO_4$ with varying Ce concentration and annealing conditions. Electron concentration n_{FS} estimated from Fermi surface area are strongly deviated from Ce concentration x (by 0.05-0.09), indicating that electrons are doped by annealing. This was also supported by the chemical-potential shift deduced from core-level XPS measurements. By comparing the electron-concentration dependence of the electronic structure between as-grown and protect-annealed samples, we have revealed that an important role of annealing other than electron-doping is to remove disorder which localizes electrons, produces the Coulomb gap, and increases the AF correlation.

Chapter 6

Nature of the antiferromagnetic gap in the electron-doped cuprates $\mathbf{Pr}_{1.3-x}\mathbf{La}_{0.7}\mathbf{Ce}_x\mathbf{CuO}_4$

6.1 Introduction

Physical properties of electron-doped cuprates are rather dominated by antiferromagnetism, and a gap opening or the suppression of spectral intensity at the hot spot, where the Fermi surface and the antiferromagnetic (AF) Brillouin zone (BZ) boundary cross with each other, has been widely observed in the electron-doped cuprates by angle-resolved photoemission spectroscopy (ARPES) [45–51]. The overall band structure is basically consistent with a tight-binding model of the square lattice consisting of the Cu $3d_{x^2-y^2}$ orbitals with the $\sqrt{2}\times\sqrt{2}$ AF order,

$$\begin{aligned}\epsilon - \mu =& \epsilon_0 \pm \sqrt{\Delta_{AF}^2 + 4t^2(\cos\, k_x a + \cos\, k_y a)^2} \\ & - 4t' \cos\, k_x a\, \cos\, k_y a - 2t"(\cos\, 2k_x a + \cos\, 2k_y a),\end{aligned} \tag{6.1}$$

where t, t', and t" are transfer integrals between the nearest-neighbor, second-nearest-neighbor, and third-nearest-neighbor Cu sites, respectively. $2\Delta_{\mathrm{AF}}$ represents the potential deference between the two spin sublattices. However, an ARPES study by Matsui *et al.* [46] has shown that the magnitude of the band splitting decreases with approaching antinodal region. Ikeda *et al.* [50] have also concluded from the observed band structure in their ARPES study that Δ_{AF} becomes zero around $(0, \pi)$ and $(\pi, 0)$. On the other hand, Park *et al.* [47] have claimed that Δ_{AF} is actually constant throughout the momentum space, but is just apparently reduced due to the presence of a paramagnetic band disperses uninterrupted through the AF BZ boundary because antiferromagnetism is inhomogeneous and short-ranged. The nontrivial AF band splitting in momentum space should contain

important information about the AF correlation in electron-doped cuprates, but whether $\Delta_{\rm AF}$ is momentum dependent or not has not been fully clarified yet.

In the present chapter, we report an ARPES study of the AF electron-doped cuprates $Pr_{1.3-x}La_{0.7}Ce_xCuO_4$ (PLCCO, $x = 0.02$) which was protect-annealed under strongly reducing condition to effectively remove excess oxygen [90]. We have closely investigated the band structure along various directions in much wider momentum region than in the previous studies, and found that the AF gap is actually highly anisotropic in momentum space. The observed features are not specific to the protect-annealed samples, but should be common to the AF electron-doped cuprates, and advance our understanding of the AF correlation in the electron-doped cuprates.

6.2 Experimental

We have performed an ARPES measurement of a protect-annealed $Pr_{1.3-x}La_{0.7}Ce_xCuO_4$ (PLCCO, $x = 0.02$) single crystal. Sample properties and experimental conditions are described in section 5.2.

6.3 Results and discussion

Figure 6.1 shows Fermi surface and band images of a protect-annealed PLCCO ($x = 0.02$) sample. The band is gapped at the node (#1), and the gap increases in going from the node to the hot spot (#2). On approaching the antinode, the upper part of the split band is lowered below the Fermi level ($E_{\rm F}$) and produces finite spectral intensity below $E_{\rm F}$, forming an electron-like Fermi surface around $(0, \pi)$. These features are characteristic of the AF electron-doped cuprates and have been reported in many previous studies [46–51].

Now we look into more detailed features of the band structure. As is seen in Fig. 6.1(c1) and (c2), at the node and the hot spot, as the band disperses from higher binding energy toward $E_{\rm F}$, it disperses back to higher binding energy beyond the AF BZ boundary, as expected for the $\sqrt{2} \times \sqrt{2}$ AF order. Once the upper band is lowered below $E_{\rm F}$, however, the lower band is no longer folded and disperses straightly across the AF BZ boundary ((c3)-(c5)), suggesting a change in the band character. On the other hand, although the upper band is folded along cut #4, along cut #5 upper band merges with the lower band before reaching the AF BZ boudary. Part of the results, such as the absence of the folding in the lower band around the antinode, has been reproduced by considering the short-range AF order [47, 105], but the momentum anisotropy of the band folding cannot be reproduced by those models. Furthermore, the present sample is in long-range AF

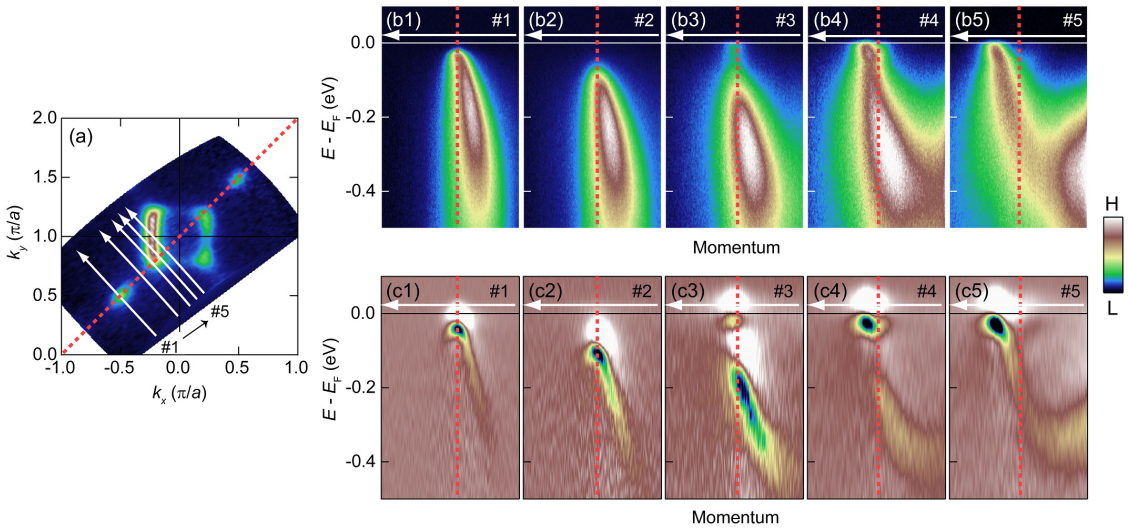

Figure 6.1: ARPES spectra of a protect-annealed PLCCO ($x = 0.02$) single crystal. (a) Fermi surface mapping. Spectral intensity integrated within ±20 meV of E_F is plotted. (b1)-(b5) Band images taken along the cuts indicated in (a). The AF BZ boundary is shown by a dashed red line in each panel. (c1)-(c5) Corresponding second derivatives with respect to energy.

order at the measurement temperature of 10 K ($< T_N = 85$ K), and hence the short-range AF model is not suitable.

The most effective method to reveal the overall momentum dependence of the AF band splitting is to observe the band dispersion along the AF BZ boundary. Since the splitting between the upper and lower bands should be constant ($= 2\Delta_{AF}$) along the AF BZ boundary within the simple tight-binding model with the $\sqrt{2} \times \sqrt{2}$ AF order (Eq. (6.1)), the observation of the momentum dependence is quite non-trivial. The experimentally obtained band image along the AF BZ boundary and its second derivative with respect to energy are shown in Fig. 6.2(a) and (b), respectively. Starting from (-π/2, 3π/2), the peak positions in energy distribution curves (EDCs) superimposed on Fig. 6.2(a) is smoothly shifted toward higher binding energy, but once the spectral intensity of the upper band emerges below E_F, the lower band shows a kink and the peak position moves upwards. Further approaching (0, π), the upper band suddenly loses its intensity, and the lower band starts to disperse downwards, reaching a minimum at (0, π). This nonmonotonic band structure can also be confirmed in the second-derivative plot in Fig. 6.2(b). The momentum position where the lower band shows the kink, i.e., around the k_F of the upper band, corresponds to the momentum position where the band folding become obscured as shown in Fig. 6.1(c3). This suggests that the band around (-π/2, 3π/2) is the antiferromagenetically split band, and the lower

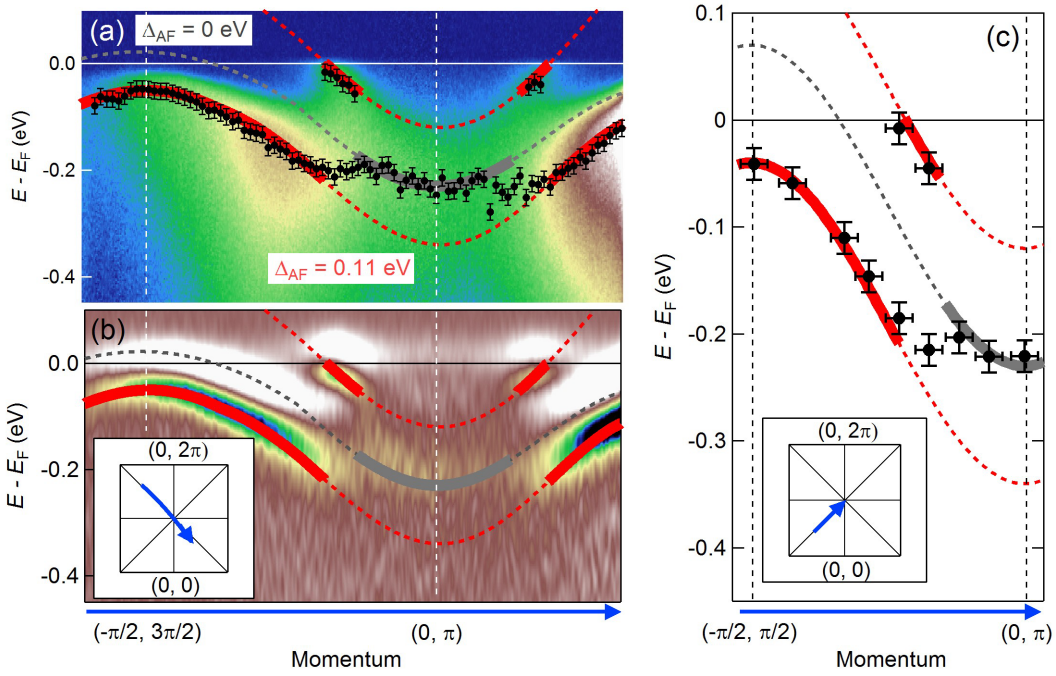

Figure 6.2: AF band splitting along the AF BZ boundary. (a),(b) Band image and its second derivative with respect to energy along the cut indicated in the inset of (b). Peak positions of the EDCs are plotted as black dots in (a). Band dispersion fitted to the tight-binding model with the $\sqrt{2} \times \sqrt{2}$ AF order ($t = 0.25$ eV, $t'/t = -0.15$, $t''/t' = -0.5$, $\epsilon_0/t = -0.02$) with $\Delta_{AF} = 0.11$ eV (red curve) and $\Delta_{AF} = 0$ eV (black curve) is also plotted. The fitted band is represented by solid curves in the region relevant to the fitting, and by dashed curves in the other region. The inset in (b) shows the experimentally obtained Fermi surface and the Fermi surface calculated using the tight-binding model with $\Delta_{AF} = 0.11$ eV (red curve). (c) Peak positions of EDCs plotted from (-π/2, π/2) to (0, π) extracted from the measurements along several cuts parallel to (0, 0)-(-π, π) direction. Band dispersion calculated by the tight-binding model using the parameters derived from the fitting is superimposed.

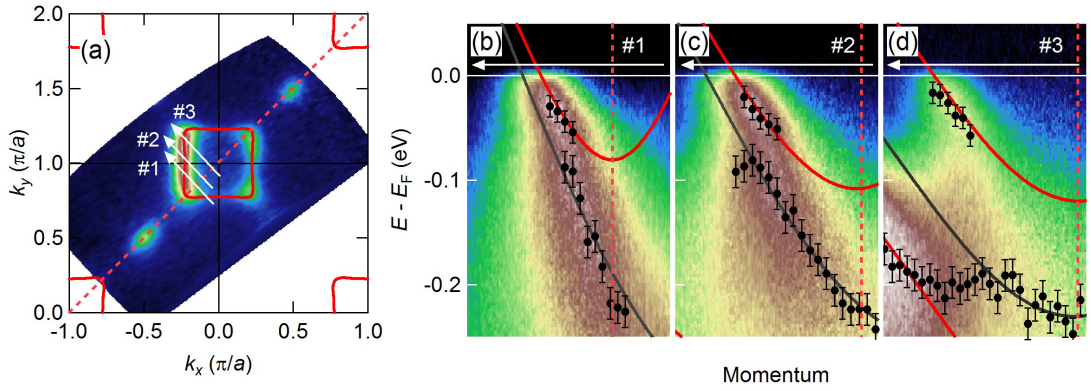

Figure 6.3: Low-energy band structure near (0, π). (a) Fermi surface mapping with the Fermi surface contour reproduced from the tight binding model with $\Delta_{AF} = 0.11$ eV. (b-d) Band images along cuts #1-#3 indicated in the inset of (a), respectively. Peak positions of the EDCs are plotted as black dots. The bands calculated using the tight-binding model with $\Delta_{AF} = 0.11$ eV (red curve) and $\Delta_{AF} = 0$ eV (black curve) are also plotted.

band around (0, π) is the paramagnetic band ($\Delta_{AF} = 0$). Based on this picture, the band structure along the AFBZ boundary was fitted to the tight-binding model with finite Δ_{AF} around (-π/2, 3π/2) and with $\Delta_{AF} = 0$ around (0, π) keeping the hopping parameters and ϵ_0 the same for both cases. The bands obtained with the fitted parameters of $t = 0.25$ eV, $t'/t = -0.15$, $t''/t' = -0.5$, $\epsilon_0/t = -0.02$, and $\Delta_{AF} = 0.11$ eV or $\Delta_{AF} = 0$ eV are plotted in Fig. 6.2(a) and (b) as solid curves in the region relevant to the fitting, and as dashed curves in the other region. The fitted bands show excellent agreement with the experimental bands. In order to exclude the possibility that the effect of photoionization matrix elements has prevented the precise evaluation of the band positions, we have also examined the band structure along the AF BZ boundary in different direction, from (-π/2, π/2) to (0, π). For that purpose, peak positions of the EDCs at the AF BZ boundary have been extracted from the measurements along several cuts parallel to (0, 0)-(-π, π) direction, and plotted in Fig. 6.2(c) together with the bands reproduced by the tight-binding model using the parameters obtained by the above fitting procedure. The EDCs' peak positions are again in good agreement with the tight-binding model, confirming the validity of the present analysis.

We now examine the sudden disappearance of the AF upper band and the jump of the AF lower band more closely. As shown in Figs. 6.3(b)-(d), not only along the cut parallel to the AF BZ boundary (#3) as also shown in Fig.6.2 but also along the cuts near the antinode (#1,#2), a jump was observed in EDCs' peak at the binding energy of $\sim$ 50 meV although the magnitude of the jump

depended on the cut position. All of these jumps, including their magnitude, can be reproduced by the combination of the antiferromagnetically split bands and the paramagnetic band as presented in Figs. 6.3(b)-(d). The relatively small size of the jump near the antinode is because the separation between the paramagnetic band and the upper AF band is smaller in the antinodal region. This agreement in all of the cuts strongly suggests that the AF gap $\Delta_{\rm AF}$ indeed collapses to zero around (0, π) in all the directions. Considering the fact that the AF upper band disappears always at $\sim$ 50 meV below $E_{\rm F}$ [Figs. 6.3(b)-(d)], it may be the binding energy of the AF upper band rather than the momentum position which triggers the collapse of $\Delta_{\rm AF}$. The present conclusion is consistent with the claim in the previous ARPES study by Ikeda *et al* [50] that the band dispersing around (0, π) is the paramagnetic band. While most of the previous theoretical studies, with weak-coupling [134] nor with strong-coupling treatment [135], have not explicitly shown the anisotropy of the AF gap, a variational Monte Carlo study by Chou and Lee [52] have shown that the $\Delta_{\rm AF}$ have a maximum value at (π/2, π/2) and have a minimum value at (0, π), qualitatively consistent with the present study, suggesting that the observed anisotropy of $\Delta_{\rm AF}$ originates from the effect of strong correlation. More detailed variational Monte Carlo studies are desired because Chou and Lee showed the result of the calculation only at five momentum points between (π/2, π/2) and (0, π), and hence it is not clear if $\Delta_{\rm AF}$ shows an abrupt change in momentum space as observed in the present study.

Since the AF upper band is consistent with the tight-binding model from $E_{\rm F}$ to $\sim$ 50 meV below it, the Fermi surface is well described by the tight-binding model. The antiferromagnetically reconstructed Fermi surface calculated using the same parameter obtained by fitting the band structure shows good agreement with the experimental one as shown in Fig. 6.3(a). The electron concentration $n_{\rm FS}$ estimated from the area of the fitted Fermi surface is 0.104, by far larger than the nominal Ce concentration $x = 0.02$. This deviation could be due to oxygen deficiency introduced by protect annealing under a strongly reducing condition. Similar deviation has also been seen in our recent ARPES study of protect-annealed PLCCO ($x = 0.10$) single crystals [93] as well as in the previous ARPES study on T'-type La_2CuO4 thin films [100], and has been attributed to oxygen non-stoichiometry.

6.4 Conclusion

In conclusion, we have carried out an ARPES measurement on the protect-annealed electron-doped cuprate PLCCO ($x = 0.02$) and investigated the nature of the AF gap. By closely examining the band structure in the wide momentum range, we have revealed that the magnitude of the AF band splitting $\Delta_{\rm AF}$ is

constant outside the antiferromagnetically reconstructed Fermi surface centered at $(0, \pi)$, but is zero inside the constant energy ($\sim$ 50 meV binding energy) surface. The momentum anisotropy is qualitatively consistent with the previous variational Monte-Carlo study by Chou and Lee [52] in the sense that Δ_{AF} is momentum-dependent and shows the minimum value at $(0, \pi)$, suggesting that the anisotropy arises from the effect of strong correlation.

Chapter 7

Superconducting gap of protect-annealed $Pr_{1.3-x}La_{0.7}Ce_xCuO_4$ single crystals

7.1 Introduction

The symmetry of the superconducting (SC) gap provides a strong clue for the origin of unconventional superconductivity and has been intensively studied on electron-doped cuprate superconductors. Raman scattering [68] and angle-resolved photoemission spectroscopy (ARPES) [69] studies have revealed that the SC gap does not only exhibit simple $d_{x^2-y^2}$-wave momentum dependence but also shows a maximum near the hot spot, where antiferromagnetic (AF) Brillouin zone boundary and Fermi surface cross, and large contribution of AF spin fluctuations to the superconductivity have been proposed. The scenario of superconductivity mediated by AF spin fluctuations in the T'-type cuprates appears quite plausible since the superconductivity emerges by doping electrons into the AF Mott insulating parent compound.

Our recent ARPES study on protect-annealed PLCCO ($x = 0.10$) has revealed strong suppression of the hot spot, namely, the AF pseudogap, suggesting a dramatic reduction of the AF spin correlation length and/or the magnitude of the magnetic moments [93]. In order to investigate the nature of the SC state with high T_c and suppressed AF correlation, we have performed ARPES measurements on protect-annealed PLCCO ($x = 0.10, 0.15$) single crystals and directly observed momentum-dependent SC gap.

7.2 Experimental

Single crystals of PLCCO with $x = 0.10$ (samples #1-#4) and 0.15 (samples #5, and #6) were synthesized by the traveling-solvent floating-zone method and were protect-annealed for 24 hours at 800 °C. After the annealing, samples with $x = 0.10$ and $x = 0.15$ showed T_c values of 27 K and 22 K, respectively. Most of the ARPES measurements were performed at beamline 7U of UVSOR facility (samples #1-#3, #5, and #6). At UVSOR, linearly polarized light with $h\nu = 16.5$ eV was used for the measurements. The total energy resolution was set at 8 meV. Sample #3 was measured three times while each of the other samples was measured once. Prior to each measurement, the sample was cleaved *in situ* under the pressure better than 1×10^{-10} Torr. Considering relatively quick surface degradation which is typical for T'-type cuprates [66], ARPES spectra were recorded within 4 hours after cleavage at only one momentum position at two temperatures below and above T_c for each sample. Just before or after taking every single spectrum of the sample, a gold film evaporated near the sample was measured to determine the Fermi level (E_F) of the sample at that moment. Sample #4 was measured using a laser-ARPES apparatus developed at ISSP with the 7 eV quasi-CW laser (repetition rate = 240 MHz). The total energy resolution was set at 1.5 meV. The measurement was carried out under the vacuum better than 4×10^{-11} Torr.

7.3 Results and discussion

Figure 7.1(a) shows energy distribution curves (EDCs) of PLCCO ($x = 0.10$) measured with $h\nu = 16.5$ eV photons at the Fermi wave vector (k_F) near ($\pi/2$, $\pi/2$) and (0.3π, π), which correspond to nodal and antinodal points, respectively, in the case of $d_{x^2-y^2}$-wave paring. Since the T'-type cuprates does not show clear SC coherence peaks in their ARPES spectra [66, 67, 69] and the position of the leading-edge midpoint at $T < T_c$ referenced to E_F does not necessarily reflect the magnitude of the SC gap [67], we compared the spectra taken above and below T_c and estimated the magnitude of the leading-edge shift Δ_{shift} caused by the opening of SC gap as shown in Fig. 7.1(a). EDCs near ($\pi/2$, $\pi/2$) taken above and below T_c cross almost at E_F and Δ_{shift} is as small as 0.3 meV, whereas those near (0.3π, π) cross recognizably below E_F and a leading-edge shift of 1.3 meV was observed. This leading-edge shift near (0.3π, π) was also observed by similar amounts in the measurements on another $x = 0.10$ sample reproducibly as shown in Fig. 7.1(b), suggesting the SC gap opening near (0.3π, π). The momentum region near (0.3π, π) cannot be reached in the ARPES measurement using 7 eV laser due to the low photon energy, but the laser-ARPES spectra also show finite Δ_{shift} between (0.3π, π) and ($\pi/2$, $\pi/2$), and negligibly small Δ_{shift} near ($\pi/2$, $\pi/2$) [Fig. 7.1(c)]. The same tendency is also observed in the $x = 0.15$ samples [Fig. 7.1(d)], although

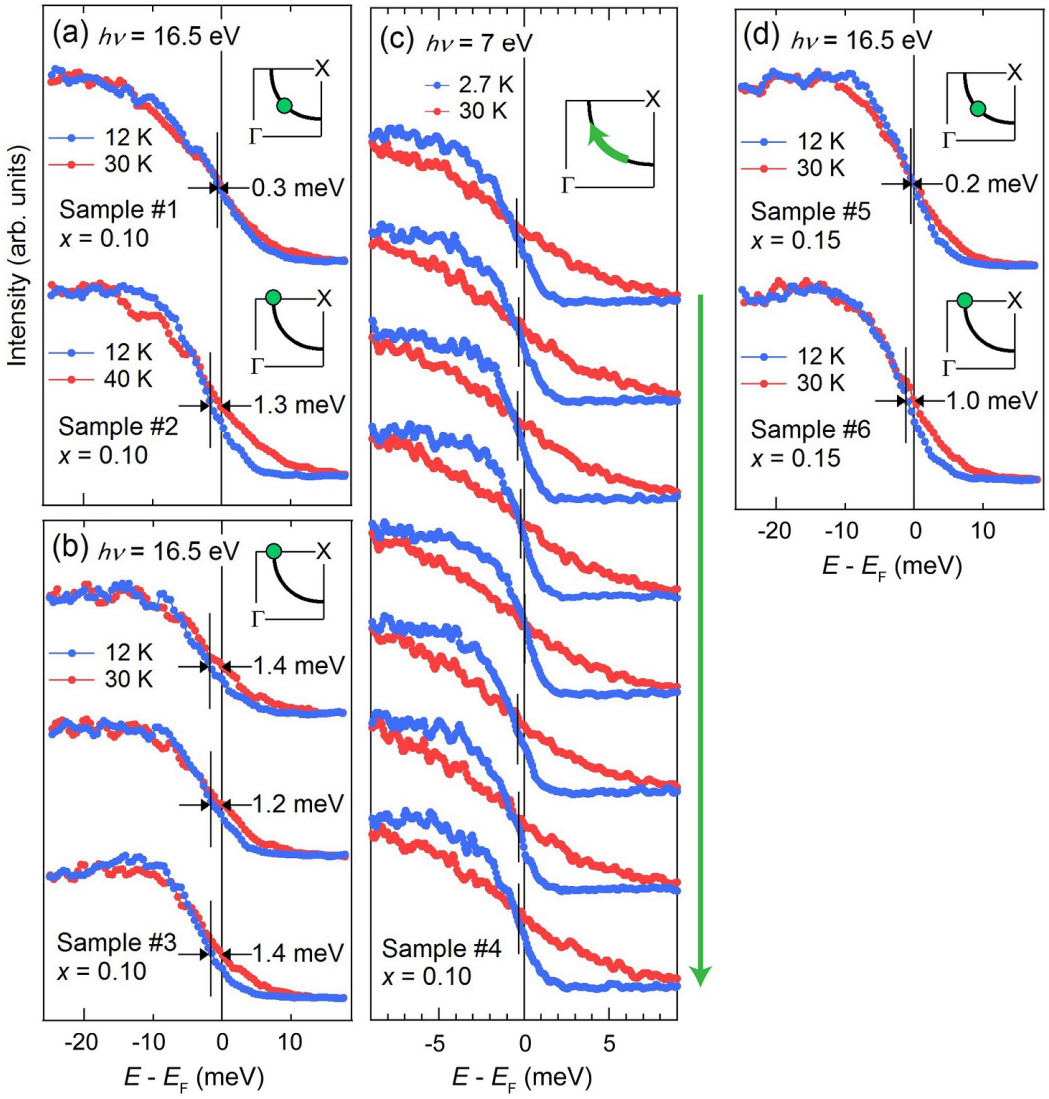

Figure 7.1: Leading-edge shift observed in PLCCO samples. EDCs of (a) samples #1 and #2 with $x = 0.10$, (b) sample #3 with $x = 0.10$, (c) sample #4 with $x = 0.10$, and (d) #5 and #6 with $x = 0.15$ measured at temperatures above (red curves) and below (blue curves) T_c. Insets indicate the k_F positions where the EDCs were measured. Estimated Δ_{shift} values are shown beside each set of the EDCs.

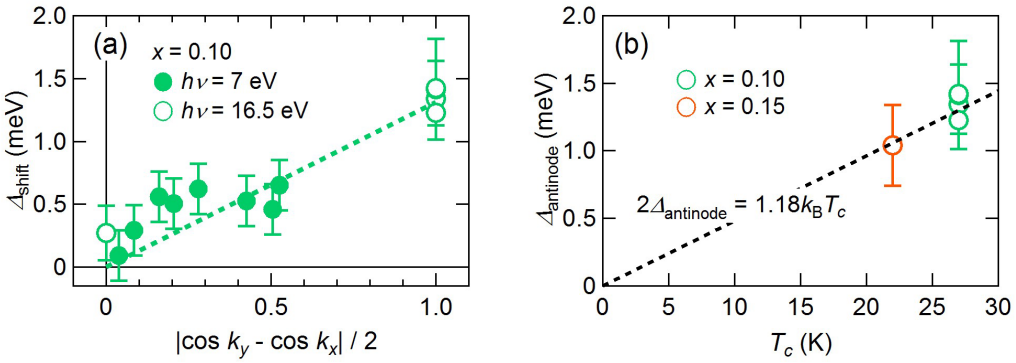

Figure 7.2: $d_{x^2-y^2}$-wave-like SC gap of PLCCO. (a) Leading-edge shift $\Delta_{\rm shift}$ plotted against the d-wave order parameter $|{\rm cos}k_x - {\rm cos}k_y|/2$. The error bar for the synchrotron data was defined as half the size of the change in $E_{\rm F}$ of the reference gold during the sample measurement. A line obtained by fitting $x = 0.10$ data is also plotted. (b) $\Delta_{\rm shift}$ at $(0.3\pi, \pi)$, $\Delta_{\rm antinode}$, plotted against T_c values. A line representing $2\Delta_{\rm antinode} = 1.18k_{\rm B}T_c$, which was obtained by fitting the data assuming that $\Delta_{\rm antinode}$ is proportional to $k_{\rm B}T_c$, is superimposed.

$\Delta_{\rm shift}$ near $(0.3\pi, \pi)$ was slightly smaller than those of the $x = 0.10$ samples.

The $\Delta_{\rm shift}$ values estimated from Fig. 7.1 are plotted against the d-wave order parameter $|{\rm cos}k_x - {\rm cos}k_y|/2$ in Fig. 7.2(a). Tiny but finite drift of the incident photon energy during the measurement at UVSOR, which affects the kinetic energy of the photoelectrons, was evaluated from the change of $E_{\rm F}$ of the reference gold film, and indicated by an error bar (The error bar was defined as half of changes in $E_{\rm F}$ of the reference gold during the sample measurement.). The error bars for the laser-ARPES data were assumed to be constant. The $\Delta_{\rm shift}$ for the $x = 0.10$ samples is roughly proportional to the d-wave order parameter, supporting the monotonic $d_{x^2-y^2}$-wave symmetry of the SC gap rather than the nonmonotonic $d_{x^2-y^2}$-wave reported previously [68, 69]. For that discussion, however, more thorough investigation of the momentum dependence of the SC gap is required. At present, we just conclude that the observed SC gap is consistent with $d_{x^2-y^2}$-wave symmetry. In Fig. 7.2(b), $\Delta_{\rm shift}$ at $\sim (0.3\pi, \pi)$ is plotted as $\Delta_{\rm antinode}$ against T_c. The dependence of $\Delta_{\rm antinode}$ on T_c was satisfactorily fitted to the equation of $\Delta_{\rm antinode} = \alpha k_{\rm B}T_c$, suggesting that the superconducting states of $x = 0.10$ and $x = 0.15$ samples are in the same $d_{x^2-y^2}$-wave-like symmetry and are realized by the same mechanism, although obtained value of $\alpha = 1.18$ is somewhat smaller than $\alpha = 1.70$ derived in the previous ARPES study on $Pr_{1-x}LaCe_xCuO_4$ ($x = 0.11$) [69] and the reason is not clear at the moment.

The present result suggests that $d_{x^2-y^2}$-paring, which is associated with AF spin fluctuations, persists after the strong reduction of AF correlation length and/or

magnitude of the local magnetic moment by protect annealing. Studies on protect-annealed PLCCO samples using muon spin relaxation [133] or NMR [136], which are sensitive to spins, have revealed the development of AF spin susceptibility with decreasing temperature and short-ranged AF order setting in at low temperature, while the long-range AF order was suppressed. These results have been explained within a model which regards T'-type cuprates as in antiferromagnetically correlated state with an AF order induced around excess apical oxygen atoms [90, 133]: The presence of apical oxygen atoms leads to long-range AF order in as-grown samples, and the order becomes short-ranged by removing part of the apical oxygen atoms by annealing. Considering that the more effective removal of the apical oxygen by protect annealing resulted in higher T_c than that had been obtained in a previous study [91], the short-range AF order induced around apical oxygen atoms is harmful for superconductivity, but AF correlation itself may survive in the $d_{x^2-y^2}$-wave SC state of the T'-type cuprates.

7.4 Conclusion

In conclusion, we have performed ARPES measurements on protect-annealed PLCCO single crystals ($x = 0.10, 0.15$) and estimated Δ_{shift} as a measure of the SC gap. Observed momentum dependence of Δ_{shift} was consistent with $d_{x^2-y^2}$-wave symmetry, suggesting that superconductivity in T'-type cuprate is mediated by AF spin fluctuations regardless of the doping level even after the strong reduction of AF spin correlation length and/or the magnitude of the magnetic moment by protect annealing.

Chapter 8

Summary and conclusion

In the present thesis, we have presented photoemission studies of new electron-doped cuprate superconductors which exhibits superconductivity at very low or even zero Ce doping. The key to achieve superconductivity was post-growth annealing under reducing conditions in order to remove excess oxygen atoms. Therefore, we investigated the electric structure of those new electron-doped cuprates with special emphasis on the effect of annealing on the electronic structure.

In chapter 3, we have prepared thin films of superconducting (SC) parent compound Pr_2CuO_4 and studied them by angle-resolved photoemission spectroscopy (ARPES). For the surface sensitive ARPES measurements, we have synthesized SC Pr_2CuO_4 by growing it under highly reducing conditions, which may have a similar effect to the post-growth annealing under a reducing condition. Clear Fermi surfaces were observed whose area suggested the electron concentration $n_{\rm FS}$ of 0.170, which is considerably deviated from half-filling and corresponding to overdoping for Ce-doped conventional superconductors. In chapter 4, the SC parent compound Nd_2CuO_4 and related materials were studied by relatively bulk sensitive hard X-ray photoemission spectroscopy (HAXPES) and X-ray absorption spectroscopy (XAS). We have observed a chemical-potential shift of ~ 0.2 eV between the insulating and SC Nd_2CuO_4. From comparison with the chemical-potential shift previously reported for $Nd_{2-x}Ce_xCuO_4$, we have concluded that SC Nd_2CuO_4 is doped with excess electrons of 0.149 per Cu, which is close to the value obtained in the ARPES study in chapter 3. Thus, the present SC parent compounds were found to be electron-doped and not at half filling.

In chapter 5, we have performed a systematic ARPES study on protect-annealed underdoped $Pr_{1.3-x}La_{0.7}Ce_xCuO_4$ single crystals with varying Ce concentration and annealing condition, and revealed three kinds of annealing effects on the electronic structure. It was found that protect annealing under highly reducing condition leads to the doping of 0.05-0.09 electrons per Cu. By comparing the electron-concentration dependence of the electronic structure between as-grown and protect-

annealed samples, we have revealed that important roles of annealing other than electron doping is to remove the Coulomb gap and to weaken antiferromagnetic (AF) correlation.

In chapter 6, the nature of the AF gap has been investigated by ARPES. We have revealed the momentum dependence of the AF gap which could not be explained by the tight-binding model with $\sqrt{2}\times\sqrt{2}$ AF order. Qualitative agreement with the variational Monte-Carlo calculation suggest that the anisotropy originates from the effect of strong electron correlation beyond the simple AF band splitting. The present results will advance our understanding of the AF correlation in the electron-doped cuprates.

In chapter 7, we have studied the SC gap of protect-annealed $Pr_{1.3-x}La_{0.7}Ce_xCuO_4$ single crystals. Although AF correlation was strongly suppressed by protect annealing, the SC gap exhibited *d*-wave symmetry, which may be mediated by AF spin fluctuations.

To summarize, the present thesis has disentangled three kinds of annealing effects and unveiled the electronic structure of the SC parent compounds of electron-doped cuprates by means of photoemission spectroscopy. The effects of annealing can be understood microscopically as follows: Annealing originally removes impurity oxygen atoms at the apical site, but excessive annealing also creates oxygen defects at the regular [CuO_2-plane and/or LnO-layer (Ln: lanthanoids)] sites. The apical oxygen atoms produce the Coulomb gap and enhance AF correlation by localizing electrons, whereas the oxygen defects at the regular sites dope the system with electrons.

Taking this into consideration, the results presented in chapters 3 and 4 can be interpreted as follows: The SC parent compounds contain oxygen defects at the regular sites, and thus are doped with a considerable amount of electrons, 0.15-0.17 per Cu atom. Oxygen deficiency may be less destructive to the superconductivity than Ce doping, which reaches the solubility limit at $x \sim 0.18$, and hence the highest T_c is achieved at $x = 0$ by doping electrons only by creating oxygen defects.

The present studies have thus clarified the nature of the SC parent compound of electron-doped cuprates as well as the mechanism of annealing conducted to induce superconductivity. We have shown that the recently reported superconductivity in the parent compound is due to electron doping by oxygen deficiency. The possibility of the superconductivity at half-filling still cannot be excluded by the present thesis, and hence is worth further investigation. Our findings will make a significant contribution to the establishment of the phase diagram of the cuprate superconductors which is mandatory to explore the mechanism of high-temperature superconductivity.

Acknowledgements

It is my great pleasure to express my special gratitude to the following people for their help concerning my study.

First of all, I would like to express my sincere gratitude to my supervisor Prof. Atsushi Fujimori who has guided me to the exciting and fruitful research project. I would like to thank him for his kind guidance, a lot of valuable advises, enlightening discussions, and continuous encouragement throughout this study.

I am grateful to Dr. Yoshiharu Krockenberger and Dr. Hideki Yamamoto for teaching me the principles and techniques of MBE and providing me with the opportunity to grow thin films with sophisticated equipment. I have to express my gratitude to Mr. Taro Ohgi, Mr. Takuya Konno, Ms. Akira Takahashi, Mr. Yosuke Mori, Prof. Tadashi Adachi, and Prof. Yoji Koike for supplying high-quality single crystals of $Pr_{1.3-x}La_{0.7}Ce_xCuO_4$ and for a lot of enlightening discussions on the electron-doped cuprate superconductors.

Thanks are also due to Prof. Kanta Ono, Prof. Hiroshi Kumigashira and Dr. Nobuhito Inami for their experimental support at KEK-PF BL28A during our beamtime. I would also acknowledge the precious collaboration with Dr. Masaki Kobayashi, Prof. Koji Horiba, and Prof. Hiroshi Kumigashira at KEK-PF BL2A. It is my pleasure to express my gratitude to Dr. Makoto Hashimoto, Dr. Donghui Lu, and Prof, Zhi-Xun Shen for their experimental support at SSRL 5-4 and helpful discussion about the cuprate superconductors. I would also like to thank Dr. Eiji Ikenaga and Dr. Akira Yasui for granting us limited beamtimes and for their valuable experimental support at SPring-8 BL47XU. For the experiment at SPring-8 BL07LSU, I am grateful to Mr. Kohei Yamamoto, Mr. Yuichi Yokoyama, Dr. Yasuyuki Hirata, Dr. Kou Takubo, Prof. Hiroki Wadati, and Prof. Shik Shin. I would like to express my gratitude to Dr. Shinichiro Ideta and Prof. Kiyohisa Tanaka for their experimental support at UVSOR BL7U and a lot of fruitful discussion about the high-temperature superconductors. I am also grateful to Dr. Yuichi Ota, Prof. Kozo Okazaki, and Prof. Shik Shin for providing me the opportunity of state-of-the-art laser ARPES experiment.

I would like to express my great thanks to the former and the present members of Fujimori group; Prof. Teppei Yoshida, Prof. Kozo Okazaki, Dr. Walid Malaeb, Dr. Virendra Kumar Verma, Dr. Keisuke Ishigami, Mr. Leo Cristobal C Ambolode

II, Dr. Liang Liu, Mr. Goro Shibata, Dr. Hakuto Suzuki, Mr. Takayuki Harano, Dr. Jian Xu, Mr. Yukio Takahashi, Mr. Shoya Sakamoto, Mr. Keisuke Koshiishi, Mr. Yosuke Nonaka, Mr. Keisuke Ikeda, Mr. Zhendong Chi, Mr. Suguru Nakata, Mr. Kenta Hagiwara, Mr. Chun Lin, and Mr. Yuxuan Wan.

I would like to thank Ms. Yuko Shimazaki, Ms. Ami Michimura, and Ms. Mayuko Niwata for dealing with a lot of business stuff and giving me continuous encouragement.

Last but not least, I would like to thank my wife, parents, and brother for supporting my student life and research activities.

December 2016,
Masafumi Horio

References

[1] Y. Tokura, H. Takagi, and S. Uchida, Nature (London) **337**, 345 (1989).

[2] N. P. Armitage, P. Fournier, and R. L. Greene, Rev. Mod. Phys. **82**, 2421 (2010).

[3] M. Naito, S. Karimoto, and A. Tsukada, Superconductor Science and Technology **15**, 1663 (2002).

[4] Y. Koike, A. Kakimoto, M. Mochida, H. Sato, T. Noji, M. Kato, and Y. Saito, Jpn. J. Appl. Phys. **31**, 2721 (1992).

[5] Y. Krockenberger, J. Kurian, A. Winkler, A. Tsukada, M. Naito, and L. Alff, Phys. Rev. B **77**, 060505 (2008).

[6] T. Sasagawa, K. Unozawa, K. Ohishi, S. Pyon, K. H. Satoh, A. Koda, R. Kadono, and H. Takagi, KEK-MSL Progress Report (2006).

[7] J. Zaanen, G. A. Sawatzky, and J. W. Allen, Phys. Rev. Lett. **55**, 418 (1985).

[8] F. C. Zhang and T. M. Rice, Phys. Rev. B **37**, 3759 (1988).

[9] Y. Tokura, S. Koshihara, T. Arima, H. Takagi, S. Ishibashi, T. Ido, and S. Uchida, Phys. Rev. B **41**, 11657 (1990).

[10] N. L. Wang, G. Li, D. Wu, X. H. Chen, C. H. Wang, and H. Ding, Phys. Rev. B **73**, 184502 (2006).

[11] K. Tsutsui, T. Tohyama, and S. Maekawa, Phys. Rev. Lett. **83**, 3705 (1999).

[12] N. P. Armitage, F. Ronning, D. H. Lu, C. Kim, A. Damascelli, K. M. Shen, D. L. Feng, H. Eisaki, Z.-X. Shen, P. K. Mang, N. Kaneko, M. Greven, Y. Onose, Y. Taguchi, and Y. Tokura, Phys. Rev. Lett. **88**, 257001 (2002).

[13] T. Xiang, H. G. Luo, D. H. Lu, K. M. Shen, and Z. X. Shen, Phys. Rev. B **79**, 014524 (2009).

[14] T. Valla, A. V. Fedorov, P. D. Johnson, B. O. Wells, S. L. Hulbert, Q. Li, G. D. Gu, and N. Koshizuka, Science **285**, 2110 (1999).

[15] T. Valla, A. V. Fedorov, P. D. Johnson, Q. Li, G. D. Gu, and N. Koshizuka, Phys. Rev. Lett. **85**, 828 (2000).

[16] C. M. Varma, P. B. Littlewood, S. Schmitt-Rink, E. Abrahams, and A. E. Ruckenstein, Phys. Rev. Lett. **63**, 1996 (1989).

[17] E. Abrahams and C. M. Varma, Proc. Natl. Acad. Sci. U.S.A. **97**, 5714 (2000).

[18] C. Tsuei, A. Gupta, and G. Koren, Physica C **161**, 415 (1989).

[19] Y. Krockenberger, H. Yamamoto, A. Tsukada, M. Mitsuhashi, and M. Naito, Phys. Rev. B **85**, 184502 (2012).

[20] E. Moran, A. Nazzal, T. Huang, and J. Torrance, Physica C **160**, 30 (1989).

[21] J.-M. Tarascon, E. Wang, L. H. Greene, B. G. Bagley, G. W. Hull, S. M. D'Egidio, P. F. Miceli, Z. Z. Wang, T. W. Jing, J. Clayhold, D. Brawner, and N. P. Ong, Phys. Rev. B **40**, 4494 (1989).

[22] E. Takayama-Muromachi, F. Izumi, Y. Uchida, K. Kato, and H. Asano, Physica C **159**, 634 (1989).

[23] J. Kim and D. Gaskell, Physica C **209**, 381 (1993).

[24] P. G. Radaelli, J. D. Jorgensen, A. J. Schultz, J. L. Peng, and R. L. Greene, Phys. Rev. B **49**, 15322 (1994).

[25] A. J. Schultz, J. D. Jorgensen, J. L. Peng, and R. L. Greene, Phys. Rev. B **53**, 5157 (1996).

[26] X. Q. Xu, S. N. Mao, W. Jiang, J. L. Peng, and R. L. Greene, Phys. Rev. B **53**, 871 (1996).

[27] G. Riou, P. Richard, S. Jandl, M. Poirier, P. Fournier, V. Nekvasil, S. N. Barilo, and L. A. Kurnevich, Phys. Rev. B **69**, 024511 (2004).

[28] P. Richard, G. Riou, I. Hetel, S. Jandl, M. Poirier, and P. Fournier, Phys. Rev. B **70**, 064513 (2004).

[29] P. K. Mang, S. Larochelle, A. Mehta, O. P. Vajk, A. S. Erickson, L. Lu, W. J. L. Buyers, A. F. Marshall, K. Prokes, and M. Greven, Phys. Rev. B **70**, 094507 (2004).

[30] H. J. Kang, P. Dai, B. J. Campbell, P. J. Chupas, S. Rosenkranz, P. L. Lee, Q. Huang, S. Li, S. Komiya, and Y. Ando, Nat. Mater. **6**, 224 (2007).

[31] P. K. Mang, O. P. Vajk, A. Arvanitaki, J. W. Lynn, and M. Greven, Phys. Rev. Lett. **93**, 027002 (2004).

[32] J. S. Higgins, Y. Dagan, M. C. Barr, B. D. Weaver, and R. L. Greene, Phys. Rev. B **73**, 104510 (2006).

[33] J. Gauthier, S. Gagné, J. Renaud, M.-E. Gosselin, P. Fournier, and P. Richard, Phys. Rev. B **75**, 024424 (2007).

[34] M. Fujita, H. Hiraka, M. Matsuda, M. Matsuura, J. M. Tranquada, S. Wakimoto, G. Xu, and K. Yamada, J. Phys. Soc. Jpn. **81**, 011007 (2012).

[35] S. D. Wilson, P. Dai, S. Li, S. Chi, H. J. Kang, and J. W. Lynn, Nature **442**, 59 (2006).

[36] W. S. Lee, J. J. Lee, E. A. Nowadnick, W. Tabis, S. W. Huang, V. N. Strocov, E. M. Motoyama, G. Yu, B. Moritz, M. Greven, T. Schmitt, Z. X. Shen, and T. P. Devereaux, Nat. Phys. **10**, 883 (2014).

[37] K. Yamada, K. Kurahashi, T. Uefuji, M. Fujita, S. Park, S.-H. Lee, and Y. Endoh, Phys. Rev. Lett. **90**, 137004 (2003).

[38] P. Dai, H. A. Mook, R. D. Hunt, and F. Doğan, Phys. Rev. B **63**, 054525 (2001).

[39] G. Yu, Y. Li, E. M. Motoyama, and M. Greven, Nat. Phys. **5**, 873 (2009).

[40] N. Bulut and D. J. Scalapino, Phys. Rev. B **47**, 3419 (1993).

[41] F. Krüger, S. D. Wilson, L. Shan, S. Li, Y. Huang, H.-H. Wen, S.-C. Zhang, P. Dai, and J. Zaanen, Phys. Rev. B **76**, 094506 (2007).

[42] M. Fujita, M. Matsuda, S.-H. Lee, M. Nakagawa, and K. Yamada, Phys. Rev. Lett. **101**, 107003 (2008).

[43] Y. Onose, Y. Taguchi, K. Ishizaka, and Y. Tokura, Phys. Rev. Lett. **87**, 217001 (2001).

[44] A. Zimmers, Y. Noat, T. Cren, W. Sacks, D. Roditchev, B. Liang, and R. L. Greene, Phys. Rev. B **76**, 132505 (2007).

[45] N. P. Armitage, D. H. Lu, C. Kim, A. Damascelli, K. M. Shen, F. Ronning, D. L. Feng, P. Bogdanov, Z.-X. Shen, Y. Onose, Y. Taguchi, Y. Tokura, P. K. Mang, N. Kaneko, and M. Greven, Phys. Rev. Lett. **87**, 147003 (2001).

[46] H. Matsui, K. Terashima, T. Sato, T. Takahashi, S.-C. Wang, H.-B. Yang, H. Ding, T. Uefuji, and K. Yamada, Phys. Rev. Lett. **94**, 047005 (2005).

[47] S. R. Park, Y. S. Roh, Y. K. Yoon, C. S. Leem, J. H. Kim, B. J. Kim, H. Koh, H. Eisaki, N. P. Armitage, and C. Kim, Phys. Rev. B **75**, 060501 (2007).

[48] H. Matsui, T. Takahashi, T. Sato, K. Terashima, H. Ding, T. Uefuji, and K. Yamada, Phys. Rev. B **75**, 224514 (2007).

[49] P. Richard, M. Neupane, Y.-M. Xu, P. Fournier, S. Li, P. Dai, Z. Wang, and H. Ding, Phys. Rev. Lett. **99**, 157002 (2007).

[50] M. Ikeda, T. Yoshida, A. Fujimori, M. Kubota, K. Ono, H. Das, T. Saha-Dasgupta, K. Unozawa, Y. Kaga, T. Sasagawa, and H. Takagi, Phys. Rev. B **80**, 014510 (2009).

[51] D. Song, S. R. Park, C. Kim, Y. Kim, C. Leem, S. Choi, W. Jung, Y. Koh, G. Han, Y. Yoshida, H. Eisaki, D. H. Lu, Z.-X. Shen, and C. Kim, Phys. Rev. B **86**, 144520 (2012).

[52] C.-P. Chou and T.-K. Lee, J. Phys. Chem. Solids **69**, 2944 (2008).

[53] M. Ikeda, Doctor thesis (2008).

[54] E. M. Motoyama, G. Yu, I. M. Vishik, O. P. Vajk, P. K. Mang, and M. Greven, Nature (London) **445**, 186 (2007).

[55] A. F. Santander-Syro, M. Ikeda, T. Yoshida, A. Fujimori, K. Ishizaka, M. Okawa, S. Shin, R. L. Greene, and N. Bontemps, Phys. Rev. Lett. **106**, 197002 (2011).

[56] T. Helm, M. V. Kartsovnik, M. Bartkowiak, N. Bittner, M. Lambacher, A. Erb, J. Wosnitza, and R. Gross, Phys. Rev. Lett. **103**, 157002 (2009).

[57] T. Helm, M. V. Kartsovnik, I. Sheikin, M. Bartkowiak, F. Wolff-Fabris, N. Bittner, W. Biberacher, M. Lambacher, A. Erb, J. Wosnitza, and R. Gross, Phys. Rev. Lett. **105**, 247002 (2010).

[58] A. Damascelli, Z. Hussain, and Z.-X. Shen, Rev. Mod. Phys. **75**, 473 (2003).

[59] D. J. Scalapino, Rev. Mod. Phys. **84**, 1383 (2012).

[60] W. N. Hardy, D. A. Bonn, D. C. Morgan, R. Liang, and K. Zhang, Phys. Rev. Lett. **70**, 3999 (1993).

[61] D. H. Wu, J. Mao, S. N. Mao, J. L. Peng, X. X. Xi, T. Venkatesan, R. L. Greene, and S. M. Anlage, Phys. Rev. Lett. **70**, 85 (1993).

[62] A. Andreone, A. Cassinese, A. Di Chiara, R. Vaglio, A. Gupta, and E. Sarnelli, Phys. Rev. B **49**, 6392 (1994).

[63] J. R. Cooper, Phys. Rev. B **54**, R3753 (1996).

[64] L. Alff, S. Meyer, S. Kleefisch, U. Schoop, A. Marx, H. Sato, M. Naito, and R. Gross, Phys. Rev. Lett. **83**, 2644 (1999).

[65] C. C. Tsuei and J. R. Kirtley, Phys. Rev. Lett. **85**, 182 (2000).

[66] T. Sato, T. Kamiyama, T. Takahashi, K. Kurahashi, and K. Yamada, Science **291**, 1517 (2001).

[67] N. P. Armitage, D. H. Lu, D. L. Feng, C. Kim, A. Damascelli, K. M. Shen, F. Ronning, Z.-X. Shen, Y. Onose, Y. Taguchi, and Y. Tokura, Phys. Rev. Lett. **86**, 1126 (2001).

[68] G. Blumberg, A. Koitzsch, A. Gozar, B. S. Dennis, C. A. Kendziora, P. Fournier, and R. L. Greene, Phys. Rev. Lett. **88**, 107002 (2002).

[69] H. Matsui, K. Terashima, T. Sato, T. Takahashi, M. Fujita, and K. Yamada, Phys. Rev. Lett. **95**, 017003 (2005).

[70] M. Brinkmann, T. Rex, H. Bach, and K. Westerholt, Phys. Rev. Lett. **74**, 4927 (1995).

[71] O. Matsumoto, A. Utsuki, A. Tsukada, H. Yamamoto, T. Manabe, and M. Naito, Physica C **468**, 1148 (2008).

[72] T. Takamatsu, M. Kato, T. Noji, and Y. Koike, Appl. Phys. Express **5**, 073101 (2012).

[73] A. Tsukada, M. Noda, H. Yamamoto, and M. Naito, Physica C **426-431**, 459 (2005).

[74] Y. Onose, Y. Taguchi, K. Ishizaka, and Y. Tokura, Phys. Rev. B **69**, 024504 (2004).

[75] E. Wang, J.-M. Tarascon, L. H. Greene, G. W. Hull, and W. R. McKinnon, Phys. Rev. B **41**, 6582 (1990).

[76] C. Weber, K. Haule, and G. Kotliar, Nat. Phys. **6**, 574 (2010).

[77] A. Tsukada, Y. Krockenberger, M. Noda, H. Yamamoto, D. Manske, L. Alff, and M. Naito, Solid State Commun. **133**, 427 (2005).

[78] M. Noda, A. Tsukada, H. Yamamoto, and M. Naito, Physica C **426-431**, 220 (2005).

[79] O. Matsumoto, A. Utsuki, A. Tsukada, H. Yamamoto, T. Manabe, and M. Naito, Phys. Rev. B **79**, 100508 (2009).

[80] O. Matsumoto, A. Utsuki, A. Tsukada, H. Yamamoto, T. Manabe, and M. Naito, Physica C **469**, 924 (2009).

[81] O. Matsumoto, A. Utsuki, A. Tsukada, H. Yamamoto, T. Manabe, and M. Naito, Physica C **469**, 940 (2009).

[82] H. Yamamoto, A. Tsukada, O. Matsumoto, and M. Naito, Physica C **470**, S88 (2010).

[83] H. Yamamoto, O. Matsumoto, Y. Krockenberger, K. Yamagami, and M. Naito, Solid State Commun. **151**, 771 (2011).

[84] A. Ikeda, O. Matsumoto, H. Yamamoto, T. Manabe, and M. Naito, Physica C **471**, 686 (2011).

[85] Y. Krockenberger, H. Irie, O. Matsumoto, K. Yamagami, A. Tsukada, M. Naito, and H. Yamamoto, Sci. Rep. **3**, 2235 (2013).

[86] Y. Krockenberger, B. Eleazer, H. Irie, and H. Yamamoto, J. Phys. Soc. Jpn. **83**, 114602 (2014).

[87] S. Asai, S. Ueda, and M. Naito, Physica C **471**, 682 (2011).

[88] M. H. Whangbo, M. Evain, M. A. Beno, and J. M. Williams, Inorganic Chemistry **26**, 1829 (1987).

[89] C. Weber, K. Haule, and G. Kotliar, Phys. Rev. B **82**, 125107 (2010).

[90] T. Adachi, Y. Mori, A. Takahashi, M. Kato, T. Nishizaki, T. Sasaki, N. Kobayashi, and Y. Koike, J. Phys. Soc. Jpn. **82**, 063713 (2013).

[91] X. F. Sun, Y. Kurita, T. Suzuki, S. Komiya, and Y. Ando, Phys. Rev. Lett. **92**, 047001 (2004).

[92] M. Horio, Master thesis (2014).

[93] M. Horio, T. Adachi, Y. Mori, A. Takahashi, T. Yoshida, H. Suzuki, L. C. C. Ambolode, K. Okazaki, K. Ono, H. Kumigashira, H. Anzai, M. Arita, H. Namatame, M. Taniguchi, D. Ootsuki, K. Sawada, M. Takahashi, T. Mizokawa, Y. Koike, and A. Fujimori, Nat. Commun. **7**, 10567 (2016).

[94] A. C. R. Brundle, J. Vac. Sci. Technol. 212 (1974).

[95] S. Ideta, Doctor thesis (2012).

[96] H. Yamamoto, Y. Krockenberger, and M. Naito, Proc. of SPIE **8987**, 89870V (2014).

[97] E. Navarro, D. Jaque, J. Villegas, J. Martín, A. Serquis, F. Prado, A. Caneiro, and J. Vicent, J. Alloys Compnds. **323-324**, 580 (2001).

[98] K. M. Kojima, Y. Krockenberger, I. Yamauchi, M. Miyazaki, M. Hiraishi, A. Koda, R. Kadono, R. Kumai, H. Yamamoto, A. Ikeda, and M. Naito, Phys. Rev. B **89**, 180508 (2014).

[99] T. Arima, Y. Tokura, and S. Uchida, Phys. Rev. B **48**, 6597 (1993).

[100] H. I. Wei, C. Adamo, E. A. Nowadnick, E. B. Lochocki, S. Chatterjee, J. P. Ruf, M. R. Beasley, D. G. Schlom, and K. M. Shen, Phys. Rev. Lett. **117**, 147002 (2016).

[101] Y. Krockenberger, M. Horio, H. Irie, A. Fujimori, and H. Yamamoto, Applied Physics Express **8**, 053101 (2015).

[102] S.-Y. Xu, M. Neupane, C. Liu, D. Zhang, A. Richardella, L. Andrew Wray, N. Alidoust, M. Leandersson, T. Balasubramanian, J. Sanchez-Barriga, O. Rader, G. Landolt, B. Slomski, J. Hugo Dil, J. Osterwalder, T.-R. Chang, H.-T. Jeng, H. Lin, A. Bansil, N. Samarth, and M. Zahid Hasan, Nat. Phys. **8**, 616 (2012).

[103] D. Liu, W. Zhang, D. Mou, J. He, Y.-B. Ou, Q.-Y. Wang, Z. Li, L. Wang, L. Zhao, S. He, Y. Peng, X. Liu, C. Chen, L. Yu, G. Liu, X. Dong, J. Zhang, C. Chen, Z. Xu, J. Hu, X. Chen, X. Ma, Q. Xue, and X. Zhou, Nat. Commun. **3**, 931 (2012).

[104] T. Suzuki, M. Nagoshi, Y. Fukuda, K. Oh-ishi, Y. Syono, and M. Tachiki, Phys. Rev. B **42**, 4263 (1990).

[105] S. R. Park, T. Morinari, D. J. Song, C. S. Leem, C. Kim, S. K. Choi, K. Choi, J. H. Kim, F. Schmitt, S. K. Mo, D. H. Lu, Z.-X. Shen, H. Eisaki, T. Tohyama, J. H. Han, and C. Kim, Phys. Rev. B **87**, 174527 (2013).

[106] H. Takagi, S. Uchida, and Y. Tokura, Phys. Rev. Lett. **62**, 1197 (1989).

[107] J. M. Luttinger, Phys. Rev. **119**, 1153 (1960).

[108] S. Massidda, N. Hamada, J. Yu, and A. Freeman, Physica C **157**, 571 (1989).

[109] M. Naito, Y. Krockenberger, A. Ikeda, and H. Yamamoto, Physica C **523**, 28 (2016).

[110] S. W. Zeng, Z. Huang, W. M. Lv, N. N. Bao, K. Gopinadhan, L. K. Jian, T. S. Herng, Z. Q. Liu, Y. L. Zhao, C. J. Li, H. J. Harsan Ma, P. Yang, J. Ding, T. Venkatesan, and Ariando, Phys. Rev. B **92**, 020503 (2015).

[111] H. Wadati and A. Fujimori, Journal of Electron Spectroscopy and Related Phenomena **190**, 222 (2013).

[112] M. Taguchi, A. Chainani, K. Horiba, Y. Takata, M. Yabashi, K. Tamasaku, Y. Nishino, D. Miwa, T. Ishikawa, T. Takeuchi, K. Yamamoto, M. Matsunami, S. Shin, T. Yokoya, E. Ikenaga, K. Kobayashi, T. Mochiku, K. Hirata, J. Hori, K. Ishii, F. Nakamura, and T. Suzuki, Phys. Rev. Lett. **95**, 177002 (2005).

[113] K. Maiti, J. Fink, S. de Jong, M. Gorgoi, C. Lin, M. Raichle, V. Hinkov, M. Lambacher, A. Erb, and M. S. Golden, Phys. Rev. B **80**, 165132 (2009).

[114] T. Böske, O. Knauff, R. Neudert, M. Kielwein, M. Knupfer, M. S. Golden, J. Fink, H. Eisaki, S. Uchida, K. Okada, and A. Kotani, Phys. Rev. B **56**, 3438 (1997).

[115] T. Böske, K. Maiti, O. Knauff, K. Ruck, M. S. Golden, G. Krabbes, J. Fink, T. Osafune, N. Motoyama, H. Eisaki, and S. Uchida, Phys. Rev. B **57**, 138 (1998).

[116] G. Panaccione, F. Offi, P. Torelli, G. Vanko, O. Tjernberg, P. Lacovig, A. Guarino, A. Fondacaro, A. Nigro, M. Sacchi, N. B. Brookes, and G. Monaco, Phys. Rev. B **77**, 125133 (2008).

[117] N. Harima, J. Matsuno, A. Fujimori, Y. Onose, Y. Taguchi, and Y. Tokura, Phys. Rev. B **64**, 220507 (2001).

[118] J. C. Slater, Int. J. Quantum. Chem. **S4**, 3 (1971).

[119] R. Sankari, M. Ehara, H. Nakatsuji, Y. Senba, K. Hosokawa, H. Yoshida, A. D. Fanis, Y. Tamenori, S. Aksela, and K. Ueda, Chemical Physics Letters **380**, 647 (2003).

[120] P. H. Citrin, P. Eisenberger, and D. R. Hamann, Phys. Rev. Lett. **33**, 965 (1974).

[121] S. Hüfner, *Photoelectron Spectroscopy* (Springer-Verlag, Berlin, 1995), Chap. 2, p. 35.

[122] E. Pellegrin, N. Nücker, J. Fink, S. L. Molodtsov, A. Gutiérrez, E. Navas, O. Strebel, Z. Hu, M. Domke, G. Kaindl, S. Uchida, Y. Nakamura, J. Markl, M. Klauda, G. Saemann-Ischenko, A. Krol, J. L. Peng, Z. Y. Li, and R. L. Greene, Phys. Rev. B **47**, 3354 (1993).

[123] C. F. J. Flipse, G. van der Laan, A. L. Johnson, and K. Kadowaki, Phys. Rev. B **42**, 1997 (1990).

[124] J. Fink, N. Nücker, E. Pellegrin, H. Romberg, M. Alexander, and M. Knupfer, Journal of Electron Spectroscopy and Related Phenomena **66**, 395 (1994).

[125] A. Krol, C. S. Lin, Z. H. Ming, C. J. Sher, Y. H. Kao, C. L. Lin, S. L. Qiu, J. Chen, J. M. Tranquada, M. Strongin, G. C. Smith, Y. K. Tao, R. L. Meng, P. H. Hor, C. W. Chu, G. Cao, and J. E. Crow, Phys. Rev. B **42**, 4763 (1990).

[126] K. Okada and A. Kotani, J. Phys. Soc. Jpn. **74**, 653 (2005).

[127] A. Kotani and F. de Groot, *Core Level Spectroscopy of Solids* (CRC Press, Florida, 2008), Chap. 5, p. 217.

[128] H. Eskes, M. B. J. Meinders, and G. A. Sawatzky, Phys. Rev. Lett. **67**, 1035 (1991).

[129] M. B. J. Meinders, H. Eskes, and G. A. Sawatzky, Phys. Rev. B **48**, 3916 (1993).

[130] J. M. Tarascon, E. Wang, S. Kivelson, B. G. Bagley, G. W. Hull, and R. Ramesh, Phys. Rev. B **42**, 218 (1990).

[131] K. Suzuki, K. Kishio, T. Hasegawa, and K. Kitazawa, Physica C **166**, 357 (1990).

[132] A. L. Efros and B. I. Shklovskii, Journal of Physics C: Solid State Physics **8**, L49 (1975).

[133] T. Adachi, A. Takahashi, K. M. Suzuki, M. A. Baqiya, T. Konno, T. Takamatsu, M. Kato, I. Watanabe, A. Koda, M. Miyazaki, R. Kadono, and Y. Koike, J. Phys. Soc. Jpn. **85**, 114716 (2016).

[134] B. Kyung, V. Hankevych, A.-M. Daré, and A.-M. S. Tremblay, Phys. Rev. Lett. **93**, 147004 (2004).

[135] D. Sénéchal and A.-M. S. Tremblay, Phys. Rev. Lett. **92**, 126401 (2004).

[136] M. Yamamoto, Y. Kohori, H. Fukazawa, A. Takahashi, T. Ohgi, T. Adachi, and Y. Koike, J. Phys. Soc. Jpn. **85**, 024708 (2016).